

DOE STUDY OF POLYURETHANE PROCESSING
PARAMETERS AFFECTS ON MICROPHASE
SEPARATION AND MATERIAL PROPERTIES

By

TAREK KANDALAFT

Bachelor of Science in Mechanical Engineering

Oklahoma State University

Stillwater, OK

2013

Submitted to the Faculty of the
Graduate College of the
Oklahoma State University
in partial fulfillment of
the requirements for
the Degree of
MASTER OF SCIENCE
December, 2016

DOE STUDY OF POLYURETHANE PROCESSING
PARAMETERS AFFECTS ON MICROPHASE
SEPARATION AND MATERIAL PROPERTIES

Thesis Approved:

Dr. Ranji Vaidyanathan

Thesis Adviser

Dr. Raj Singh

Dr. James Smay

ACKNOWLEDGEMENTS

Firstly, I would like to express my sincere gratitude to my advisor, Dr. Ranji Vaidyanathan, for his support and guidance through this research and all my course work. Moreover, I would like to give thanks to my committee members, Dr. Raj Singh and Dr. James Smay, for monitoring over my professional development and providing direction in the vast material science field. I would like to offer my thanks to Dr. Feng Lu for his support with imaging and other core labs equipment.

I would like to give special gratitude to my T.D. Williamson colleagues and managers who have offered endless encouragement and clarity through this work. Many thanks to Woody Smith and Eric Freeman who have offered generous support for my continued education and provided encouragement since the beginning. I would like to specifically express my appreciation to Jeff Hailey for his hours of help with equipment malfunctions and expertise in DOE's and statistical insight.

A special thanks to my lab colleagues, Muthu Subramanian and Noom Graham for their support and empathy during this work.

I would like to give appreciation to Sara Gleason for her rigorous proof reading and corrections to my many grammatical mishaps.

Finally, my gratitude to Susan Gleason for her incredible support, tolerance, and patience through many study and coffee sessions. I could not have stayed focused, nor awake, without her gentle push to keep going.

Name: TAREK KANDALAFT

Date of Degree: DECEMBER, 2016

Title of Study: DOE STUDY OF POLYURETHANE PROCESSING PARAMETERS
AFFECTS ON MICROPHASE SEPARATION AND MATERIAL
PROPERTIES

Major Field: MATERIAL SCIENCE AND ENGINEERING

Abstract:

In this study, a design of experiments (DOE) has been setup to better understand the effects of percentage of hard segment (%HS), mixing index, temperature, and environmental humidity on the microstructure development, tensile properties, and thermal properties of an MDI based poly(ester urethane) with 1,4 butane diol chain extender. Fourier transform infrared spectroscopy (FTIR) and differential scanning calorimeter (DSC) were utilized to better investigate the amount of microphase separation. Tensile testing was conducted to measure the elongation, tensile strength at break, and the resistance to tear. Finally, scanning electron microscopy (SEM) was used to examine any microstructure or superstructure development or phase separation. A DOE statistical regression analysis was completed to insure adequate sample sizes, low factor aliasing, and high statistical confidence and signal-to-noise (low p-value and high T-stat). Regression models are presented. Results indicate that the amount of hard segment had a large influence on hydrogen bonded carbonyl groups. However, these formations remained in amorphous state and did not form well structured, phase separated blocks. Results also show that the mixing temperature has a large effect on both tensile and tear strengths. Moreover, DSC results indicate a significant impact of mixing temperature on the crystallinity of the sample. A large second order interaction between relative humidity and the samples glass transition temperature has been observed. However, humidity effects were not detectable in FTIR spectrums.

TABLE OF CONTENTS

Chapter	Page
I. INTRODUCTION.....	1
Primary Goals	1
Objectives	2
Hypothesis.....	4
Motivation and Application	4
II. BACKGROUND AND LITERATURE REVIEW	14
Polyurethane	14
Material Properties.....	30
Characterization Methods	39
DOE Methodology.....	44
III. EXPERIMENTAL PROCEDURES.....	48
DOE Design	48
Sample Preparation	53
Characterization Procedures	55
IV. RESULTS AND ANALYSIS.....	58
FTIR Characterization	58
DSC Characterization	68
Tensile Testing.....	71
SEM Imaging.....	75
V. DISCUSSION AND CONCLUSION.....	78
Discussion.....	78
Conclusion	82
Future Work	83
REFERENCES	85
APPENDICES	91

LIST OF TABLES

Table	Page
Table 1: Relative reaction rates of aromatic isocyanates	18
Table 2: Commonly used diisocyanates.....	19
Table 3: Common polyol's and their chemical structures.	20
Table 4: Hydroxide and amine based chain extenders and their chemical structures.....	21
Table 5: Crosslinking molecules derived from isocyanate	24
Table 6: Level of crack growth depending on tearing energy	32
Table 7: Infrared frequency ranges for the characteristics vibrations in polyurethane elastomers.....	43
Table 8: 4 factor, 3 level, CCD test matrix.	51
Table 9: Molecular weights and functionality of chemical components.	54
Table 10: Composition and processing parameters of sample numbers	59
Table 11: Peak deconvolution of carbonyl region FTIR spectrum	64
Table 12: Coded regression table for peak deconvolution of FTIR spectrum	65
Table 13: DSC testing results	68
Table 14: Coded regression coefficients and statistics for DSC results.....	70
Table 15: Tensile testing results	72
Table 16: Coded regression coefficients and statistics for tensile testing data.	73
Table 17: Uncoded coefficients for tensile DOE.	93
Table 18: Uncoded coefficients for DSC DOE.....	93
Table 19: Uncoded coefficients for FTIR DOE.....	94

LIST OF FIGURES

Figure	Page
Figure 1: The size of the U.S. transmission, gathering, and distribution pipeline infrastructure.....	5
Figure 2: Energy consumption by source	7
Figure 3: U.S. energy production by sources.....	8
Figure 4: A Multi-Data Set (MDS) tool.....	9
Figure 5: The large array of pipeline utility pigs	10
Figure 6: Forces encountered in a typical pigging operation.....	11
Figure 7: Chemical reaction for urethane and urea linkages.....	15
Figure 8: Diagram of soft and hard segments in a block copolymer polyurethane chain.....	16
Figure 9: polyurethane microstructure reaction to applied stress	21
Figure 10: Monodentate and bidentate hydrogen bond.....	25
Figure 11: Viscoelastic response of material to sinusoidal excitation load	33
Figure 12: Creep response with a force step function applied	34
Figure 13: Relaxation models with a strain step function applied	34
Figure 14: 10 cyclic loadings of a 75 Shore A polyurethane elastomer	36
Figure 15: Different modes of tensile testing.....	40
Figure 16: Schematic of ATR standing wave interaction with material.....	41
Figure 17: Result ranking of outputs from QFD 1.....	48
Figure 18: Rank of CTF from QFD 2.	49
Figure 19: IPO diagram	50
Figure 20: FTIR Spectrum of DOE test specimens	60
Figure 21: Carbonyl region of FTIR spectra for 0% hard segment	61
Figure 22: Carbonyl region of FTIR spectra for 20% hard segment	62
Figure 23: Carbonyl region of FTIR spectra for 40% hard segment	63
Figure 24: Carbonyl region of FTIR spectra for 72% hard segment	63
Figure 25: residual plots of generated regression model	67

Figure	Page
Figure 26: Residual plot of Tg (a) and ΔC_p (b).....	71
Figure 27: Main effects plots for predicted elongation and tear strength	74
Figure 28: Residual plot of predicted values of elongation (a) and tear strength (b).....	75
Figure 29: SEM, SE images of SN0034, 20% hard segment urethane	76
Figure 30: SEM, SE images of SN0049, 40% hard segment urethane	77
Figure 31: Coded coefficient summary of factor effects on mechanical and thermal properties ..	79
Figure 32: Coded regression coefficients for FTIR carbonyl peaks and DSC ΔC_p	80
Figure 33: Main effects plot of 1733 and 1708 cm^{-1} carbonyl peaks.....	81
Figure 34: Full spectrum of manufacturer supplied MDI, BD, ester based polyurethane.	91
Figure 35: Selected regions of manufacturer supplied MDI, BD, ester based polyurethane.	92
Figure 36: Phase diagram with both LCST and USCT	101

CHAPTER I

Section 1: INTRODUCTION

1.1 Primary Goals

The primary goals of this thesis is:

To determine the sensitivity of MDI based polyurethane (PUR) material's mechanical and thermal properties to manufacturing controls and environmental conditions.

Polyurethanes are a widely used material for many applications such as in elastomers, biomedical materials, protective coatings, ecological lacquers, adhesives and binders, in ceramics, and electronic applications [1]. This is partly due to the highly customizable properties of polyurethane to meet its applications [2]. The three main components of a polyurethane reaction are the polyol, diisocyanate, and a chain extender. This will be further discussed in later sections. Many different combinations of these components can result in a wide variety of material combinations. However, some manufacturing challenges remain. For example, due to the high reactivity of the diisocyanate with active hydrogen, it becomes very sensitive to water and temperature exposure [3, 4]. Other processing parameters such as mold temperature, mix speed, catalyst, cure temperature, cure time, mixing tolerances and others can also affect the microstructure formation of the polyurethane, which affect material performance. Besides some industry rules-of-thumb, these factors can have varying effects and can be difficult to

predict. The first goal of this thesis is to understand and quantify the effect of these factors on bulk MDI based poly(ester urethane) elastomer using the design of experiments approach.

1.2 Objectives

In this thesis, the Design for Six Sigma (DFSS) approach to problem solving has been utilized. The reason for this is due to the large number of variables that can affect the polymer properties. DFSS is an industry accepted tool used for rigorous and focused implantation of proven principles and practices to improve manufacturing quality [6]. This methodology has been used in many industries such as automotive, communication, manufacturing, aerospace, and many others. The first objective to accomplish the first goal of this thesis is to begin by preparing a Design of Experiments (DOE). A DOE is an organized approach to understand a system with multiple input factors at different levels and with multiple outputs. This will be further discussed in subsequent sections.

Therefore, the major milestones or objectives of this thesis that are crucial to achieve the established goals above are:

Objective: To rank the effect of processing factors on mechanical properties and material thermal stability by a DOE approach.

Due to the high dependability of the microstructure development of a polyurethane component to its material performance, the processing parameters become a crucial factor. For example, it has been shown that deviations from stoichiometric mixing can alter these properties [1]. Therefore, in the industry, it is important for the design engineers to determine the stoichiometry which will give the most optimum properties. Moreover, the tolerances of the mixing machines used for mass production becomes important. For example, a machine with loose tolerances could cause large variations in crucial material properties, not initially intended

by the product development teams. Other manufacturing factors used in industry to produce PUR components that have been speculated as possible contributors to product variations are:

- 1) **Environmental humidity:** this is a result of the high reactivity of diisocyanate groups with water molecules to create a urea group and a CO₂ molecule capable of creating voids in a bulk material.
- 2) **Mold design and quality:** clean molds and the application of mold release can have a direct effect on the surface quality on the final cast product. In addition, mold design can play an important role in allowing entrapped air to be released during the pour process. Moreover, some molds are rotated, shaken, or stationary in an attempt to reduce entrapped air. Molds can be designed for open casting, compression molding, centrifugal molding, liquid injection casting, pressure casting, extrusion, vacuum casting, and transfer casting [7]. These can also play an important role on the microstructure development of the material.
- 3) **Material storage:** It has been shown that the storage temperature and humidity can have a large effect on the viscosity and NCO content of a prepolymer.
- 4) **Machine Tolerance and Settings:** Most industrial production of polyurethane utilizes sophisticated mixing machines that degas the chemical components, heat components to appropriate mixing temperatures, meter out the correct mass ratios, and inject the components into mixing chambers before pouring into the molds by the operators. The many settings such as mixing head speed, flow meter accuracy, processing temperatures, and others have been speculated to have a contribution on material quality.
- 5) **Post curing:** Once a part has been cast, the post curing can play an important role in the activation of the catalyst and necessary material reactions. Temperature and time of curing are monitored. However, incorrect control over these factors can create unintended variations.

6) **Operator Variations:** Similar to most manufacturing processes, machine operators can introduce additional variations to the product quality.

1.3 Hypothesis

In this study, polyurethane material will be produced using parameters suggested by a DOE experimental matrix. These will be further discussed in later sections.

Hypothesis 1: As the amount of hard segment is increased, a larger H-bonded network will form due to the increased density of urethane groups. This will result in a stiffer and stronger material.

Hypothesis 2: A higher mixing index will result in a more crosslinked polymer network. If a high mix index is processed at high temperatures, a lower crosslinked network would form due to the breaking down of the crosslinking molecules. Higher crosslinking could also result in improved mechanical and temperature properties.

Hypothesis 3: As processing temperature is increased, a higher microphase separated network will form. This is due to the LCST exhibited in polymer-polymer blends as will be discussed in further sections. Although the entropy term of the Gibbs free energy of mixing is driven up, the enthalpy terms dependence on temperature also increases with increasing molecular weight.

Hypothesis 4: As humidity increases, a reaction will occur with the diisocyanate and reduce mechanical properties by introducing CO₂ gas into the microstructure. Urea groups will increase as humidity is increased.

1.4 Motivation and Application

In the United States, a large network of pipelines transports energy, water, and other goods across the country to processing plants and end users. According to the Pipeline and Hazardous Materials Safety Administration (PHMSA), an agency of the Department of Transportation (DOT), there was an estimated 2.5 million miles of transmission, gathering, and distribution

pipeline infrastructure in the United States during 2014 [8]. These are the three major sectors of the oil and gas pipeline system. Gathering pipelines are pipelines that transport crude oils from the oil wells to either nearby refineries or junction points. Transmission pipelines then transport the product long distance, sometimes across the country or even continent to oil refineries or other destinations. These pipelines tend to be the largest. Finally, distribution pipelines distribute the final product, such as natural gas, gasoline, propane, etc. to their intended end-user. The amount of pipelines in each of these sectors is shown below in figure 1.

It can be clearly seen that distribution pipelines are the largest group. However, these tend to be the smallest lines in terms of diameter and pressure. In contrast, transmission pipelines are the largest pipelines. Sometimes these will reach 48 inches in diameter and larger for natural gas pipelines.

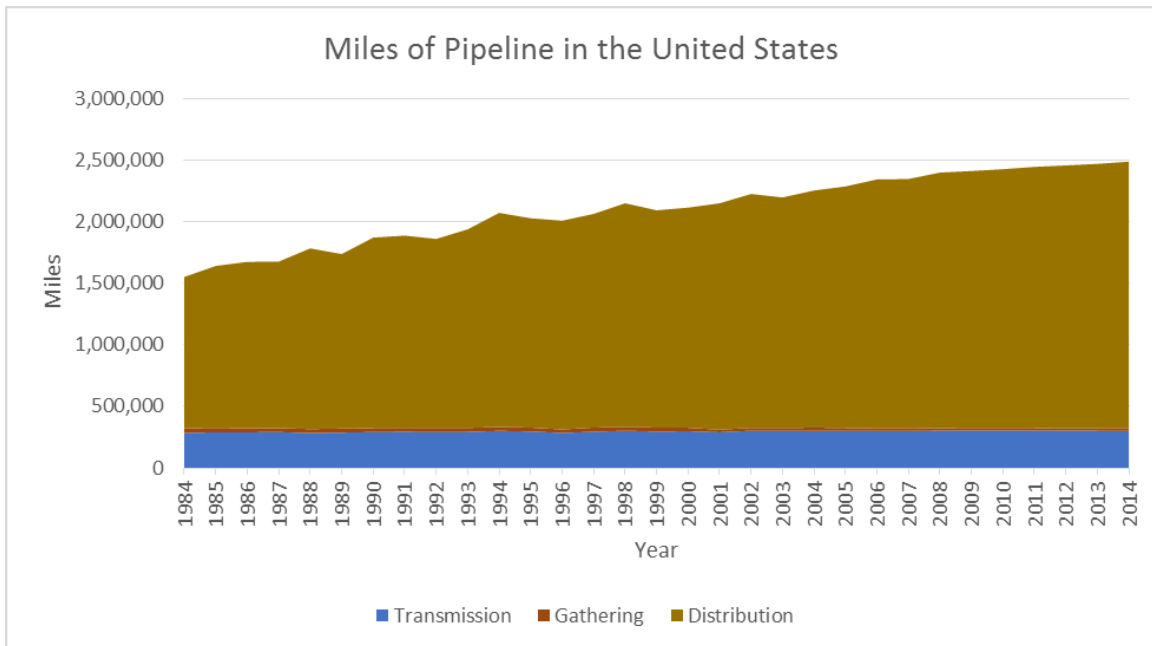


Figure 1: The size of the U.S. transmission, gathering, and distribution pipeline infrastructure according to the PHMSA annual report. [8]

Pipelines are an attractive means of transportation, especially to oil and gas producers, due to their high safety record for both human and environmental safety. According to the U.S.

Liquid Pipeline Usage & Mileage Report by the Association of Oil Pipe Lines (AOPL) and American Petroleum Institute (API), 99.999% of crude or other petroleum products reach their final destination safely [9]. This high level of reliability is unmatched with alternative means of transportation such as rail, road, or air transportation. Moreover, pipelines are advantageous over these methods due to their cost effectiveness and efficiency of transportation. Pipelines can run continuously with only a few operators. In addition, most pipelines are buried and routed away from populated areas for added safety.

As a result of these benefits, the U.S. pipeline network has seen consistent growth to meet ever growing energy demands. The mileage of liquid pipelines grew 3.5% from 2013 to 2014, with crude oil pipelines growing 9.1% during that same time period [9]. This growth has continued to help meet consumer demands and reduce energy imports. Although new alternative energy sources have increased, fossil fuels remain a vital part of the current energy sector. The U.S. Energy Information Administration (EIA) reported that in 2015, less than 10% of energy consumed and produced in the United States came from renewable energies, with nuclear and biofuels being the two major components [10]. In contrast, U.S. fossil fuel production has been steadily growing since 2010. This increase can be seen in figure 3. Therefore, the pipeline infrastructure has grown proportionally to meet the demand of transportation.

The need for maintenance, monitoring, and commissioning of this growing infrastructure is therefore of great interest. The intention of this thesis is to provide a valuable insight to the tools used for this kind of work.

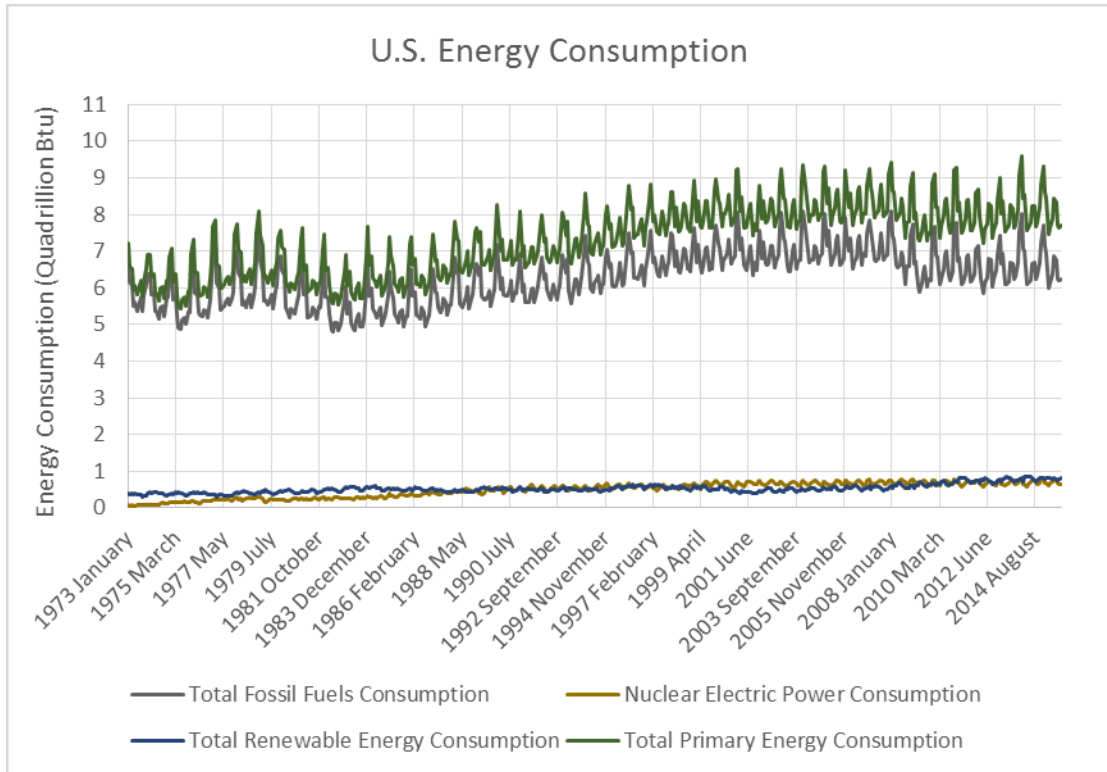


Figure 2: Energy consumption by source. [10]

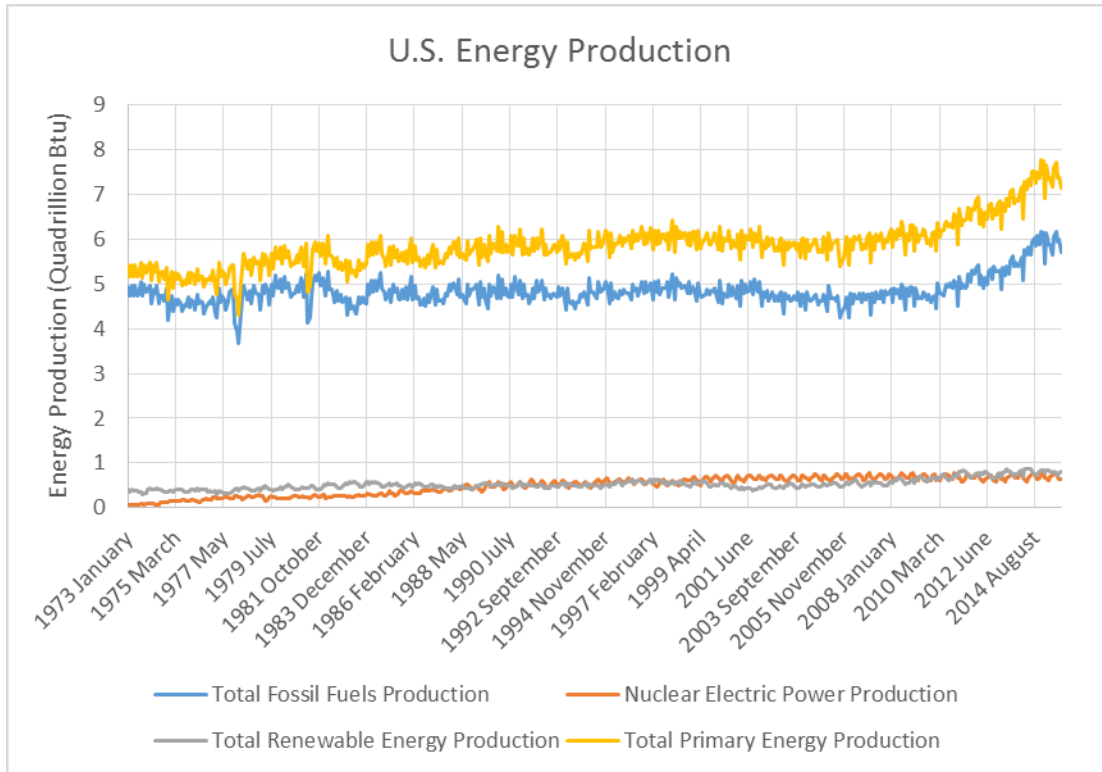


Figure 3: U.S. energy production by sources. [10]

The tools used for commissioning, inspecting, and maintaining pipeline integrity are called pipeline scrapers. In the United States and some other parts of the world, these are also referred to as pipeline pigs. These tools are used throughout the life span of the pipeline. Initially, they are used to bring the pipeline online, also known as commissioning. The purpose of these tools during this phase is to hydrotest the pipeline and remove any construction debris.

Aggressive pigs with brushes and magnets pickup and remove any welding rods, hand tools, dirt, and other debris left over from construction. Hydrotesting is a method of pressuring the pipeline above its operating pressure with water to validate all critical welds and other critical to safety components from leaks. However, in gas pipelines, it is crucial that this water is dried before operation. Therefore, pipeline pigs are run through the pipeline to absorb any remaining moisture.

Moreover, inspection is another crucial phase of the maintenance of the pipeline.

Inspection is done with sophisticated pigs that are propelled through the pipeline to scan the

pipeline walls for defects. Multiple methods can be used such as magnetic flux leakage (MFL), ultrasonic transducers (UT), caliper geometry tools, inertial mass units (IMU), electro-mechanical acoustic transducers (EMAT), and others. The discussion of these methods is not within the scope of this study, but in-depth literature can be found. These tools scan for pipeline damage and deterioration such as dents, pipeline shifts, cracking, corrosion, gouging, and any other anomalies that can occur. Data from the tool runs is recorded onboard, downloaded, and post analyzed. An example of such a tool can be seen in figure 4.



Figure 4: A Multi-Data Set (MDS) tool used during pipeline inspection to check for pipeline anomalies. This MDS tool utilizes multiple scanning techniques such as MFL, IMU, geometry, and ID/OD modules. Courtesy of T.D. Williamson.

Finally, the most commonly used pigs are general utility pigs. These pigs have many uses and applications. This can include cleaning, batching, displacement, coating applications, and light inspection. Cleaning pigs carry brushes, magnets, wax cutters, and other tools for removing debris that might settle in the flow or adhere to the pipeline walls. Batching pigs are used to separate different grades of product that is sent through the same pipeline. These are more commonly used on long transmission pipelines. Displacement pigs are used for removing or purging a pipeline of a fluid. Specialty pigs such as spray pigs can be used to apply inhibitor coatings to the top of the pipeline walls. Other pigs such as gauging pigs are used to identify dents or other anomalies. Some of these pigs can be seen in Figure 5.



Figure 5: The large array of pipeline utility pigs. Courtesy of T.D. Williamson.

One thing that is common among all pipeline pigs is that they are propelled through the pipeline via differential pressure. This differential pressure is formed across a sealing element that, in most cases, does not allow flow to bypass the pig. Therefore, the pipeline flow and pressure, which is created by the pumps, propel the pig down the pipeline. If this seal is broken, the pig will stall. Therefore, this sealing element must maintain a good seal against the internal face of the pipeline wall and deliver the propulsion force to move the pig. In present day pipeline pigs, the most preferred material is polyurethane elastomers. In figure 4 and figure 5 above, the polyurethane is cast with a red pigment and is easily identifiable. These sealing elements also provide the structure to keep the pigs centered in the pipeline. In the case of cleaning pigs, they can be designed to improve cleaning effectiveness.

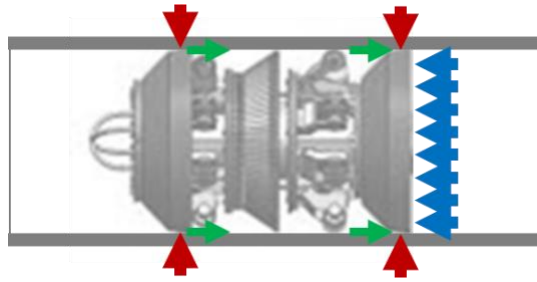


Figure 6: The friction force (green), normal compression load (red), and resultant differential pressure (blue) encountered in a typical pigging operation.

It is widely known in the pipeline industry that, “there is no such thing as a perfect pipeline”. This “perfect pipeline” would be straight with no tees, valves, or other obstructions, perfectly round, smooth with no weld beads, check valves, dents, metal loss, no internal diameter changes, steady flowrate, no corrosive materials, ambient temperature, and low pressure. However, because we do not live in this ideal world, all pipeline pigs must adapt to the widely varying environments of the pipeline. Some obstacles for pigs include navigating continuous and mitered bends, tees and wyes, features such as valves, check valves, signalers, sensors, and internal diameter changes such as wall thickness increases in heavily populated areas or increasing or decreasing pipeline size as lines branch off or combine to the main

Therefore, the sealing element of the pig must be flexible enough to contour around such conditions, strong enough to carry the pig’s weight and transfer the propulsion force to the pig body, and tough and resilient enough to withstand cyclic loads, sharp objects, abrasive internal surfaces, high pressure chemicals, temperature variations, and fluctuating flowrates. It is easy to begin to understand how incredibly demanding the requirements are of the sealing elements of the pipeline pig and the polyurethane material.

It should not come as a surprise then, that in some instances, these sealing elements do fail in the pipeline. Pipeline pig failure can be the result of many issues, and most of the time there are multiple issues coupled. Postmortem analysis of these failures can be time and resource

intensive on both the pipeline operators and engineering consulting company. Typically, DFSS approaches are taken to find root-causes. Some failure causes that are typically speculated and investigated are:

- 1) **Static forces:** These are the forces that act on the pig while it is inside the pipeline. These include forces such as friction, buoyancy, weight, pressure, and compression. These can vary as the pig navigates changing pipeline conditions (e.g. internal diameter reductions, valves, and bends).

- 2) **Transient effects:** This is an investigation of transient effects caused by the speed of the pig. High velocities can cause an increase in sealing element vibrations which accelerate heat buildup and material fatigue.

- 3) **Manufacturing and quality variations:** Due to the sensitive nature of the manufacturing of polyurethane, material properties can vary from batch to batch.

- 4) **Temperature, pressure, and chemical effects:** Temperature has a significant effect on the mechanical and chemical properties of polyurethane. In addition, degradation from chemicals present in the pipeline is accelerated from the high pressure environment, further decreasing mechanical properties.

- 5) **Viscoelastic behavior:** Due to the time dependency of polyurethane properties and the long durations a pig takes to travel through the pipeline. The viscoelastic nature of PUR can have an influence on performance and material behavior.

- 6) **Pipeline pig design:** It is arguable that the design of the sealing element and the pig in general plays the most crucial role in the success of the pigging operation. The pigging engineers have a wide range of options that allow for infinite configurations and designs. Mistakes made by operators and engineers in choosing the correct pig can result in failures.

Therefore, it is the primary intent of this work to provide answers and insight into a better understanding of these material questions. The manufacturing parameters that contribute to the largest property variations will first be characterized. This includes increasing the operation envelope and improving material reliability.

CHAPTER II

Section 2: BACKGROUND AND LITERATURE REVIEW

2.1 Polyurethane

In 1937, in the Main Scientific Laboratory of I.G. Farbenindustrie, Otto Bayer and his team of chemists first discovered and developed polyurethane (PUR) [11]. Since then, PUR's have been the main focus of many studies to improve or understand processability, chemistry, and mechanical, thermal, or chemical properties. For this reason, PURs have become a large commercial success. Cast PURs are used in a wide range of industries including, wheels and tires, oil and gas, mining, defense, medical, electronics, automotive, food processing, packaging, and recreation [12]. PURs high abrasion resistance, long-term stability, good cut and tear resistance, high load bearing, and ability to be cast into large segments are some of the reasons for their wide appeal and success. The processing methods of PUR materials are just as versatile and abundant. This includes casting, milling, Banbury mixing, calendaring, extruding, injection/compression/transfer/centrifugal molding, and solution applications [13]. In the manufacturing of thermosetting PUR parts, the fabricators mix the different components of isocyanate, polyol, chain extender and any additional additives each time a component is produced. Therefore, to insure quality and consistency of products, variables such as chemical component purity, catalyst type and amount, mixing ratios, and environmental conditions such as processing temperature, curing, and humidity all play a role.

As C. S. Schollenberger, in M. Morton's *Rubber Technology* text states, "so, it is clearly quite important that the liquid process fabricator understand and practice the proper chemistry in all operations" [13]. In addition, the morphology of the PUR plays a role. This is typically determined by the polymer chemistry, mold design, pouring process, and curing. Therefore, the chemistry of polyurethane components and their crosslinking will first be discussed. Next, the mechanical properties that are important to characterize PURs by design engineers for intended applications will be presented.

2.1.1 Polyurethane Chemistry

Polyurethane is a nonhomogeneous, crosslinked block copolymer which consists of a hard segment (HS) and a soft segment (SS). It can be mixed as either a thermoset or a thermoplastic. Alger defines polyurethane as a polymer which contains a urethane group in its chain [2]. A urethane group is generally formed from the reaction between an isocyanate function group (-NCO) and a hydroxyl group (-OH). Moreover, the reaction between an isocyanate group and an amine (-NH₂) will result in a similar urea linkage. These reactions are illustrated below in figure 7. This reaction is a rapid exothermic reaction [3]. Primary and secondary hydroxyls can be used, whereas tertiary hydroxyl groups result in an unstable urethane group which decompose into olefins. In order to insure the creation of large polymer networks, a diisocyanate is used. This is simply a molecule with two isocyanate function groups at both ends. In addition, a diol must be used to react with the diisocyanate. Generally, both a short chain and a long chain diol will be used to form the hard and soft segments, respectively, as shown in figure 8.

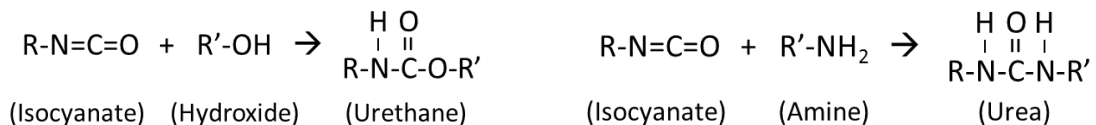


Figure 7: Chemical reaction for urethane and urea linkages.

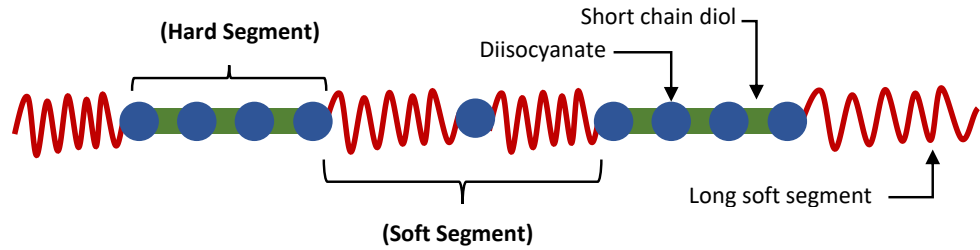


Figure 8: Diagram of soft and hard segments in a block copolymer polyurethane chain. Red: soft segment chain, Blue: diisocyanate, Green: Short segment diol (e.g. 1,4 Butanediol).

The reaction of the diisocyanate with the short chain diol or diamine, also called the chain extender, will result in a region known as a hard segment. The reaction between the diisocyanate with a much longer soft segment oligomer, typically a high molecular weight polyol, will give the soft segment. Due to the immiscibility of the hard and soft segment, microphase separation is present [4]. This is referred to as microphase separated morphologies [5]. The amount of miscibility between the hard and soft segments can be predicted using a classical thermodynamic approach. Further information on the theoretical approach for determining miscibility can be found in appendix E.

It has been shown that the thermal and mechanical properties of high molecular weight multiphase thermoplastics, such as polyurethane and poly(urethane urea), are dependent on the following three microstructure characteristics [6]:

- 1) The amount of microphase separation between hard and soft segments
- 2) Degree of hydrogen bonding within the hard segments
- 3) Degree of crystallization of the hard segment

Bonart and Müller proposed the metric of degree of separation (α_{seg}) and the ability to measure it using small-angle X-ray scattering [$\alpha_{seg} = \overline{\Delta\rho}_{exp}^2 / \overline{\Delta\rho}_{theor}^2$] based on Porod's theory of low-angle scattering [7]. Camberlin and Pascault later suggested that the degree of separation could also be acquired using DSC results. Using the change of the heat capacity at the glass

transition, the change in heat capacity of a pure soft segment oligomer ($\Delta C_{p,SS}$) was compared with the change in heat capacity per gram of block polymer ($\Delta C_{p,Block}$) giving the relationship [$\alpha_{seg} = \Delta C_{p,Block} / \Delta C_{p,SS}$] [8]. However, due to the greater free volume of soft segments compared to block urethane, $\Delta C_{p,Block} > \Delta C_{p,SS}$ could occur giving $\alpha_{seg} > 1$. Therefore, a proportionality coefficient K_S and a normalization of $\Delta C_{p,Block}$ by volume fraction of the soft segment (ϕ_{Block}) has been proposed [9, 10].

$$\alpha_{seg} = \left(\frac{\Delta C_{p,Block}}{\Delta C_{p,SS} \phi_{Block}} \right) K_S, \quad (eq. 2.1)$$

Where,

$$K_S = \frac{N_A \sum \Delta V_{ru}}{M_{ru} / \rho_{Block}} \quad (eq. 2.2)$$

With, N_A is the Avogadro number, ΔV_{ru} the volume of a repeating chain, M_{ru} the molecular weight of the repeating chain, and ρ_{Block} the density of the block.

The three main constituents used to react polyurethane polymers, as discussed above, are isocyanate, a long chain oligomer, and a short chain diol. The diisocyanate is a molecule, typically an aromatic or saturated (alkane) or unsaturated (alkene and alkyne) aliphatic, with two isocyanate functional groups on its ends. Aromatic structured diisocyanates typically have much quicker reaction times than aliphatic diisocyanates (e.g. MDI compared with its aliphatic homolog HMDI [5]). Diisocyanates are synthesized through phosgenation (most common) which is the reaction between a phosgene and the salt from a primary amine [11]. Other methods include double decomposition reactions, Curtius, Hofman, and Lossen rearrangements, or preparation from other isocyanate derivatives to name a few [11]. This molecule is a strong electrophile. Its reactivity with other molecules has been studied by Entelis et al. who show its strong reactivity

with urea, water, and hydroxyl groups [12]. The reactivity of aromatic isocyanates with different hydrogen containing compounds is shown below in table 1.

Hydrogen Compound	Chemical Structure	Relative Reaction Rate
Primary Aliphatic Amine	R-NH ₂	100000
Secondary Aliphatic Amine	R ₂ -NH	20000-50000
Primary Aromatic Amine	Ar-NH ₂	200-300
Primary Hydroxyl	R-CH ₂ -OH	100
Water	H ₂ O	100
Carboxylic acid	R-CO-OH	40
Secondary Hydroxyl	R ₂ CH-OH	30
Tertiary Hydroxyl	R ₃ C-OH	0.5
Urethane	R-NH-CO-O-R	0.3
Amide	R-NH-CO-R	0.1

Table 1: Relative reaction rates of aromatic isocyanates with hydrogen containing compounds. [5, 13]

From table 1 above, it can be seen that the reactivity of an aromatic isocyanate with water is higher or equivalent to hydroxyl groups and lower than its reactivity with amines. For this reason, it is believed that the effects of humidity on a polyurea blend will not be as severe as its effects on polyurethane. For polyurethane foams, water is added into a mixture as a blowing agent. When this is done, the water will first react with the isocyanate forming a carbamic acid which quickly decomposes into an amine and a carbon dioxide [14]. Next, the amine will react with an additional isocyanate to form a urethane. With proper design of the ratios, the released carbon dioxide will begin a foaming reaction to produce either open or closed cell foams. The amount of water and the correct catalyst must be carefully controlled to allow for the correct amount of released carbon dioxide to start the foaming reaction with sufficiently strong cell walls. Polyurethane foams are not a focus of this study.

Some of the most common diisocyanates used today are 4,4'-Methylenediphenyl (MDI) and 2,4-Toluene, both aromatic. Some other, less common diisocyanates available are Bis(4-

isocyanatocyclohexyl) (HMDI) an aliphatic homolog of MDI, hexamethylene (HDI), and Isophorone (IPDI) a highly asymmetric aliphatic. These are shown in table 2.

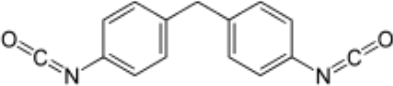
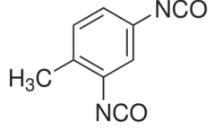
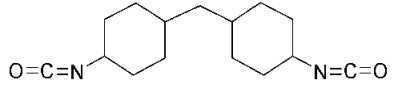
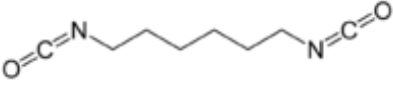
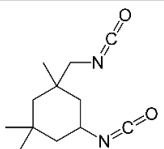
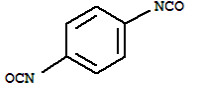
Diisocyanate	Abbreviation		Molar Mass (g/mol)	Chemical Structure
4,4'-Methylenediphenyl	MDI	aromatic	250.25	
2,4-Toluene	TDI	aromatic	174.2	
Bis(4-isocyanatocyclohexyl)	HMDI	aliphatic	258.32	
Hexamethylene	HDI	aliphatic	168.2	
Isophorone	IPDI	aliphatic	222.3	
1,4-Phenylene	PPDI	aromatic	160.13	

Table 2: Commonly used diisocyanates.

Polyols are used to create the long chain, soft segments of the polyurethane chains. Many polyols have been experimented with and are available on the market. These long chains have hydroxyl function groups, which react with the isocyanate to create urethane linkages. Some polyols can have more than two hydroxyl groups such as trifunctional or more. Polyols can be carbon chains that are ether, ester, or carbonate based. The most common synthesis method for polyester polyols, which is used in this study, is through transesterification, antihydride addition, and condensation. The molecular weight can be altered by varying the acid to glycol ratio during synthesis. Moreover, controlling the ratio of ethylene and propylene glycol used can vary melting point and hydrolysis resistance [15]. However, the ester linkage in polyester based urethane is very sensitive to hydrolytic cleavage compared to other polyether based urethanes. A fairly new

type of polyol with use of alkyl side groups (PDPAd) has been demonstrated to exhibit improved hydrolytic stability for polyurethane aquatic dispersions [16]. Some of these polyol chemical structures are illustrated in table 3.

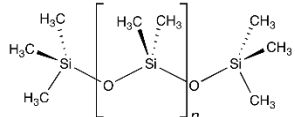
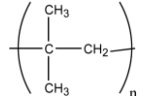
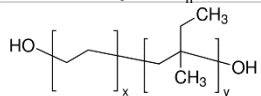
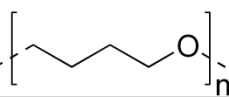
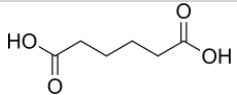
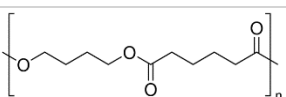
Soft Segment Polyols	Abbreviation	Chemical Structure
Polydimethylsiloxane	PDMS	
Polyisobutylene	PIB	
Poly(ethylene butylene)	PEB	
Poly(Tetramethylene ether)glycol	PTMEG	
Polyester (adipic acid)		
Poly(butylene adipate)	PBA	

Table 3: Common polyols and their chemical structures.

Similar to the long chain soft segment polyols, a short chain diol is also used in polyurethane synthesis. These are considerably smaller molecules in comparison with the soft segment polyol. In this thesis, a 2000 g/mol polyol, and in comparison, a 1,4 butandiol with a molecular weight of only 90 g/mol (x22 smaller). The short segment diol reacts similarly with the isocyanate to create a diol-urethane-diol chain. Commonly used chain extenders are summarized in table 4. This is the hard segment portion of the chain due to the higher density of urethane linkages and shorter chains. The closer proximity of the urethane linkages allows for more hydrogen bonding between chains. The presence of a higher hydrogen bonded phase results in improved mechanical properties. The reaction of the microphase hard segments to an applied load is illustrated in figure 9. The chain extender can also be amine terminated, which creates a urea linkage.

Chain Extender	Abbreviation	Molar Mass (g/mol)	Chemical Structure
Ethylen Glycol		62.1	<chem>OCCO</chem>
1,4-Butanediol	BD	90.12	<chem>OCCCCO</chem>
Dipropylene glycol		134.17	<chem>CC(O)COCC(O)C</chem> <chem>HOCCOCCOCCO</chem>
Hydroquinone bis(2-Hydroxyethyl ether)	HQEE	198.22	<chem>OCCOC1=CC=C(OCCO)C=C1</chem>
4,4'-Methylenebis(2-chloroaniline)	MOCA	267.15	<chem>Nc1ccc(cc1Cl)C2=CC=C(N)C=C2Cl</chem>
4,4'-Methylenedianiline	MDA	198.27	<chem>Nc1ccc(cc1)C2=CC=C(N)C=C2</chem>

Table 4: A list of hydroxide and amine based chain extenders and their chemical structures.

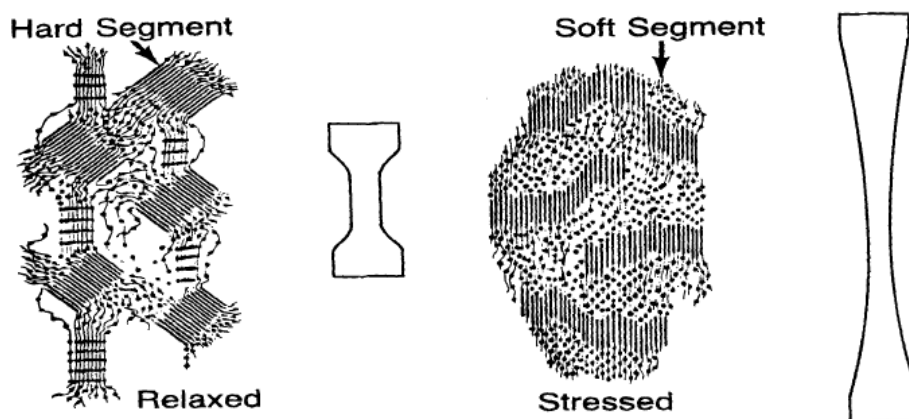


Figure 9: polyurethane microstructure reaction to applied stress. Strong hydrogen bonded hard segments provide strong mechanical resistance [17].

Finally, the last component which is critical to the polyurethane reaction is a catalyst. Catalysis of the polyol/isocyanate reactions is required to achieve proper reaction rates for manufacturing. Some common catalysts are metal salts, organometallic compounds, and tertiary amines. Bases, acids, and water can also act as catalyst. These catalysts can be used to either decelerate or accelerate the reaction. Some decelerating agents are water through hydrolysis, pigment through absorption, solvents through solubility, and acids in the formation of inactive

salts [18]. In general, a good catalyst is one which is a strong nucleophile, capable of creating an active hydrogen amine complex, and soluble in water and able to form strong hydrogen bonds with the water [14].

The amount of hard segment content in a polyurethane by weight can be estimated with equation 2.3 [5]. The molar percentage can also be calculated by simply multiplying by the corresponding molecular weights. Increasing the percent HS, leads to increased elastomer hardness and modulus due to the larger hard segment regions.

$$HS \text{ (wt\%)} = \frac{\text{weight}(\text{diisocyanate} + \text{chain extender})}{\text{weight}(\text{total polymer})} * 100, \quad (\text{eq. 2.3})$$

Moreover, the index of a polyurethane mixture can be calculated using equation 2.4. The index is an important number that describes the mixing ratio of the polyurethane material. Simply, this is a ratio of the functional groups (NCO/OH) in the mixture [19].

$$\text{Index} = \frac{\text{diisocyanate}}{\text{polyol} + \text{chain extender}} = \frac{\frac{W_{NCO}}{\bar{E}_{NCO}}}{\frac{W_{polyol}}{\bar{E}_{polyol}} + \frac{W_{chain \text{ extender}}}{\bar{E}_{chain \text{ extender}}}}, \quad (\text{eq. 2.4})$$

where \bar{E} is the equivalent weight (\bar{Mn}/f), Mn is the molecular weight, f is the functionality, and W is the weight. The functionality of a diisocyanate, polyol, diamine, and diol is 2. Another mixture parameter sometimes cited by manufacturers is the mixture stoichiometry. This is simply the inverse of the index (OH/NCO). An index equal to unity is a perfectly stoichiometric mixed urethane. An index that is greater than unity is NCO rich.

2.1.2 Crosslinking

The reaction of polyurethane follows a second order reaction rate, but as the urethane linkages become more prevalent, side reactions become more common. Therefore, higher order reaction rates are observed [20]. This is due to any extra isocyanate in the mixture reacting with

the N-H group in the urethane or urea linkage. This leads to allophanate (-NCO + urethane) and biuret (-NCO + urea) branching. Isocyanates react slowly with urethanes to form allophanates. Allophanates are thermally unstable and begin to dissociate at temperatures above 106 °C [11]. Biuret links are more stable and begin to dissociate at 130-145 °C [11].

These side reactions can be heavily affected by the choice of an aromatic or aliphatic diisocyanate. The addition of an aromatic ring connected to the -NCO group can increase the electronegativity, and therefore it can impact the reaction rate at lower temperatures. It has been shown that Allophanate formations are favorable with aromatic diisocyanates at mixing temperatures above 60 °C [21]. These additional reactions can have a large effect on the consumption of isocyanates. Therefore, they require extra isocyanate in the mixture. Otherwise, they result in polymers with a lower index than expected.

Other network forming molecules derived from the reaction of isocyanates in urethane are uretidinedoine (dimerization), isocyanurate (trimerization), carbodiimide, and oxazolidone [4, 22]. The thermal stability of these linkages are isocyanurate > oxazolidone > carbodiimide > urea > urethane > biuret > allophanate [4]. These linkages can exist in the polyurethane copolymer in different varieties depending on the isocyanate index and mixing conditions. Higher crosslink densities can result in enhanced mechanical and temperature properties. See table 5 for structures of some crosslinking formations.

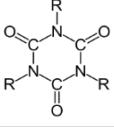
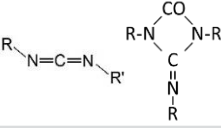
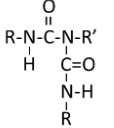
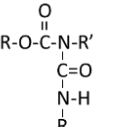
Crosslinkers and Isocyanate Derivatives	Thermal Stability	Chemical Structure
Isocyanurate		
Carbodiimide		
Biuret	130-145	
Allophanate	106	

Table 5: List of crosslinking molecules derived from isocyanate reactions within the molecular structure of polyurethane.

In areas of urethane rich hard segments, the proximity of the urethane and urea linkages in well-structured elastomers produce what has been described by Schollenberger as a “virtual crosslink” (VC) [22]. The hard segments aggregate, and hydrogen bonding forms between the urethane/urea hydrogen atoms and the urethane, urea, ester carbonyl, or ether oxygen groups of a nearby chain. Urethane hydrogen bonding is considered monodentate whereas urea groups can produce a bidentate hydrogen bond. Quantum mechanical calculations (QMC) have shown that the hydrogen bonding between urea groups is 58.5 kJ/mol compared to a urethane-urethane bond of 46.5 kJ/mol [23]. These hard segments can consist of branched crosslinking or virtual crosslinking and give the elastomer many of its mechanical properties.

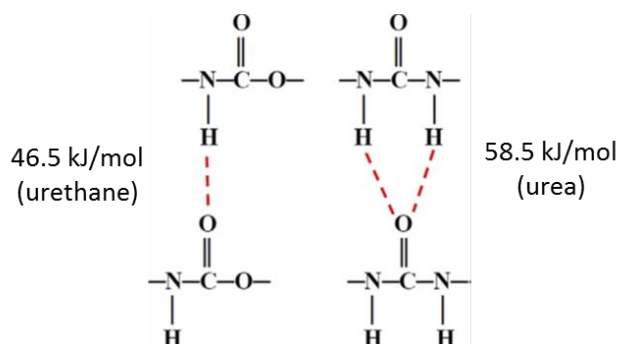


Figure 10: Monodentate and bidentate hydrogen bond between urethane-urethane and urea-urea molecules, respectively. Hydrogen bonds may also form with ester carbonyl groups, not illustrated here [5, 23].

2.1.3 Polyurethane Synthesis

During the preparation of polyurethane copolymers, the procedure taken can have an effect on the microstructure produced. There are two primarily distinct methods, one-shot and prepolymer. However, a “quasi-prepolymer” method has also been described and is commonly used in industry.

In the one-shot method, as the name implies, all reactants (diisocyanate, soft segment oligomer, and chain extender) are mixed together at once at the desired ratios. This method is generally carried out in bulk, and there is no need for a solvent. However, this method results in fairly random size distribution of hard and soft segments. This method is used for the production of thermoplastic resins, reaction injection molding (RIM), and foams.

The prepolymer polymerization method is a two-step process. In the first step, polyol is mixed with excess amounts of diisocyanate. This produces linear chains with isocyanate terminated ends and is called the “prepolymer.” This gives relatively low molecular weight chains, which allow for low melt viscosity. In the second step, the chain extender is added, which couples the prepolymer molecules to form a high molecular weight chain. This step also produces the urethane rich, hard segment. This method has the advantage of allowing for longer or shorter

soft segments by adjusting the diisocyanate/polyol ratio in the prepolymer. As this ratio approaches 1/1, the prepolymer can no longer accept chain extender and produces a linear, high molecular weight soft segment. This is also referred to as a millable polyurethane gum.

At prepolymer ratios of greater than 2, free floating diisocyanate can be achieved. This additional polyol and chain extender is then mixed in a three mixture setup. This method is referred to as “quasi-prepolymer.” This gives the advantage of a more structured elastomer product compared to the one-shot method, but it allows for similar viscosities between the components which is favorable for industrial manufacturing. This also tends to produce elastomers with larger hard segments due to the reaction of chain extenders with free diisocyanate.

Once the components are mixed, they are cured in an oven. Typically, a “green strength” is achieved within an hour, and the part can be demolded. Afterwards, a longer post cure cycle is needed to fully cure the elastomer. The cure can be monitored and quantified by measuring the hardness buildup of the material or through Fourier Transform Infrared Spectroscopy (FTIR) of the molecular evolution such as the strong isocyanate absorption peak (2270 cm^{-1}) [11, 24].

2.1.4 Polyurethane Additives

It is not uncommon to see polyurethane elastomers compounded with an additional filler. This can be done for many reasons including protection from hydrolysis, UV autoxidation, thermooxidation, microbiological attacks, and nitrogen dioxide attacks [22]. Moreover, the incorporation of filler particles into elastomers increases the stiffness (elastic modulus), alters the strain history dependence (the Mullins effects), and modifies the time-dependent aspects of material behavior such as hysteresis, creep, and stress relaxation [25]. Bergstrom and Boyce proposed that the variables which influence the mechanical behaviors are:

- 1) Size, type, and shape of the filler
- 2) Filler aggregate structure

3) Polymer-filler interface area

The loss of stiffness of an elastomer after an applied load has been shown to be independent of volume fraction of the filler, which Govindjee and Simo attributed to the breaking of molecular bonds in the matrix. Filled elastomers have also been shown to exhibit higher rate-dependence and larger hysteresis than unfilled elastomers. Models have been used to predict the upper and lower bound for the increased elastic modulus such as the Voigt upper bound and Reuss lower bound or the more restrictive Hashin-Shtrikman model [26]. However, due to the low modulus of the matrix and large filler modulus, these equations result with very large possible regions. Therefore, other elastomer composite models have been proposed. These are covered in the literature and will not be further reviewed here [25-29].

Many types of filler materials have been incorporated into polyurethanes. Some of these are carbon based additives such as ultra-thin graphite (0.5 wt% - 3.0 wt%), oxidized ultra-thin graphite, multiwalled carbon nanotubes, single walled carbon nanotubes, and carbon black [30-33]. Responses to these additives include increased crystallization temperature, increased thermal stability, and increased tensile strength and elongation. The addition of an oxidized layer onto the graphene significantly increased the interaction with the polyurethane matrix. The amount of oxidation can be tailored to give the properties desired. Single-walled CNT/polyurethane composites exhibited enhanced microwave absorption between 2-18 GHz with a maximum absorption of 22 dB at 8.8 GHz [33]. This additive allows for the possibility of microwave curing. Multi-walled carbon nanotubes have also been incorporated onto polyurethane sheets through direct-write additive manufacturing for force and slip detection tactile sensors [34]. Cork has also been used as a filler which results in increased Young's modulus and damping properties. However, a decreased elongation at break is common. Agar additives can lead to improved tensile strength and hydrophobicity, but it too causes reduced elongation at break. Rectorite nanocomposite resulted in some improved mechanical properties. Additives such as fibrin have

also been used to improve biocompatibility and bioinductivity [35]. Sustainable composites using natural fibers and castor oil have been studied [36].

Polyurethane provides endless abilities to tailor final material properties through chemistry alone (e.g. index, HS%, polyol molecular weight, diisocyanate), but it is now apparent that the addition of additives can also provide solutions to unique material requirements. However, a general trend exists in the literature that with the increase of ultimate strength comes a reduction in elongation. Moreover, the addition of fillers creates a large increase in viscosity. Increase of viscosity can create difficulties for processing. This increase can be modeled through many analytical models. The simplest is the Einstein equation for viscosity of suspensions [28].

$$\eta = \eta_1(1 + k_E\phi_2) \quad (eq. 2.5)$$

where η is the viscosity of the mixture, η_1 is the viscosity of suspending liquid, k_E is the Einstein constant ($k_E = 2.5$), and ϕ_2 is the volume fraction of filler. This equation has been shown to be accurate for fully rigid particles at a very low concentration. For higher concentrations, the Mooney equation has been shown to be more accurate [28].

$$\ln\left(\frac{\eta}{\eta_1}\right) = \frac{k_E\phi_2}{1 - \phi_2 / \phi_m} \quad (eq. 2.6)$$

Where ϕ_m is the maximum volume fraction that the filler can occupy. Theoretically, this is similar to the packing factor, therefore, $\phi_{m,theoretical\ max} < 0.74$ (hexagonal packing factor of perfect spheres). However, experiments have shown that this value is not always met due to agglomeration. Therefore, it is recommended that this value is calculated through experimental methods such as sedimentation measurements. Moreover, k_E in this equation is no longer constant. For spheres, if there is no slippage at the interface, $k_E = 2.5$. If slippage does occur, k_E can drop to 1.0. Moreover, if agglomeration into rough spherical clusters occurs, k_E can be estimated by

$$k_E = \frac{2.5}{\phi_a} = \frac{2.5(V_s + V_L)}{V_s} \quad (\text{eq. 2.7})$$

where ϕ_a is the volume fraction of an agglomerate made up of spheres, V_s is the actual volume of the spheres in a typical agglomerate, and V_L is the volume of the matrix entrapped inside the agglomerate. Therefore, it can be seen that larger agglomeration increases the viscosity build up. If nonspherical fillers are used, k_E can be calculated based on the aspect ratio. In the case of aggregated mixtures above the concentration value of ϕ_m , ϕ_2 is replaced with ϕ_2/ϕ_a in the Mooney equation. Other models exist such as Eilers-van Dijck, Roscoe, or Krieger-Dougherty equations. Also, non-newtonian effects can be taken into account and occur as ϕ_2 approaches ϕ_m ($\phi_2/\phi_m > 0.80$). However, these will not be reviewed further here.

The ability to improve overall material toughness (both strength and elongation) was explored with the addition of nanosilica. These property improvements were balanced with the rheological behaviors of the mixture. In order to achieve this, the nanosilica was pre-dispersed into the polyol. The nanocomposite resulted in improved toughness and thermal stability [37]. However, in this work, only three samples were poured (0% nanosilica, 2% and 4%), therefore higher statistical confidence is needed.

Polyhedral oligomeric silsesquioxanes (POSS) has been shown to improve the thermal stability and some mechanical properties when dispersed in polyurethane films to form a nanostructured, polymer-ceramic hybrid [38]. A unique aspect of the POSS composite is the incorporation of the POSS molecule into the polymer chain. Other examples of organic compounds incorporated into PUR are clay silicate layers (12COOH-montand BZD-mont) which, resulted in drastic increases in tensile strength and elongation with an additional improvement in water absorption. An addition of organophilic montmorillonite (OMMT) clay modified the storage and loss modulus by acting as a random nucleation zone [39, 40]. Micro and nano clays have also been shown to be a viable additive in polyurethane foams [41].

2.2 Material Properties

Due to their chemical structures, polyurethane, and more generally polymers, exhibit very unique mechanical and thermal properties. The objective of this study is to understand the effect of synthesis parameters on these properties. Two engineering approaches are used for capturing the full polymer responses. The *phenomenological experience* approach is based on repeating enough experiments to provide a good understanding of material response to a load case. This approach is the most common approach in industry. However, it has limitations of modeling for only exact loading conditions. A second approach is the *micromechanical model* approach. This method attempts to capture material mechanisms at a micro and nano scale, which are then translated into overall material behavior. However, even though these models are preferred, the complexity and difficulty for pure micromechanical modeling makes them less practical. Therefore, these models can be used by a material scientist as a bridge and guide to material design for desired behavior. [42]

In this work, the phenomenological responses will be captured. Next, if possible and the data allows, a micromechanical explanation for such behaviors will be given. For further reading on the micromechanical mechanisms, the reader is directed towards the literature.

2.2.1 Fracture

Fracture of a material has three primary stages; crack initiation, crack propagation, and finally, rupture once the crack has reached its critical length. Crack initiation, the first stage, can occur from cyclic or a monotonic load. Moreover, it can be an inherent defect preexisting in the material from manufacturing impurities. Inhomogeneities in the material such as undispersed additives, microvoids, or roughness from the mold surface can create localized stress concentrations for crack initiation to begin by forming microcracks [43]. Once the crack has reached a sufficiently large size, classical fracture mechanics can be used to model material

behavior. The load for crack initiation for polyurethane is commonly measured using die C test specimens of ASTM D-624.

Once a crack exists, the second state of fracture is the propagation of that crack. In order for crack growth, a minimum energy is required. For elastomers, this tear energy is defined as [44]:

$$T = -\frac{\partial U}{\partial a}; \quad T = \frac{2F}{t} \text{ (for trouser tear test) } \quad (\text{eq. 2.9})$$

where T is the tear energy, U is the elastically stored energy, A is the area of the crack. F is the load, and t the sample thickness. This definition is similar to the strain energy release rate of classical fracture of metals. The crack propagation of an elastomeric material can be characterized using the trouser tear test from either ASTM D-470 or ASTM D-624.

2.2.2 Fatigue

Due to the internal viscosity of an elastomer, these materials exhibit hysteresis. As a material is deformed, the uncrosslinked segments become mobile. This mobility is both temperature and strain rate dependent. As the temperature is lowered toward the glass transition temperature, a maximum in the fractional energy absorbed (H) reaches a maximum before the glass transition temperature. At sufficiently high temperatures, the material is rubberlike. At low temperatures, the material becomes more glasslike and does not experience as much motion. Therefore, this maximum is observed between these two phenomena [45]. Hysteresis can cause large heat buildup in bulk materials with low thermal conductivity and can cause failures. Thinner cross sections are used by designers to counter this effect [46].

Fatigue cracking is the appearance of cracks under cyclic tensile deformation, which grow under additional loading resulting in failure. The crack growth per cycle (dc/dn) can be related to the tearing energy (T) through an empirical relationship similar to that used in linear elastic fracture mechanics (LEFM).

$$\frac{dc}{dn} = A(\Delta T)^{m'}, \quad (\text{eq. 2.10})$$

Where ΔT is the cyclic range of T , and A and m' (value of 1-3.5 for elastomers) are scaling parameters dependent on material structure, frequency, temperature, environment and stress ratio. This is similar to the Paris-Erdogan law for fatigue. Amorphous elastomer crack growth is constant with an increase in tear energy, whereas strain crystallizing elastomers grow continuously only after a tear energy threshold is exceeded [45]. Multiple levels of crack growth exist depending on the tearing energy as shown in the table below.

Tearing Energy	Crack growth rate
$T < T_o$	No crack growth ($dc/dn < 10^{-7}$ mm/cycle)
$T_o < T < T_t$	Growth proportional to $T - T_o$ (eq. 16)
$T_t < T < T_c$	Growth proportional to T^2
$T \geq T_c$	Abrupt tearing ($dc/dn > 10^{-4}$ mm/cycle)

Table 6: Level of crack growth depending on tearing energy. T_o is the tearing threshold, T_t is the transition threshold, and T_c is the critical threshold. [60, 61]

2.2.3 Viscoelasticity

Polyurethane, like many polymers, exhibits a frequency and temperature dependence. The mechanical analog of a polymer comprises of both a spring (linear effects) and a damper (nonlinear effects). Some common models used to describe this behavior in polymers are both the Maxwell and Voigt model [47, 48]. The combination of these two analogs can be used to create more accurate models such as the generalized Maxwell model used in common finite element analysis software.

When a sinusoidal load is applied to a sample, due to the viscous nature of the material, a delay in the strain response is exhibited [49]. The ratio between the stress and strain amplitude is called the dynamic modulus, E^* .

$$E^* = \frac{\sigma_o}{\varepsilon_o}, \quad (\text{eq. 2.11})$$

Using the dynamic modulus, the storage modulus and loss modulus can be defined as:

$$\text{Storage Modulus: } E' = E^* \cos(\delta), \quad (\text{eq. 2.12})$$

$$\text{Loss Modulus: } E'' = E^* \sin(\delta), \quad (\text{eq. 2.13})$$

Finally, tan delta is the ratio of loss modulus to storage modulus:

$$\text{Phase Angle: } \tan(\delta) = \frac{E''}{E'}, \quad (\text{eq. 2.14})$$

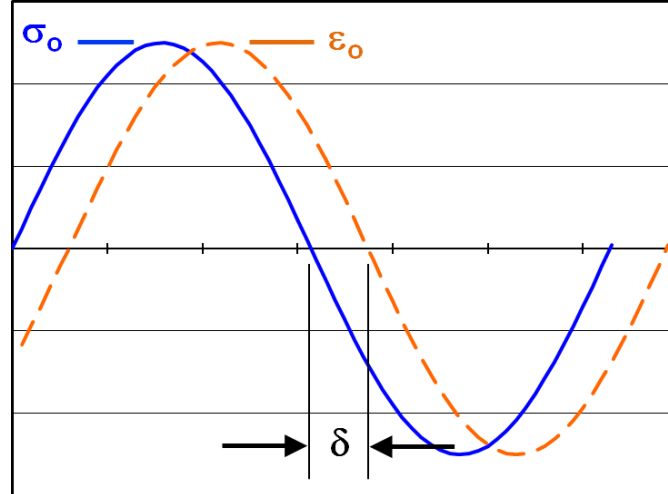


Figure 11: Viscoelastic response of material to sinusoidal excitation load. Blue line represents the applied load and the dashed orange line is the lagging strain response [65].

2.2.4 Creep and Stress Relaxation

Due to the additional viscoelastic nature of polymers, especially elastomers, they often exhibit time dependent behavior. Two responses are material creep and stress relaxation. Creep is

additional strain encountered after the initial constant load has been applied [50]. Stress relaxation is the reduction in material stress after an initial strain is applied. The figures below show a response of the mechanical analogs; Maxwell, Voigt, and standard linear viscoelastic models response to a constant load and constant strain step function [51]. These models are adequate for a fundamental understanding of these phenomena. However, more complex models such as the generalized Maxwell model is used for more accurate material modeling.

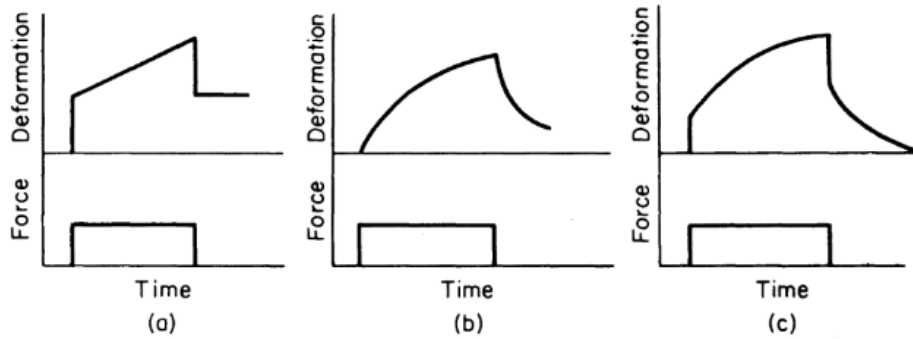


Figure 12: creep response with a force step function applied. Responses to different linear viscoelastic models are: Maxwell model (a), Voigt model (b), Standard Linear model (c). [67]

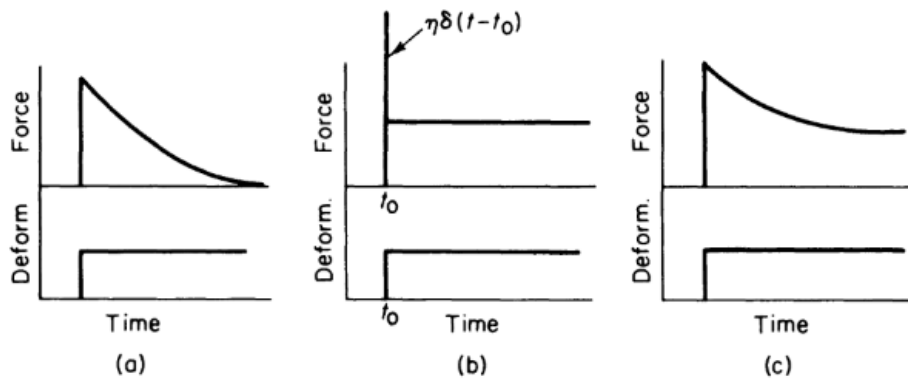


Figure 13: Relaxation models with a strain step function applied. Maxwell response (a), Voigt response (b), Standard Linear (c). [67]

2.2.5 Abrasion Resistance

The ability of a material to withstand rubbing, scraping, or erosion from cyclic loading against another surface is the abrasion resistance of that material. Abrasion in elastomers is

attributed to a process of micro-tearing at the surface contact with sharp asperities. This process begins at a structural unit or stress concentration causing the removal of small particles (1-5 μm) leading to a pitted surface followed by larger particle removal ($>5 \mu\text{m}$) [52, 53]. Because mechanical failure at a microscopic level is closely related to abrasion, fracture fatigue mechanics, specifically tearing energy, has been used as a mechanism of abrasion characterization [54].

$$\text{Abrasion Loss} = \frac{KE'Ft}{u_t} = \frac{kE'\mu wt}{u_t}, \quad (\text{eq. 2.15})$$

Where u_t is the tearing energy (can also be substituted with $\sigma_{ultimate}\epsilon_{break}$), F is the tangential friction force, μ is the coefficient of friction, w is the normal load, E' dynamic Young's modulus, k is a constant, and t is the time duration. For further reading, the reader is directed to the additional literature [55].

Polyurethane has been shown to have very good abrasion resistance (10x longer) as compared to natural rubbers. Silicon oil, molybdenum disulfide, or graphite has been shown to add a self-lubricating effect [46]. Both the Taber Abrasion (ASTM D-1044) and NBS Index (ASTM D-1630) can be used for abrasion characterization. However, the comparison of performance data between labs is not recommended due to the large variability of lab results.

2.2.6 Tensile Properties

Tensile properties are material properties derived from the stress-strain curves. Unlike metals, polymers and elastomers do not exhibit linear, Hookean behavior. The compression and tensile behavior can show enormous differences as compared with linear metallic materials. The elastic modulus (Young's modulus) for polymers is given at a specified strain (i.e. 100%, 200%, or 300%). The strain and stress at break is also a common output as elongation and tensile strength, respectively. The tensile toughness of an elastomer is the area under the entire curve. With elastomers, the strain rate, temperature, strain history (Mullins effect), and modes of loading

(i.e. uniaxial tensile, compression, planar shear, etc.) can have a large effect on the stress-strain behavior. Moreover, elastomers exhibit a hysteresis in the stress-strain behavior which contributes to the heat generation of the material under cyclic loading. The initial stress-strain behavior of a polymer after demolding is referred to as the green strength. After this, the material will exhibit lower modulus values. Figure 14 shows the stress relaxation and Mullins effect response of a 75 Shore A polyurethane elastomer as tested.

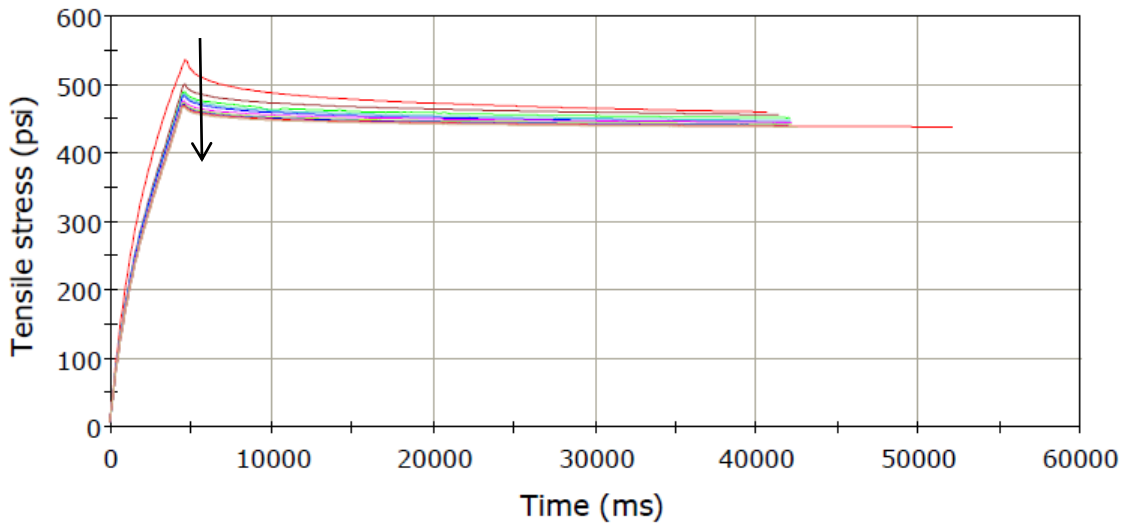


Figure 14: 10 cyclic loadings of a 75 Shore A polyurethane elastomer to 100% strain with a 40 second hold.

2.2.7 Glass Transition Temperature

The glass transition phase transformation is a unique characteristic of polymers. Above this temperature, the material exhibits a rubbery state. Below this temperature, it exhibits a hard and brittle state. The glass transition is a transition which affects the amorphous portion of a polymer. A differential scanning calorimeter (DSC) can be used to measure the glass transition temperature (T_g) and enthalpy change when the glass transition temperature is passed. At the T_g , there is an increase in heat capacity, but there is no latent heat. Since this transition only affects the amorphous portion of a polymer, T_g is commonly used to characterize the degree of crystallinity

of a polymer. For polyurethane, it is observed that the hard segment does not exhibit a T_g . Therefore, any transition is attributed to the amorphous soft oligomer.

2.2.8 Hardness

A common hardness measurement for elastomers is the shore durometer. This is a measure of the indentation of the material under a constant load. In comparison, other hardness test techniques measure the residual indentation after the load has been removed. Therefore, shore durometer is a general measure of the materials compliance and a characterization of the material's plastic flow [28]. However, attempts to find a correlation between hardness and Young's modulus have been ineffective [42]. This could be attributed to the large variance in Young's modulus with its dependency on time and temperature. The ASTM shore A hardness tester is common in industrial applications of polyurethane. This tester utilizes a truncated cone indenter loaded by a calibrated spring. The Shore A value is a representation of the distance of penetration (h) and spring compression load. The depth of penetration can be modeled using the Hertz equation:

$$h = \left[\frac{3}{4} \left(\frac{1 - \nu_1^2}{E_1} + \frac{1 - \nu_2^2}{E_2} \right) \right]^{2/3} F^{2/3} R^{-1/3}, \quad (eq. 2.16)$$

where E_1 is the Young's modulus of the indenter, E_2 the Young's modulus of the specimen, ν_1 the Poisson ratio of indenter, ν_2 the Poisson ratio of the specimen, F is the load applied, and R is the radius of the indenter.

2.2.9 Processability

Polyurethane is a unique polymer since it has the ability of forming either a thermoset or thermoplastic. This ability allows for its tailoring to the manufacturer's needs. A thermoplastic is a material, which has the ability of being reformed after it has cured by subjection to elevated temperatures and a forming pressure. However, due to the strong covalent crosslinking formed in

thermosets, they cannot be reprocessed. Therefore, the scrap rate can be quite high and costly for thermoset manufacturers if the process is not controlled correctly.

Thermoset plastics begin as separate chemical liquids and gels. Once they are mixed, the chemical reactions begin. The progress of the reaction is evident in the viscous build up from a Newtonian fluid into a networked polymer. During the viscous buildup, a gel point is crossed when the material ceases to flow and is no longer processable. At this point, physical material properties such as Young's modulus and hardness begin to develop. The stage after the gel time is called the cure time. Prior to the gel point, the viscous buildup can be measured with a rheometer. Afterwards, a number of techniques are available to monitor the cure. Some popular methods include hardness buildup or NCO content.

A distinction is made between gelation, molecular and macroscopic gelation. Molecular gelation is the point at which the resin becomes insoluble or the loss modulus becomes frequency independent. This gelation point is dependent on the functionality, reactivity, and stoichiometry of the mixture. In contrast, macroscopic gelation is the point at which the viscosity passes a threshold and approaches infinity. At the point of gelation, the chemical conversion (degree of cure) may only be 50-80%. Vitrification can occur during the mix if the cure temperature drops below the glass transition temperature of the forming cure. To avoid this, the cure temperature must be held well above the T_g of the fully cured polymer. Vitrification results in a large reduction in the reaction rate. T_g of the components premixing can be used as a recommended storage temperature. Below this temperature, chemical degradation is slowed down, increasing the shelf life of the product.

Calculation of the curing kinetics of a mixture can be calculated using proposed methods [56]. However, difficulties arise with variable component reactivity, functionality, and addition of a catalyst.

2.3 Characterization Methods

Although there are many characterization techniques available for polymers, only the methods utilized in this study are discussed in this section.

2.3.1 Dynamic Mechanical Analysis

Dynamic mechanical analysis (DMA) is a versatile material analysis technique used to study viscoelastic behaviors as a function of temperature and frequency. Samples can be tested under multiple modes of loading using a variety of clamps such as dual or single cantilever, tension, compression, and two-point bending. Loading profiles can also be varied such as multifrequency sweeps (variable frequency, sinusoidal oscillations), creep (constant load), stress relaxation (constant strain), and stress-strain (steady increase of load). The chamber temperature may be increased or decreased to study temperature dependent properties such as the glassy plateau ($\tan(\delta) < 0.01$), glassy transition region ($0.1 < \tan(\delta) < 1.2$), leathery region ($\tan(\delta) < 1.0$), rubbery plateau ($\tan(\delta) \approx 1.0$), viscous region ($\tan(\delta) > 1.0$), and the fluid region ($\tan(\delta) \gg 1.0$) [57]. Moreover, the frequency of the applied load can vary. The outputs of the instrument are storage modulus (E'), loss modulus (E''), and phase angle ($\tan(\delta)$). However other parameters relevant to the mode of testing can also be output. These parameters are used to characterize the materials viscoelastic behavior. Storage modulus is the elastic response, loss modulus the viscous response, and $\tan \delta$ the ratio between the two [48]. Further discussion of these properties can be found in section 2.2.3.

2.3.2 Tensile Testing

Tensile testing is one of the most common testing techniques for characterizing material properties and is used to create stress-strain relationships. This can be performed under multiple loading modes such as uniaxial tension, uniaxial compression, biaxial tension, planar shear, simple shear, and volumetric test [58]. These tests are used for setting up nonlinear hyperelastic

(neo-hookean) models used in finite element material models such as Mooney-Rivlin, Gent, Arruda-Boyce, Yeoh, Ogden, and others, which can be found in commercial software.

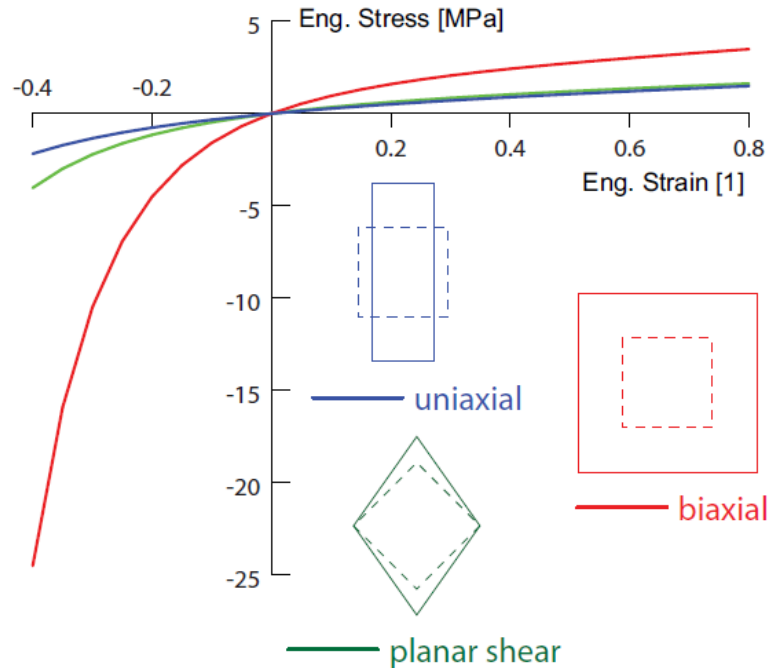


Figure 15: Different modes of tensile testing used in hyperelastic modeling of material behavior.

[73]

Moreover, tensile machines are capable of characterizing fracture parameters. For polymers, relevant test includes trouser tear (ASTM D-470 and D-624) and die C tear test (ASTM D-624). Tensile testing is commonly done on a dumbbell shaped sample according to ASTM D-412.

2.3.3 Fourier Transform Infrared Spectroscopy

A Fourier transform infrared spectroscopy (FTIR) is a method used to analyze the types of molecular bonding in a material. A sample is irradiated with an IR radiation signal causing stretching and bending of the present bonds. The amount of absorbed, transmitted, and reflected signals is captured as the wavenumber is swept through the specified range. As the wavenumber changes, it interacts with the molecular bonds changing the absorptivity. The amount of IR absorptivity of a molecular mode at a wavenumber is constant and unchanging. Therefore,

indicating the presence of that bond. This indicates the presence of that bond and can be a signature of this material. The amplitude of the absorptivity is proportional with the concentration.

In this study, attenuated total reflectance (ATR) was used. This configuration of ATR utilizes the same IR principles, but it lends itself very well to soft polymers due to its ease of operation and sample preparation. This technique uses a crystal where a standing wave (evanescent wave) is passed over the material surface. This wave penetrates the material (0.1 to 5 μm), and the beam spectrum is absorbed and collected [59].

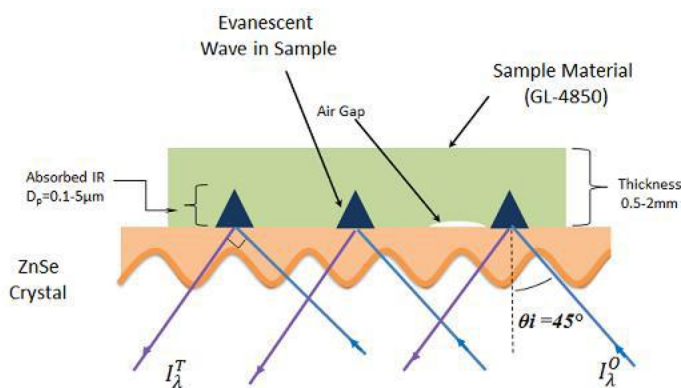


Figure 16: Schematic of ATR standing wave interaction with material. [75]

This method was used to identify the presence of isocyanate, hydroxyl, carbonyl, and esters groups. The peak at $2250\text{-}2270\text{ cm}^{-1}$ is attributed to the presence of free NCO and can be monitored to determine the degree of cure, verifying the conversion into urethane or urea linkages [40]. This peak is used for its very strong intensity.

Alternatively, the OH peak (3350 cm^{-1}) can be used, but this is less reliable [60]. Investigation of the FTIR spectrum morphology during cure and aging was conducted on multiple urethane samples produced from the reaction of poly(tetramethylene oxide) (PTMO-1000) with 1, 4-phenylene diisocyanate (PPDI), trans-1,4-cyclohexyl diisocyanate (CHDI), (4-isocyanatecyclohexyl)methane (HMDI), bis(4-isocyanatephenyl)methane (MDI) [61]. Yilgor et

al. have shown with a comparison of HMDI based polyurethane and a model urethane (BuO-HMDI-OBu) spectra indicating that FTIR can be used to measure the formation of strongly hydrogen bonded microstructures. Therefore, monitoring the spectra absorption peak at 1695 cm⁻¹ should correlate well with strongly hydrogen bonded urethane structures resulting in greater microphase separation. It is expected that with greater hydrogen bonding, a noticeable increase in the elastic modulus as well as other mechanical properties will be observed.

The reaction of water molecules from the moisture in the air or other contamination with free NCO will create urea linkage. Due to the strength of the bidentate hydrogen bonding or urea, it is expected to see a larger amplitude at 1635 cm⁻¹ with an increase in humidity. The following equation proposed by Yilgor et al. will be used to predict the amount of hydrogen bonded, ordered carbonyl groups [61]:

$$\%C = \frac{A(1695)}{A(1733) + A(1708) + A(1695)}, \quad (eq. 2.17)$$

where A(1695) is the absorbance at 1696 cm⁻¹ due to strongly H-bonded ordered carbonyl groups, A(1733) is the absorbance at 1733 cm⁻¹ due to free carbonyl groups, and A(1708) is the absorbance at 1708 cm⁻¹ due to disordered, hydrogen bonded carbonyl groups. The values for equation 2.17 can be obtained either from peak deconvolution or relative absorbance. Peak deconvolution will be used in this study. FTIR spectra peaks of interest are summarized in the table 7.

Vibration	Frequency	Intensity	Reference
v_{as} (NCO)	2300-2250 (L)	Very strong	[11]
v_s (NCO)	1450 - 1400 (L)	Very weak	[11]
δ_{perp} (NCO)	650 - 600 (L)	Poorly defined	[11]
$\delta_{parallel}$ (NCO)	600 - 590 (S)	Strong	[11]
Ester groups	1300 & 1060	Strong	[40]
Ester Carbonyl	1720-1730		[61]
Urethane	1695		[61]
Urea	1635		[61]

Table 7: Infrared frequency ranges for the characteristics vibrations in polyurethane elastomers.

2.3.4 Differential Scanning Calorimeter

Differential scanning calorimeter is a thermal analysis technique. A pan with a sample is heated simultaneously with a reference pan. The amount of heat required to raise the temperature of both pans at the same rate is measured. At sufficiently low temperatures, an endothermic peak signifies the onset of the glass transition and is related to the disordering of the crystallites [62].

Polyurethane is a copolymer consisting of both hard crystalline segments and an amorphous soft segment [62]. At room temperature, the soft segment is in the rubbery region ($T_g < T_{RT}$), whereas the hard segments remain crystalline and incompatible with the soft phase ($T_g > T_{RT}$). As the temperature is reduced, the soft segment will experience a glass transition. As the temperature is increased above room temperature, a series of endothermic peaks appear due to the disordering of the hard segments. Briber and Thomas have proposed type I and type II peaks distinguishing between a high degree of mixing phase and a more connected phase with higher phase separation [63]. In this study, DSC is used to find the glass transition temperature, as well as the change in specific heat to determine the degree of crystallinity of the polyurethane samples as shown in equation 2.1.

2.3.5 Scanning Electron Microscope

The scanning electron microscope (SEM), is a versatile tool used for material imaging. A focused electron beam is rastered across a material surface creating an interaction volume, which releases many types of electron and x-ray signals. The addition of different detectors allows it to pick up signals such as backscattered electrons (BSE), secondary electrons (SE), auger electrons, x-rays, and others. These signals are processed to give information about the topology, surface composition, and bulk composition. SEM has been used to study the superstructure development of spherulites of varying sizes in polyurethanes [64, 65]. The researchers in these studies have used monodispersed cast films. In this study, a batched polydispersed superstructure is expected. Moreover, increased branching between hard segments is expected due to the use of a thermoset instead of a thermoplastic. SEM images of type II hard segment crystals indicate a lath shape about 12 nm wide and 50-70 nm in length. Type I crystals are expected to be smaller than 10 nm and are difficult to detect [63]. AFM images also show hard segment domains about 70 nm long and 6 nm wide with varying length due to the degree of tilt to the viewing angle [64].

2.4 DOE Methodology

A design of experiments (DOE) is a “scientific approach which allows the researcher to gain knowledge in order to better understand a process and to determine how the inputs affect the response(s)” [66]. This methodology is used by the engineer and scientist to identify the key input factors, the interactions between these factors, and to build a regression fit (transfer function) and determine statistical significance. The types of DOEs available are: historical, screening (i.e. Taguchi L-12), full factorial, fractional, central-composite, Box-Behnken, and high throughput (HTT) (i.e. Latin hypercube). These designs, excluding historical DOEs, give fully orthogonal or near-orthogonal matrices. Orthogonality is important to ensure the balance of a design matrix and avoid aliasing. For each DOE, two parameters are important for the design chosen, the number of factors (K) and factor level. Furthermore, the number of repetitions (n_{reps}) for a desired statistical confidence (α) and power (β) must be determined. The outputs of the DOE are a \hat{Y} model

(transfer function for averages) and \hat{S} model (transfer function for standard deviation). The \hat{S} model describes the expected amount of variance as factor inputs change. In addition, statistical parameters such as p-values, r^2 and adjusted- r^2 , F statistics, T statistics, and variance inflation factor (VIF) are direct outputs of a regression analysis. An example of a general form transfer function output for a one factor 2-order polynomial fit is given by:

$$\hat{Y} = b_0 + b_1X_1 + b_{1,1}X_1^2 \quad (eq. 2.18)$$

Here, b_n is a constant value coefficient determined through the method, and X_n is the value of the n^{th} factor [66]. A (1,1) subscript indicates a second order coefficient for the 1st factor. However, this form may also include (X_1X_2) interaction terms with their own coefficients. The coefficients of the transfer functions are commonly plotted in a Pareto chart to show the impact of each factor, interaction, and higher order dependencies. The design of the DOE test matrix may or may not allow for the capturing of all interactions and higher order terms with significance due to aliasing between factors or low confidence. A further application of this approach is the ability to perform Monte Carlo simulation given tolerances for the process to find total variance and an estimated defects-per-million (DPM) or C_{pk} [67].

2.4.1 VOC and QFD Analysis

Voice of Customer (VOC) and Quality Function Deployment (QFD) are Six Sigma (DFSS) tools for capturing the needs of the “customer” and prioritizing them into the most relevant engineering parameters to optimize the return. The customer in this case may not necessarily be the end user, but they may be the next handoff in the design process. As a material scientist, the customer is the industrial formulator of the material. It is common in engineering to receive vague requirements at first request. These tools are part of the process to guide and document these vague requirements into concrete design parameters.

The QFD process is split into a series process. The first QFD₁ begins with the VOC and outputs the critical-to-customer (CTC) factors. These CTCs are then the inputs into QFD₂, which then outputs the critical-to-function (CTF). CTF's must be measurable factors. A Pareto chart of both the CTCs and CTFs are commonly created. These factors are rank order from the most important parameters to insure the success of a product. Further QFDs can be created for manufacturing and quality control metrics. However, this will be manufacturing process specific and must be completed at the industry level.

2.4.2 Ishikawa Diagram (CE)

Ishikawa diagrams, also known as cause-and-effect diagrams, are tools used to show common causes for a specific outcome. These tools can be used for gaining insight into the different types of factors which have influences on an “effect”. These effects may be for quality controls or product performance. The “causes” considered typically fall into six categories, measurements, materials, personnel, environment, methods, and machines. These categories are intended to capture the major areas which may lead to a quality defects or performance problems. For example, a suboptimal performance of a new material maybe due to an inherent error in the microstructural morphology as specified by the engineer, or it may be due to an incorrect setting of the machine, or may be due to a defect at the measurement device predicting suboptimal performance. This tool is used to allow for the investigation of all possible causes, and it is used to find and focus on root-causes.

2.4.3 IPO and SOP

Input-process-output (IPO) and standard operating procedures (SOP) are both integral parts of a DOE. The IPO is used to illustrate which factors the researchers believes have an influence on the outputs. These input factors are categorized as noise (N), control (C), or experimental (X). A noise is a factor which may affect the outputs, and it cannot be controlled (i.e. lab temperature and humidity). A control factor can and will be controlled to a constant value throughout the

experiment (i.e. mixing time, chemical suppliers, degassing). These must be specified in the SOP with a plan to reduce drift and variability. Experimental factors are the primary factors which will be tested against (i.e. mixing temperature, index, percent HS). The experimental values must also be specified in the SOP with a given range of intended parameter variation. The experimental factors are the key inputs to the transfer function created through the DOE process.

CHAPTER III

Section 3: EXPERIMENTAL PROCEDURES

3.1 DOE Design

3.1.1 QFD

By sitting down with a urethane pipeline pigging manufacturer, both QFD₁ and QFD₂ were completed to prioritize CTCs and CTFs. Results from QFD₁ are shown below for polyurethane criteria for pipeline pigging.

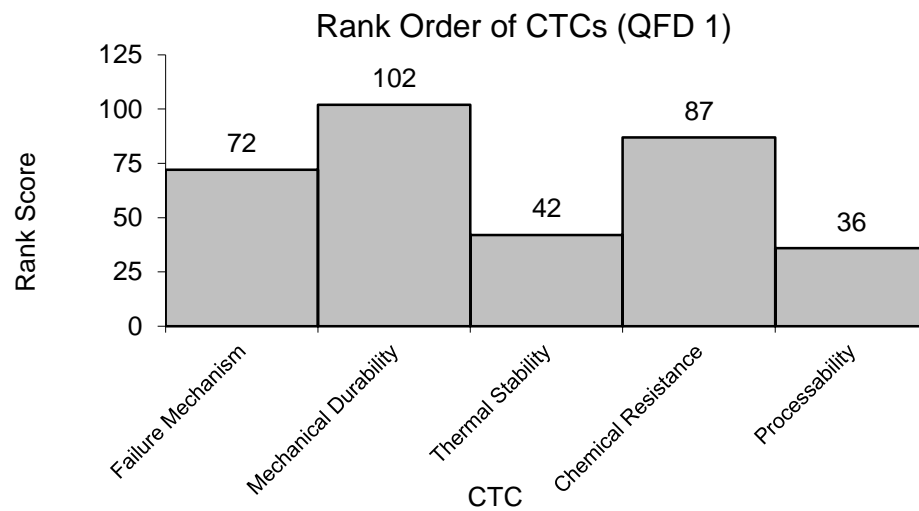


Figure 17: Result ranking of outputs from QFD 1.

As can be seen in the above figure, the mechanical durability of polyurethane ranks the highest for CTCs. With higher mechanical durability, the tools using polyurethane are able to last longer and return a higher value to the final user. The chemical resistance and failure mechanisms are the next highest ranked CTCs. All three of these factors describe the overall “customer’s” desire for the tool to “last longer”. To better define these CTCs in measurable terms, QFD₂ was completed. The CTFs from this are prioritized below:

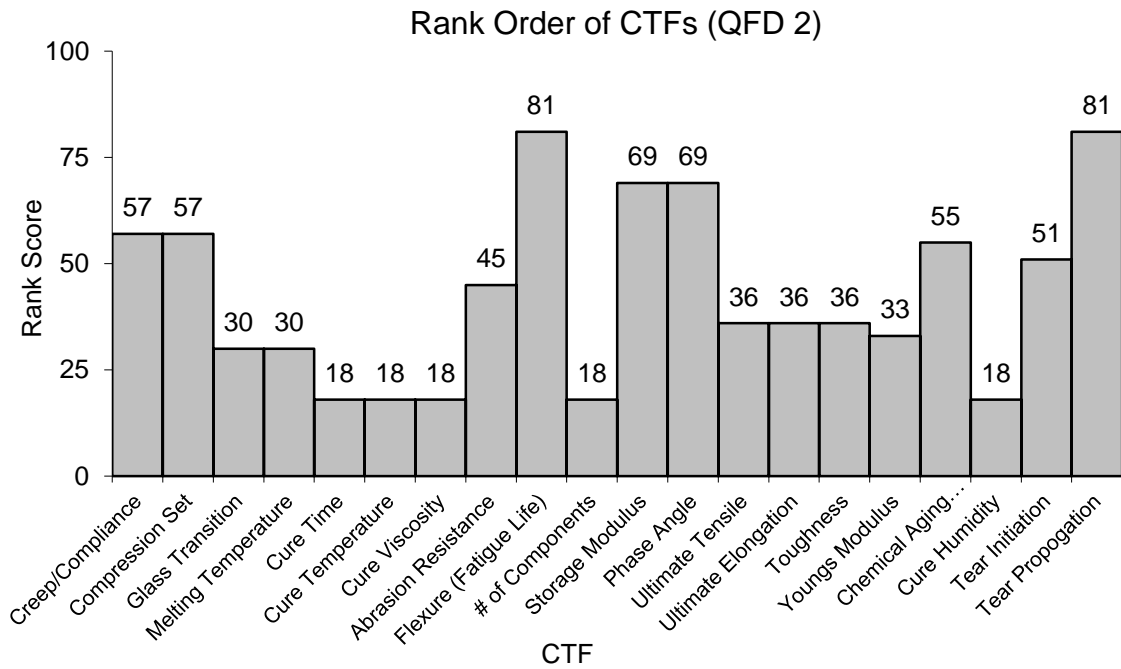


Figure 18: Rank of CTF from QFD 2.

From QFD₂, it can be seen that the fatigue life and tear propagation are the two highest ranked CTFs. However, as discussed in section 2, the fatigue life and abrasion resistance of polyurethane is closely related to tear propagation. The storage modulus and phase angle, or the viscoelastic behavior, is also highly ranked. These results are indicative of the importance of an overall understanding of the tear and viscoelastic behavior of polyurethane in pipeline pigging. Therefore, by optimizing these factors, the overall mechanical durability from QFD₁ can be optimized. This will maximize the performance of the material for its intended need. With a

better understanding of the microstructures (i.e. amount of hard segment and crosslinking) effects on these parameters is of utmost importance. Moreover, it is important to better understand how common manufacturing conditions, such as humidity, affect tear and viscoelasticity.

3.1.2 CE and IPO

An input-process-output (IPO) diagram was created to illustrate variables that were within the scope of this work and the output variables that have been characterized. For input variables; X denotes an experimental variable, C a controlled, and N is noise. As can be seen from figure 19 below, this study involves four experimental variables, percent hard segment, index, component temperature, and humidity. The range of these variables is presented in the DOE test matrix. DMA, SEM, DSC, FTIR, and tensile testing were conducted to characterize the viscoelastic behavior, morphology, microphase separation, and other mechanical properties of the polyurethane.

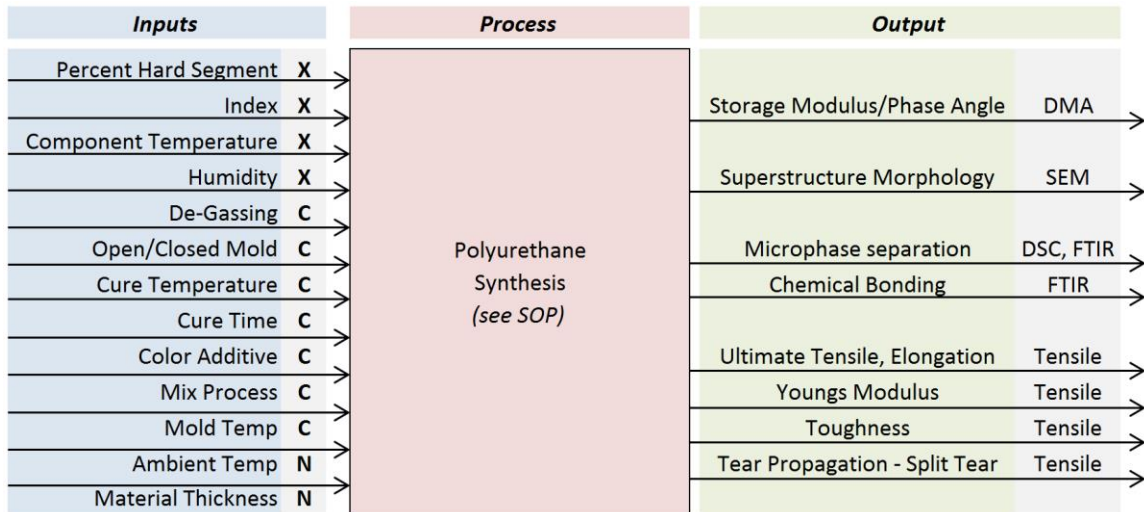


Figure 19: IPO diagram of intended experimental factors and the outputs and characterization methods.

3.1.3 DOE Test Matrix

The DOE test matrix selected is a 4 factor, 3-level, central composite, and 26 run DOE. The design points for %HS chosen were 0%, 20%, and 40%. The index design points chosen were

0.95, 1.00, and 1.05, mix temp from 81 °C, 93 °C, 105 °C, and humidity 20 %RH, 60 %RH, and 100 %RH. These ranges were selected based on estimates of common operating conditions and supplier recommended settings.

To improve statistical confidence in the experiment, 3 repetitions are needed for $\alpha = 0.95$ and $\beta = 0.99$. This gives a total of 78 samples. As part of the central composite design, the central point, run 17 and 18, are repeated. However, due to the large time commitment to process and characterize 78 samples, a smaller subset of this CCD DOE was completed as a screen for the effects of the factors. A full set of descriptions of the samples produced for this study can be found in table 10. Table 8 below is the full CCD matrix which is fully orthogonal.

Run #	% HS	Index	Mix Temp	Humidity	Replicates
1	0	0.95	81	20	3
2	0	0.95	81	100	3
3	0	0.95	105	20	3
4	0	0.95	105	100	3
5	0	1.05	81	20	3
6	0	1.05	81	100	3
7	0	1.05	105	20	3
8	0	1.05	105	100	3
9	40	0.95	81	20	3
10	40	0.95	81	100	3
11	40	0.95	105	20	3
12	40	0.95	105	100	3
13	40	1.05	81	20	3
14	40	1.05	81	100	3
15	40	1.05	105	20	3
16	40	1.05	105	100	3
17	20	1	93	60	3
18	20	1	93	60	3
19	0	1	93	60	3
20	40	1	93	60	3
21	20	0.95	93	60	3
22	20	1.05	93	60	3
23	20	1	81	60	3
24	20	1	105	60	3
25	20	1	93	20	3
26	20	1	93	100	3

Table 8: 4 factor, 3 level, CCD test matrix.

To control the %HS and index, the mixture ratio was adjusted as needed using equations 2.11 and 2.12. The chemical components were heated under vacuum with a thermocouple monitoring the temperature. The components were removed from the oven and measured out and placed back into the oven to maintain the correct temperature. Components were mixed and degassed if the pot-life allowed. Due to the high amount of BD in the 40 %HS samples, pot life was noticed to be drastically reduced. Once the samples were poured into the preheated molds, they were cured in the oven with the appropriate humidity control. For 100 %RH runs, a beaker with water was placed in the oven to fully saturate the curing atmosphere.

3.1.4 SOP

All samples were hand batched and mixed according to the hand bathing procedures outlined by the chemical supplier [68]. The steps are summarized here:

- 1) Preheat prepolymer and polyol. Monitor temperature with a type-k thermocouple.
- 2) Degass samples in a vacuum chamber (minimum 30 minutes).
- 3) Insure that prepolymer and polyol have reached the correct temperature.
- 4) Weigh out correct amount of BD to $\pm 0.05\text{g}$ in a 100ml plastic beaker.
- 5) Add correct amount of polyol measured to $\pm 0.1\text{g}$ to the BD.
- 6) Add correct amount of prepolymer measured to $\pm 0.5\text{g}$ to BD and polyol.
- 7) Mix prepolymer, polyol, and BD and insure that the walls are scraped for about 30-60 seconds. Use a glass stirring rod to reduce water contamination.
- 8) Degass mixture if pot life allows.
- 9) Pour mixture into the center of a mold preheated to $100\text{ }^{\circ}\text{C}$ and allowed to flow to the outside edge.
- 10) Appropriate humidity control was placed in the center of the oven rack.
 - a. 20%RH – Potassium Acetate
 - b. 60%RH – Sodium Bromide

c. 100%RH – Water

11) Allow to cure for 12 hours at 100 °C.

12) Demold, label, and store.

3.2 Sample Preparation

3.2.1 Materials

Polyurethane samples formulated in this study were bulk mixed from a 3 component polyester polyol, MDI, and 1,4 BD mixture. Chemical components were supplied by Chemtura. Vibrathane 7500 (MDI prepolymer), 7562 (polyester polyol), and 1,4 butane-diol were mixed in the appropriate ratios according to index and %HS calculations.

The Vibrathane 7500 prepolymer is part of quasi-prepolymer system with a free NCO content of 22%. To determine the actual weight of diisocyanate and polyol in this system for proper index and HS% calculations, the method outlined by Dow® was utilized [69].

$$Z = \frac{X + Y}{\left(\frac{42Y}{N}\right) - 1} \quad (eq. 3.1)$$

Where Z is the weight of isocyanate, X and Y are the polyol and isocyanate equivalent weight respectively, and N is the percentage of free isocyanate. The values for these can be found in the table 9 below as supplied by the supplier. A catalyst is also present in this system, but it is in small enough quantities that its weight effects are ignored.

Component	Molecular Weight (g/mol)	Functionality	Equivalent Weight (g/mol)
MDI	250	2	125
Polyol	1814	2	907
1,4 Butane-Diol	90	2	45

Table 9: Molecular weights and functionality of chemical components.

3.2.2 Apparatus and Equipment

3.2.2.1 Molds

Molds used in this study are galvanized steel blank square electrical conduit covers 4"x4" and ½" deep. These were supplied by McMaster-Carr and were found to be convenient and robust. MR™ 315 Urethane & Styrene Silicone Release Agent Aerosol was used as a mold release.

3.2.2.2 Degassing

Degassing of chemical components was conducted first during the melting down of the prepolymer and polyol. A vacuum pressure of 28 in-Hg was achieved. Furthermore, after mixing, components with a gel point which allowed were degassed for an additional 2 minutes in a vacuum chamber capable of reaching pressures of 30 in-Hg.

3.2.2.3 Oven

Two ovens were used in this study. The first is the vacuum oven used for both melting down the components and degassing. This was a Yamato ADP21 vacuum curing oven. Once mixed and poured, curing was conducted in a programmed Hamilton Beach convection oven with a Love Controls Series 4B temperature controller. Molds were cured on a wire meshing in the center of the oven. Temperature gradients were controlled, monitored, and logged using a series of K-type thermocouples and a Pax Instruments T400 thermometer DAQ.

3.2.2.4 *Mixing*

The mixture was mixed in a plastic, 100ml beaker with a glass rod for about 30-60 seconds. Care was taken to scrape the sides of the beaker.

3.2.2.5 *Humidity Control*

Humidity control was achieved by the use of anhydrous salts. Chemicals were supplied by Fisher Scientific. Humidity was monitored with a direct reading humidity and temperature meter with humidity accuracy of $\pm 2\%$ and a range of 25-95%. However, measurement of humidity at elevated oven temperatures was not possible due to meter limitations.

3.2.2.6 *Weight Scale*

Two types of weight scales were used in this study. The first scale was an analytical balance used to achieve the $\pm 0.05\text{g}$ tolerance for the BD. This was a Fisher Science ALF64. The second was a precision balance used for measuring of the prepolymer ($\pm 0.5\text{g}$) and diisocyanate ($\pm 0.1\text{g}$). This was a Mettler Toledo MS1602S/03.

3.2.2.7 *Chemical Storage*

To ensure that chemicals did not deteriorate while in storage, all containers were purged with dry nitrogen gas and sealed. The containers were also stored in a drum and purged with a constant stream of dry nitrogen gas. Chemicals were stored at room temperature.

3.3 Characterization Procedures

3.3.1 Tensile and Tear

Tensile and tear testing was done on an Instron Model 3345 with extensometers and calibrated by the National Voluntary Laboratory Accreditation Program (NVLAP). Tensile samples were stamped and tested according to ASTM D-614. Tear samples were stamped and tested according to ASTM D-470. Samples were stamped out using dies from Pioneer Dietecs with certificates of compliance. Two specimens from each sample were tested.

3.3.2 Fourier Transform Infrared Spectroscopy

FTIR spectrums were collected on a Varian 680-IR with an Agilent Technologies Cary 600 Series Microscope and Cary 610 ATR. A diamond ATR crystal cooled with liquid nitrogen was used. Spectrums were collected from wavenumber 400-4000 cm^{-1} at a resolution of 4 cm^{-1} . A background scan was collected using 16 scans, and 8 sample scans. Samples were cleaned with isopropyl alcohol and allowed to dry. Each sample was scanned in 4 separate locations to confirm spectrum consistency.

Origin 2016 software was used to analyze FTIR spectrums. Spectrums were first averaged across the 4 specimen scans. Next, a subset from 1600-1800 cm^{-1} was analyzed by first subtracting a baseline to isolate the carbonyl peaks. A peak deconvolution with a gauss fit was used to find peaks at 1685 cm^{-1} , 1708 cm^{-1} , and 1733 cm^{-1} .

3.3.3 Differential Scanning Calorimeter

In this study, a TA Instruments Q2000 DSC with a refrigerated cooling unit (RCS) was used. The samples were prepared and placed in Tzero aluminum pans without lids. A sample size between 5-15 mg was used to measure the T_g and ΔC_p . The furnace temperature was ramped from -90 °C to 150 °C at 3 °C/min. Indium was used to calibrate the DSC. All data was analyzed using TA Universal Analysis software.

3.3.4 Scanning Electron Microscopy

A Hitachi S-4800 FE-SEM was used for imaging of the microstructure of the samples. Specimens were first wiped clean with isopropyl alcohol and allowed to dry to remove any residual mold release. Samples were mounted onto a stage with double-sided carbon tape and grounded on the top and bottom of the sample. They were then gold sputter coated for 15 to 30 seconds. Samples were inserted into the microscope and imaged at an accelerating voltage of 1keV and an emission current of 10 μA . A secondary electron signal was collected from a mix of

detectors, one above and one below the sample. A backscattered electron signal was also collected and is presented in the appendix.

CHAPTER IV

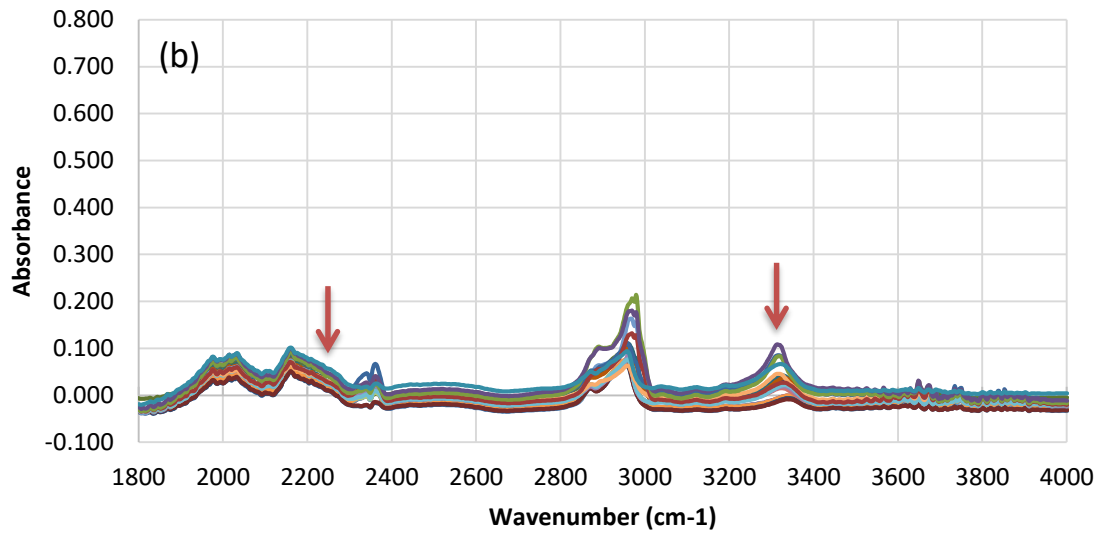
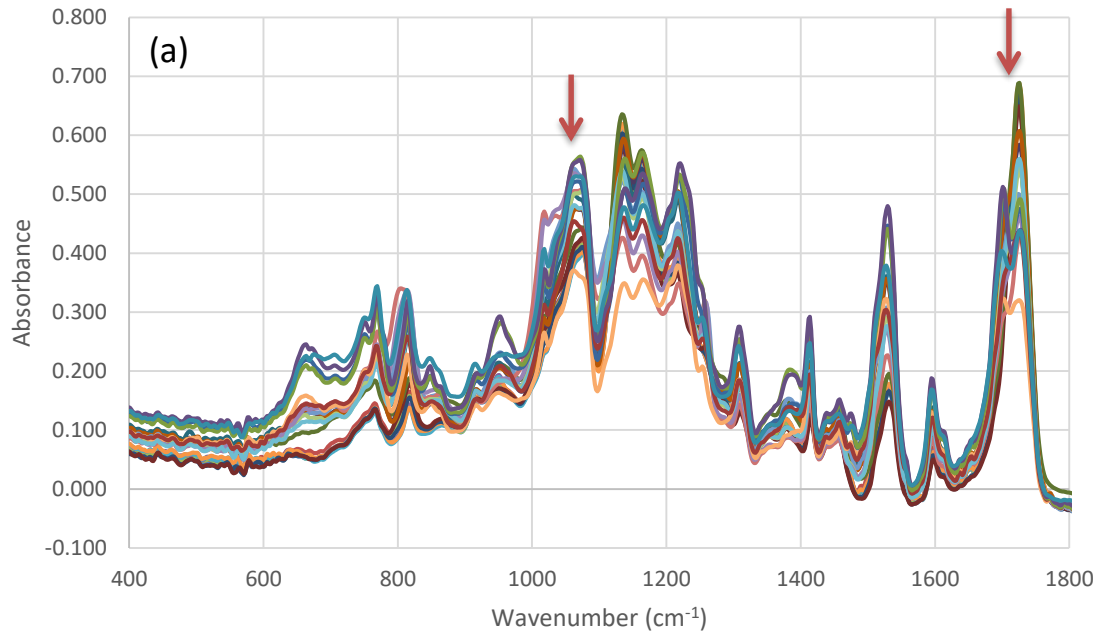
Section 4: RESULTS AND ANALYSIS

4.1 FTIR Characterization

23 samples were prepared and characterized using FTIR. Six samples with the same chemistry were also characterized. These were received from two different manufacturers. The results for these samples are included in Appendix A. The 23 DOE test runs completed are summarized in table 10. In order to reduce bias or noise aliasing, DOE run numbers have been quasi-randomized. To reduce processing time, samples with similar humidity and component temperature were synthesized sequentially. Figure 20 has been split into two graphs, graph (a) is the absorbance spectrum from 400 – 1800 cm^{-1} , graph (b) is the absorbance spectrum from 1800 – 4000 cm^{-1} . No absorbance peak is seen at 2250-2270 cm^{-1} indicating the reaction of all free isocyanate in all the samples. A peak in some of the samples around 3315-3343 cm^{-1} indicates stretching of the N-H bond in urethane and urea molecules. As this peak increases in intensity, a shift to a lower wavenumber occurs. Ester peaks are apparent around 1060 cm^{-1} . Strong carbonyl peaks are also evident around 1650-1750 cm^{-1} . These carbonyl peaks are further investigated by peak deconvolution.

Sample Number	Run	HS	Index	Temp	RH
SN 0028	19	0	1	93	49
SN 0030	20	40	1	93	49
SN 0031	2	0	0.95	81	100
SN 0032	6	0	1.05	81	100
SN 0033	17	20	1	93	46
SN 0034	18	20	1	93	46
SN 0035	21	20	0.95	93	46
SN 0036	22	20	1.05	93	46
SN 0037	19	0	1	93	46
SN 0038	4	0	0.95	100	100
SN 0039	8	0	1.05	97.3	100
SN 0041	12	40	0.95	95.4	100
SN 0042	14	40	1.05	94.5	100
SN 0043	17	20	1	93	46
SN 0044	20	40	1	89	46
SN 0045	21	20	0.95	89	46
SN 0046	22	20	1.05	88	46
SN 0047	26	20	1	93	100
SN 0048	10	40	0.95	81	100
SN 0049	16	40	1.05	105	100
SN 0050	2	0	0.95	81	100
SN 0051	6	0	1.05	81	100
SN 0053	4	0	0.95	105	100

Table 10: Composition and processing parameters of sample numbers. The run number correlates to the run number of the DOE design matrix in Chapter 3.



- SN 0053 - AVG — SN 0051 - AVG — SN 0050 - AVG — SN 0039 - AVG
- SN 0038 - AVG — SN 0037 - AVG — SN 0032 - AVG — SN 0031 - AVG
- SN 0028 - AVG — SN 0047 - AVG — SN 0046 - AVG — SN 0045 - AVG
- SN 0043 - AVG — SN 0036 - AVG — SN 0035 - AVG — SN 0034 - AVG
- SN 0033 - AVG — SN 0049 - AVG — SN 0048 - AVG — SN 0044 - AVG
- SN 0042 - AVG — SN 0041 - AVG — SN 0030 - AVG

Figure 20: FTIR Spectrum of DOE test specimens. (a) spectrum from 400 to 1800 cm⁻¹ (b) spectrum from 1800 to 4000 cm⁻¹

The carbonyl regions of the FTIR spectrum for 0%, 20% and 40% hard segments are shown below in figure 21, 22, and 23 respectively. Very consistent spectra for the 0% HS (figure 21), full soft segment polymers are observed. A strong distinct peak occurs centered at 1730 cm^{-1} for all samples indicating full transformation into disordered, non-hydrogen bonded carbonyl groups. A small shoulder at about 1710 cm^{-1} and 1685-1687 cm^{-1} indicates some hydrogen bonding, but a low number of ordered crystalline urethane structures is shown. No peak is observed at 1635 cm^{-1} that is distinct beyond any noise indicating the formation of urea groups from reaction with water molecules from atmospheric humidity. Moreover, good separation in the spectra between 600 and 800 cm^{-1} is observed. However, this has not been further investigated.

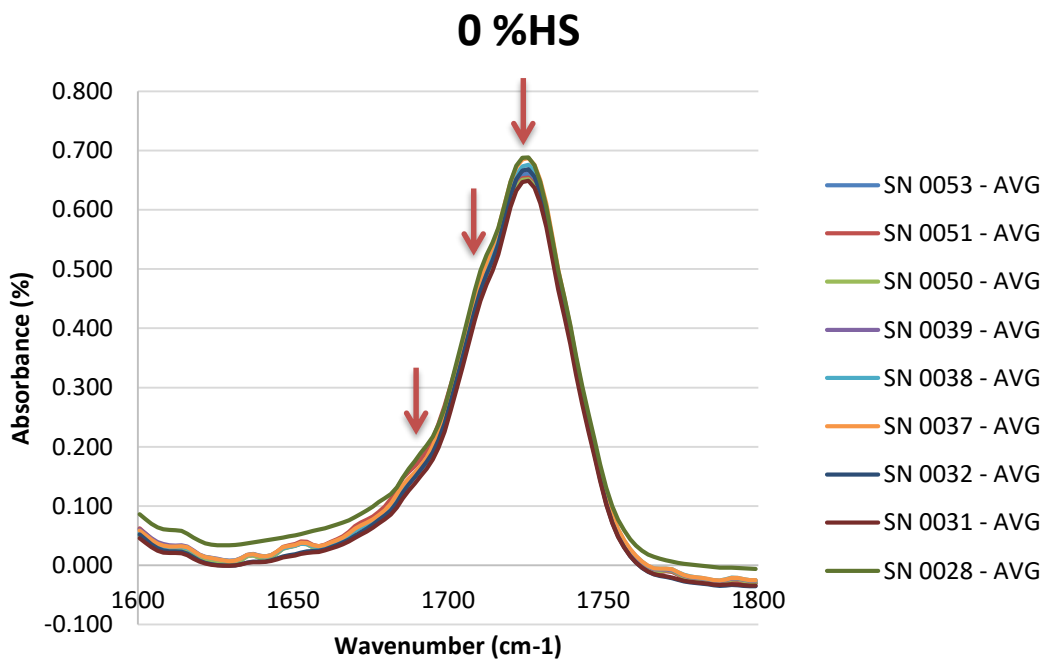


Figure 21: Carbonyl region of FTIR spectra for 0% hard segment polyurethane with varying temperature, index, and humidity.

As the percentage of hard segment is increased, the shoulder appearing to center at 1706 cm^{-1} becomes larger. This shoulder appears to have shifted to a slightly lower wavenumber from the 1708 cm^{-1} peak in the 0 %HS samples to 1702 cm^{-1} in the 20 %HS samples. Small shoulder at 1685 cm^{-1} also appears to have not grown. The large peak amplitude at 1725 cm^{-1} has become

smaller. As compared with the 0 %HS case, there is a larger spread of spectras between samples. Moreover, a very small peak is observed at 1635 cm^{-1} . However, this peak amplitude remains small for all samples.

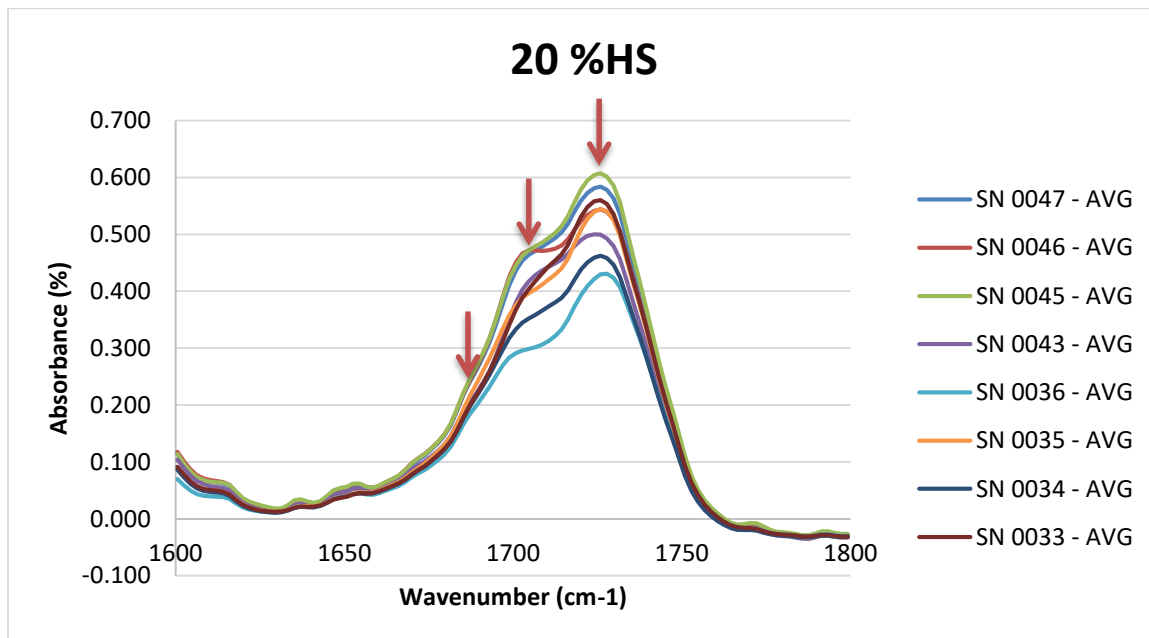


Figure 22: Carbonyl region of FTIR spectra for 20% hard segment polyurethane with varying temperature, index, and humidity.

For the 40 %HS samples, similar to the 20 %HS condition, the peak amplitude at 1725 cm^{-1} continues to shrink as the peak amplitude at 1709 cm^{-1} increases. The 1709 cm^{-1} shoulder observed in figure 21 continues to shift to a lower wavenumber of 1701 cm^{-1} for the 40 %HS case. The shoulder at 1685 cm^{-1} remains small. The absorbance peak at 1635 cm^{-1} also remains too small to distinctively identify. The 40 %HS maintains distinct variation between sample spectras similar to the 20 %HS spectras.

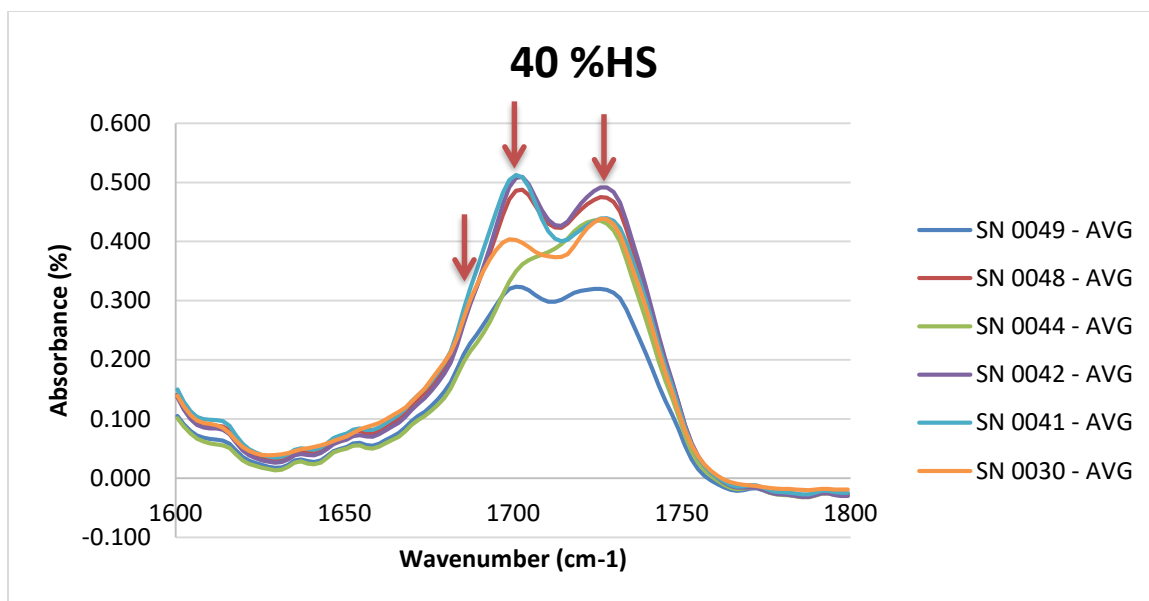


Figure 23: Carbonyl region of FTIR spectra for 40% hard segment polyurethane with varying temperature, index, and humidity.

Moreover, an FTIR spectra of a 72% hard segment sample is presented in figure 24 below. This sample is not included in the DOE regression. However, it adds insight into the influence of hard segment on the carbonyl hydrogen bonding. It can be seen that at this extreme case, the peak at 1733 cm^{-1} has almost disappeared and been converted into the 1708 cm^{-1} peak, which has shifted to 1701 cm^{-1} . The 1685 cm^{-1} peak remains unchanged indicating a microstructure dominated by H-bonded amorphous hard segment.

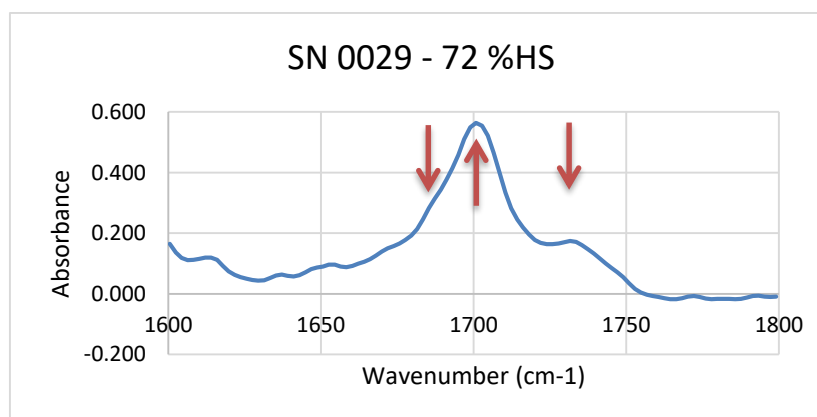


Figure 24: Carbonyl region of FTIR spectra for 72% hard segment polyurethane. This sample was not included in the DOE regression.

Peak deconvolution of the carbonyl peaks discussed above is presented in the Appendix C.

Results from deconvolution are presented in table 11.

Sample Number	HS	Peak Center (cm ⁻¹)			Peak Amplitude (%)		
		peak 1	peak 2	peak 3	peak 1	peak 2	peak 3
SN 0028	0	1693.8	1706.8	1725.3	0.11	0.07	0.64
SN 0031	0	1693.8	1706.3	1725.6	0.11	0.05	0.64
SN 0032	0	1693.6	1706.2	1725.5	0.12	0.06	0.66
SN 0037	0	1693.7	1705.9	1725.5	0.12	0.06	0.67
SN 0038	0	1694.3	1706.1	1725.7	0.12	0.06	0.65
SN 0039	0	1694.9	1706.3	1725.8	0.12	0.06	0.64
SN 0050	0	1695.0	1705.8	1725.8	0.12	0.06	0.63
SN 0051	0	1694.2	1705.5	1725.7	0.13	0.06	0.63
SN 0053	0	1694.5	1705.8	1725.7	0.12	0.06	0.64
SN 0033	20	1685.0	1702.4	1726.7	0.09	0.24	0.54
SN 0034	20	1684.1	1701.8	1727.4	0.08	0.23	0.44
SN 0035	20	1685.0	1700.5	1727.1	0.09	0.23	0.53
SN 0036	20	1685.0	1699.6	1728.3	0.08	0.18	0.42
SN 0043	20	1685.0	1704.1	1727.6	0.10	0.28	0.47
SN 0045	20	1685.0	1701.9	1726.7	0.11	0.29	0.58
SN 0046	20	1685.9	1702.5	1727.2	0.11	0.31	0.52
SN 0047	20	1695.5	1702.2	1727.9	0.15	0.22	0.52
SN 0030	40	1685.1	1699.6	1728.3	0.09	0.28	0.40
SN 0041	40	1685.0	1700.7	1728.5	0.11	0.38	0.42
SN 0042	40	1685.0	1701.1	1727.8	0.12	0.37	0.47
SN 0044	40	1685.0	1703.5	1728.2	0.08	0.25	0.40
SN 0048	40	1685.0	1701.3	1727.9	0.12	0.35	0.45
SN 0049	40	1685.0	1701.4	1729.2	0.07	0.24	0.29

Table 11: Peak deconvolution of carbonyl region FTIR spectrum. Rows are organized by percent hard segment. Peak 1, peak 2, and peak 3 are gauss fit functions over the 1685, 1708, and 1733 cm-1 peaks and shoulders respectively.

A DOE regression analysis was completed for the peak amplitudes in Table 11. All second order interaction and quadratic terms were kept for the initial regression. Since a reduced CCD DOE was used, a historical DOE analysis was conducted. Therefore, perfect orthogonality is not expected. Due to this low confidence and/or orthogonality, many high order terms were dropped. S-hat models could not be generated due to insufficient repetitions. Reduced coded regression tables are presented in table 12 below. In table 12, SE is the standard error, T is the signal-to-noise T-stat (Coeff/SE), P is the confidence level P-value, and VIF is the variance

inflation factor, a measure of factor orthogonality. A high T-stat indicates a high signal-to-noise ratio, and low P-value (<0.05) indicates a statistically significant term. Moreover, a low VIF is also necessary to signify a balanced sample set. Values of VIF 2 and greater indicate factor aliasing with another term, and this may give misleading results. If two factors are always changed simultaneously, and a response is observed, it is statistically impossible to contribute this response to either factor because of aliasing. Significant P-value terms are represented in red. Factors that may be statistically significant (P-value between 0.05 and 0.1) are in blue.

	Factor	Coeff	SE	T	P	VIF		R ²
1685 cm ⁻¹	Const	0.1359	0.0043	31.853	0.000			0.792
	HS (A)	-0.0117	0.0028	-4.1913	0.001	1.0944		Adj R ² 0.714
	Index (B)	0.0015	0.0026	0.5576	0.585	1.0121		Std Error 0.0102
	Temp (C)	-0.0071	0.0041	-1.7583	0.098	1.21		F 10.152
	RH (D)	0.0167	0.0032	5.2908	0.000	2.1621		Sig F 0.0001
	AA							F _{LOF} 1.6005
	BB	-0.0106	0.0056	-1.8735	0.079	1.6066		Sig F _{LOF} 0.3462
	CC	-0.0089	0.0075	-1.1876	0.252	2.4348		
1708 cm ⁻¹	Factor	Coeff	SE	T	P	VIF		R ² 0.9766
	Const	0.2834	0.0137	20.673	0.000			Adj R ² 0.9678
	HS (A)	0.1529	0.0065	23.65	0.000	1.0546		Std Error 0.0241
	Index (B)	0.0013	0.0062	0.2047	0.840	1.0069		F 111.054
	Temp (C)	0.0051	0.0089	0.5768	0.572	1.0378		Sig F 0.0
	RH (D)	-0.0032	0.0076	-0.4271	0.675	2.2416		F _{LOF} 1.2702
	AA	-0.0631	0.0133	-4.7563	0.000	1.5865		Sig F _{LOF} 0.4448
	BB	0.0127	0.0131	0.9732	0.345	1.5439		
CC								
1733 cm ⁻¹	Factor	Coeff	SE	T	P	VIF		R ² 0.9753
	Const	0.5822	0.0089	65.733	0.000			Adj R ² 0.968
	HS (A)	-0.1419	0.0059	-24.252	0.000	1.0539		Std Error 0.0218
	Index (B)	-0.003	0.0057	-0.5273	0.605	1.0068		F 134.301
	Temp (C)	0.0002	0.008	0.026	0.980	1.028		Sig F 0.0
	RH (D)	-0.0114	0.0057	-1.9857	0.063	1.5612		F _{LOF} 0.5818
	AA	0.0628	0.0119	5.2951	0.000	1.5439		Sig F _{LOF} 0.7943
	BB							
CC								

Table 12: Coded regression table for peak deconvolution of FTIR spectrum of carbonyl formations centered at 1685, 1708, and 1733 cm⁻¹.

From table 12, relative humidity P-values indicate a significant term, however, high aliasing (VIF=2.1621) does not allow for a confident correlation. Hard segment content shows good orthogonality (1.0944), signal-to-noise (-4.1913), and confidence (0.001) for all peaks. This indicates the amount of hard segments large contribution to ordered carbonyl H-bonding.

However, a negative coefficient for the %HS of the 1685 cm⁻¹ implies that increasing hard segment reduces the percentage of well ordered, H-bonded carbonyl groups. This coefficient (-0.0117) is relatively small compared to the constant (0.1359) implying that even though %HS reduces the 1685 cm⁻¹ peak, this amount is very small. In comparison, the %HS contribution to the 1708 cm⁻¹ peak is 0.1529; this is more than half its constant value (0.2834) indicating its large contribution. Moreover, the %HSs quadratic term, AA, also shows low P-values and near acceptable orthogonality. The negative coefficient for this (-0.0631) indicates that as HS is increased, the 1708 cm⁻¹ peak will increase only to a maximum value. No other factor shows adequate statistical confidence or orthogonality. Further testing of %RH and temperature is recommended in order to improve orthogonality and statistical power. The mix index shows high P-values even with excellent orthogonality, indicating no significance.

The R² and adjusted-R² of the models for 1708 and 1733 cm⁻¹ show good correlation, 0.9678 and 0.968 respectively. The uncoded regression equations are:

$$A(1695) = -4.6354 - 0.0006A + 8.4856B + 0.0109C + 0.0006D - 4.228B^2 - 0.0001C^2 \quad (eq. 4.1)$$

$$A(1708) = 5.1075 + 0.014A - 10.168B + 0.0004C - 0.0001D - 0.0002A^2 + 5.0968B^2 \quad (eq. 4.2)$$

$$A(1733) = 0.8756 - 0.0134A - 0.0596B - 0.0004D + 0.0002A^2 \quad (eq. 4.3)$$

Where A(X) is the amplitude at X wavenumber in cm⁻¹, A is weight percent of hard segment between 0 and 40%, B is the index between 0.95 and 1.05, C is the temperature between 81 and 105 °C, and D is the relative humidity between 46 and 100%. Constant value standard deviation for these models are 0.0087, 0.0138, and 0.0215 for the 1685, 1708, and 1733 cm⁻¹ peaks. These show good correlation between calculated and tested values for the 1708 and 1733 cm⁻¹ peaks.

Residual plots of the regression models created above are shown below in figure 25. Care must be taken with these models, so that the same units are used and within the ranges tested.

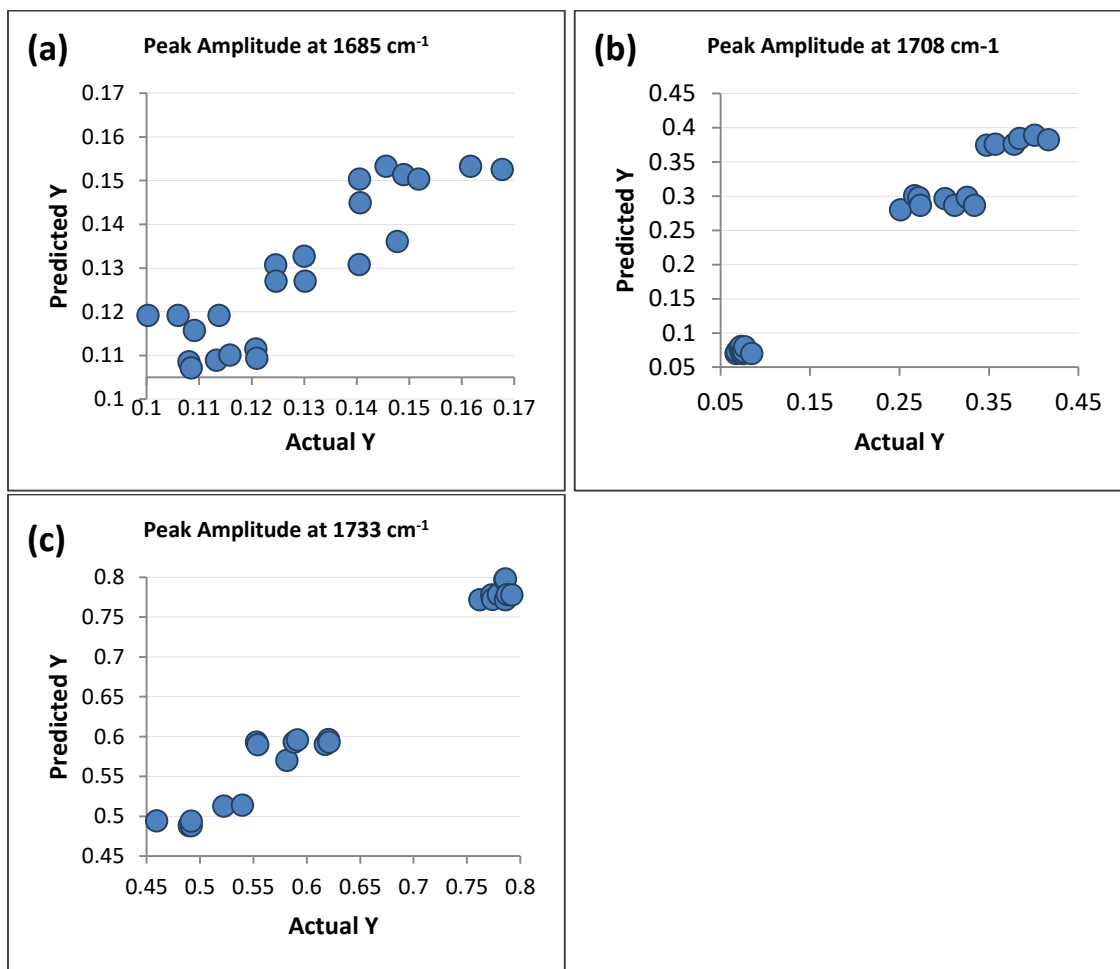


Figure 25: residual plots of generated regression models. Actual test results are compared with model predictions. Graph (a) 1685 cm⁻¹ peak, (b) 1708 cm⁻¹ peak, (c) 1733 cm⁻¹ peak.

As can be seen from this data, the regression model shows good confidence in prediction of the 1733 cm⁻¹ and 1708 cm⁻¹ peaks. However, due to the little variation in the 1685 cm⁻¹ peak, the model shows a larger spread as can be seen in figure 25(a). The percentage of hard segment shows the greatest contribution to the increase in the 1708 cm⁻¹ peak, indicating an increased disordered H-bonded polymer network. The temperature, humidity, and index show very little

influence on these three peaks. The effects of relative humidity did not cause any detectable peaks at 1635 cm⁻¹.

4.2 DSC Characterization

Differential scanning calorimetry data was collected for the same set of samples characterized in FTIR. A list of the samples and their processing has been described in table 10. The T_g and the change in specific heat (ΔC_p) at the glass transition was calculated using TA Instruments Universal software. The change in the crystalline structure at the glass transition temperature is due to a phase change of the soft segment. Therefore, equation 2.1 may be used to predict the percentage of microphase separated, crystalline material. The results from this analysis for the DOE samples are summarized in table 13 below.

Sample Number	Run	T _g	ΔC_p
SN 0028	19	-35.51	0.3541
SN 0030	20	-33.35	0.2541
SN 0031	2	-34.77	0.3063
SN 0032	6	-35.39	0.4128
SN 0033	17	-26	0.2998
SN 0034	18	-29.53	0.3194
SN 0035	21	-32.94	0.3024
SN 0036	22	-23.38	0.4027
SN 0037	19	-35.12	0.3605
SN 0038	4	-34.04	0.3284
SN 0039	8	-35.43	0.3223
SN 0041	12	-19.54	0.2677
SN 0042	14	-17.9	0.315
SN 0043	17	-23.36	0.4357
SN 0044	20	-32.07	0.1848
SN 0045	21	-33.3	0.3074
SN 0046	22	-32.47	0.3941
SN 0047	26	-27.45	0.3584
SN 0048	10	-17.24	0.3836
SN 0049	16	-24.38	0.1862
SN 0050	2	-36.26	0.3433
SN 0051	6	-34.08	0.4271
SN 0053	4	-37.62	0.4166

Table 13: Glass transition temperature and change in the specific heat results.

Regression statistics results are shown in Table 14. From these results, it can be seen that the hard segment has a large influence on both T_g and ΔC_p as indicated by the large coefficient values. For both of these cases, the orthogonality and confidence are acceptable. The hard segment quadratic also shows high levels of confidence with a negative coefficient for the prediction of the change in specific heat. The processing temperature indicates a significant effect on the specific heat, however, orthogonality is lacking for the glass transition temperature model. More test runs are needed to confirm this result. Multiple second order factors, AC, AD, and BC all show low p-values. However, more samples are needed to confirm their coefficients. An adjusted- R^2 value of only 0.6162 for ΔC_p is low. An important note is the significance and good orthogonality of the relative humidity quadratic (DD) on the glass transition temperature. However, the value of T-stat, a measure of signal-to-noise ratio, is relatively low. This represents the high amount of noise in the testing results. The large coefficient for this term implies significant second order interaction between %RH and T_g .

Factor	Coeff	SE	T	P	VIF	R ²	0.8846
Const	-58.839	10.065	-5.8462	0.000		Adj R ²	0.8186
HS (A)	5.2717	0.8407	6.2706	0.000	1.4396	Std Error	2.6781
Index (B)	1.3446	0.7855	1.7118	0.109	1.2868	F	13.414
Temp (C)	7.079	2.8135	2.516	0.025	8.361	Sig F	0.0
RH (D)	0.1132	0.6883	0.1645	0.872	1.4875	F _{LOF}	1.5004
AC						Sig F _{LOF}	0.3704
AD	2.7854	0.8543	3.2604	0.006	1.4439		
BC							
BD	-1.5756	0.7855	-2.0058	0.065	1.2867		
CD	-8.411	2.8122	-2.9909	0.010	8.713		
AA							
CC							
DD	31.02	10.323	3.0049	0.009	1.1952		

Factor	Coeff	SE	T	P	VIF	R ²	0.7732
Const	0.3644	0.0173	21.018	0.000		Adj R ²	0.6162
HS (A)	-0.0501	0.0134	-3.7446	0.002	1.4418	Std Error	0.0426
Index (B)	0.0224	0.0135	1.6609	0.121	1.5023	F	4.9243
Temp (C)	-0.0543	0.018	-3.019	0.010	1.3517	Sig F	0.005
RH (D)	0.0232	0.0115	2.0198	0.065	1.6377	F _{LOF}	0.4599
AC	-0.0411	0.0203	-2.0223	0.064	1.6947	Sig F _{LOF}	0.8468
AD	0.0291	0.0136	2.1407	0.052	1.4493		
BC	-0.0387	0.0183	-2.1205	0.054	1.4329		
BD	-0.0159	0.0129	-1.235	0.239	1.3763		
CD							
AA	-0.0552	0.0232	-2.3809	0.033	1.5468		
CC							
DD							

Table 14: Coded regression coefficients and statistics for the glass transition temperature and specific heat. Higher order, low confidence terms have been dropped to improve regression fit.

The uncoded regression equations generated for DSC results are:

$$T_g = -173.3 - 0.113A + 112B + 2.485C - 2.73 + 0.0052AD - 1.1671BD - 0.026CD + 0.0426DD \quad (eq. 4.4)$$

$$\Delta C_p = -5.7103 + 0.0175A + 6.16B + 0.0618C - 0.0002D - 0.0002AC + 0.0001AD - 0.0626BC - 0.0001AA \quad (eq. 4.5)$$

Where A is the weight percent of hard segment between 0 and 40%, B is the index between 0.95 and 1.05, C is the temperature between 81 and 105 °C, and D is the relative humidity between 46 and 100%. Residual plots of the model are shown below in figure 26.

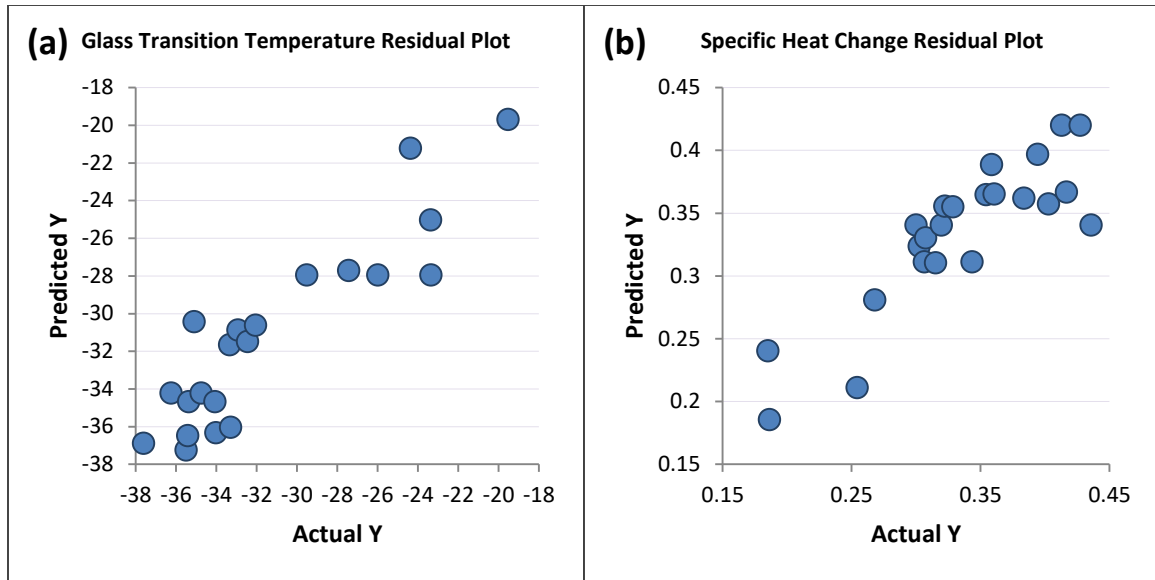


Figure 26: Residual plot of Tg (a) and ΔC_p (b). Actual test results are contrasted with regression model predictions.

By the combination of equation 2.1 and 4.5, an equation for the phase segregation can be created.

$$\alpha_{seg} = \frac{\Delta C_{P,Block}}{\Delta C_{P,SS}} = \frac{\Delta C_P(A, B, C, D)}{\Delta C_P(A = 0, B, C, D)} \quad (eq. 4.6)$$

Therefore, it can be seen from these results that the quadratic of the humidity term could have the largest effect on the glass transition temperature. However, the low signal-to-noise requires higher resolution testing or more sample repetitions. The %HS shows both good correlation and confidence. Mixing temperature and CD requires more sampling to improve orthogonality. The specific heat regression model does not show great R^2 values with a tendency to under predict test results.

4.3 Tensile Testing

Tensile testing was completed on the DOE samples in table 10. Two tension and two tear specimens from each sample were stamped out and tested. Results from these two specimens were averaged. These results are presented in table 15 below. Note, that maximum tensile results

are considerably lower than expected. This may be due to a high amount of porosity introduced during sample processing.

Sample Number	Run	Elongation at Break (%)	Max Tensile (psi)	Tear Strength (lb/in)
28	19	979	1171	54.63
30	20	38	1319	111.78
31	2	1003	419	34.43
32	6	883	1168	50.66
33	17	442	1250	82.73
34	18	559	1640	99.29
35	21	833	1309	94.22
36	22	113	277	34.04
37	19	850	1456	50.63
38	4	999	575	43.91
39	8	927	1630	49.23
41	12	22	1304	83.18
42	14	122	1240	65.70
43	17	240	805	54.20
45	21	682	740	74.06
46	22	114	301	35.53
47	26	426	1177	75.86
48	10	113	1187	42.40
49	16	197	2853	132.20
50	2	969	1230	53.64
51	6	705	1162	49.83
53	4	976	599	38.18

Table 15: Testing results for elongation at break, tensile strength at break, and tear strength.

The regression statistical results are shown below in table 16. The percentage of hard segment and index show low p-values and adequate orthogonality. Negative coefficients indicate that as these factors increase, the maximum elongation will decrease (i.e. get stiffer). Moreover, the interaction between index and relative humidity is significant and is positively correlated. Therefore, as humidity and index increase or decrease together, an increase in max elongation is expected. This regression model (elongation) shows good correlation with test results having an adjusted-R² value of 0.9464.

The tensile regression model shows a high amount of aliasing. Significant factors are processing temperature, and AB, BC, BB, and BD interactions. This regression model shows low adjusted-R² (0.6705) and is therefore not recommended without additional testing.

The tear regression analysis shows multiple significant terms. HS, index, temperature and AC, BD, and BB interactions all show sufficiently low P-values. However, high VIF for A, AC, and BD indicate the need for better orthogonality for these terms. The adjusted-R² of this model is 0.7912.

Factor	Coeff	SE	T	P	VIF
Const	473.522	19.397	24.412	0.000	
HS (A)	-433.782	27.575	-15.731	0.000	1.3383
Index (B)	-161.99	26.207	-6.1811	0.000	1.362
Temp (C)	43.329	38.093	1.1375	0.274	1.4487
RH (D)	29.497	18.983	1.5539	0.143	1.0205
AB	34.003	32.427	1.0486	0.312	1.5275
AC					
AD					
BC	54.328	37.852	1.4353	0.173	1.4805
BD	148.75	25.9	5.7433	0.000	1.3303
BB					
CC					

R ²	0.9643
Adj R ²	0.9464
Std Error	86.839
F	53.993
Sig F	0.0
F _{LOF}	0.2162
Sig F _{LOF}	0.9774

Factor	Coeff	SE	T	P	VIF
Const	1,321.77	139.691	9.4621	0.000	
HS (A)	114.205	103.559	1.1028	0.294	1.3963
Index (B)	-30.878	103.062	-0.2996	0.770	1.5582
Temp (C)	630.623	177.513	3.5525	0.005	2.3272
RH (D)	67.017	101.013	0.6634	0.521	2.1376
AB	-306.966	132.725	-2.3128	0.041	1.893
AC	304.062	169.509	1.7938	0.100	2.0481
AD					
BC	378.197	139.979	2.7018	0.021	1.4977
BD	260.828	102.128	2.5539	0.027	1.5301
BB	-455.256	183.772	-2.4773	0.031	1.5812
CC	514.054	249.487	2.0604	0.064	2.6895

R ²	0.8274
Adj R ²	0.6705
Std Error	319.28
F	5.2742
Sig F	0.0056
F _{LOF}	0.3735
Sig F _{LOF}	0.879

Factor	Coeff	SE	T	P	VIF
Const	78.942	5.2445	15.052	0.000	
HS (A)	22.737	4.2333	5.371	0.000	1.5694
Index (B)	-11.587	3.7182	-3.1162	0.008	1.3641
Temp (C)	20.159	5.2355	3.8504	0.002	1.3616
RH (D)	-1.2394	3.2557	-0.3807	0.710	1.4936
AB					
AC	22.503	5.7475	3.9152	0.002	1.5837
AD	-6.6592	4.3276	-1.5388	0.148	1.6556
BC					
BD	12.673	3.7333	3.3945	0.005	1.3752
BB	-16.567	6.8223	-2.4283	0.030	1.4657
CC					

R ²	0.8707
Adj R ²	0.7912
Std Error	12.311
F	10.946
Sig F	0.0001
F _{LOF}	0.2702
Sig F _{LOF}	0.9523

Table 16: Coded regression coefficients and statistics for tensile testing data.

The main effects plots for elongation and tear are shown in figure 27. The plots for tensile have been excluded due to the high aliasing and low regression fit. For each plot, all other factors are held constant at their median value. It can be seen that increasing hardness content and processing temperature has a large effect on tear strength. The VIF for the AC interaction is 1.5837, indicating that some aliasing is occurring. More DOE design points could reduce this. The relative humidity has a very minor impact on both elongation and tear strength. As percent hard segment is increased, the max elongation is reduced. Figure 28 presents the residual plots for these two models.

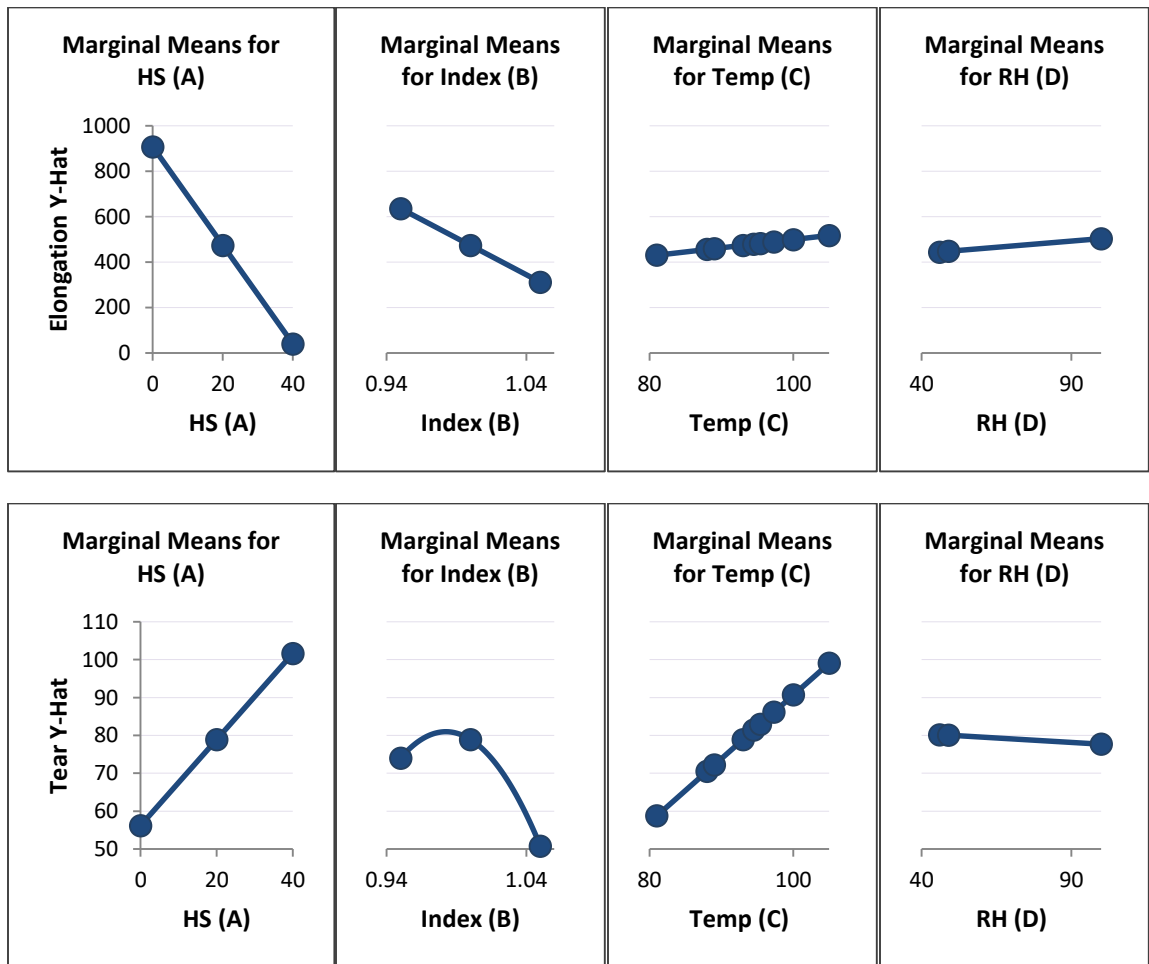


Figure 27: Main effects plots for predicted elongation and tear strength. At each factor, all other factors are held constant at their median values.

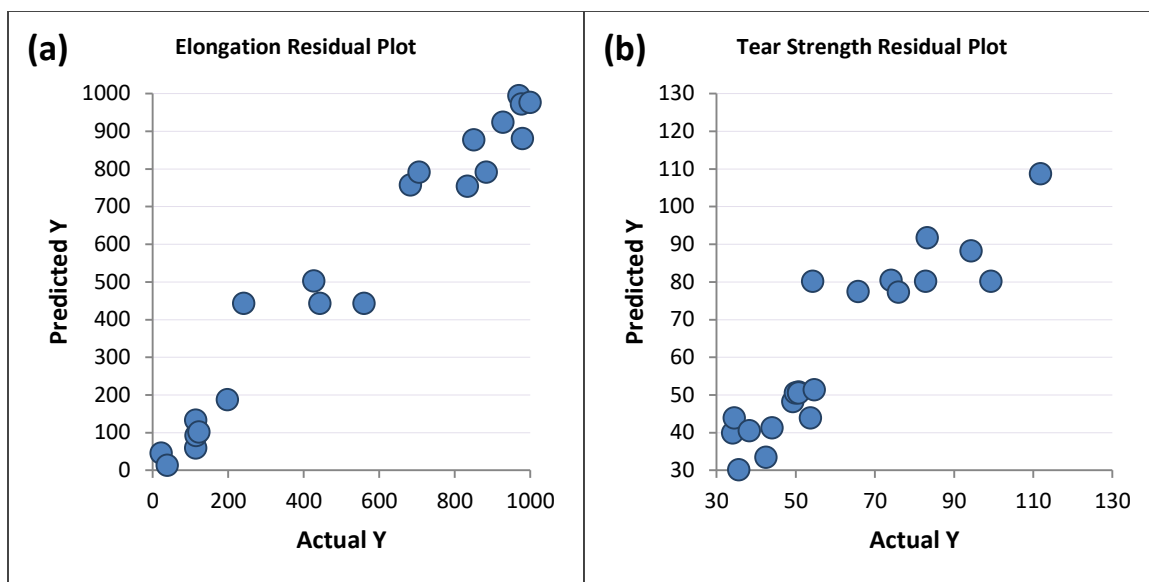


Figure 28: Residual plot of predicted values of elongation (a) and tear strength (b) as compared with test results.

4.4 SEM Imaging

Scanning electron microscopy images were collected for two samples, SN0034 and SN0049. SN0034 is a 20% hard segment sample with a 1.00 index, 93 °C processing temperature, and 46% humidity curing environment. SN0049 is a 40% hard segment sample with 1.05 index, 105 °C curing temperature, and 100% relative humidity during cure. FTIR spectrums for SN0034 indicate 10% of carbonyl groups are H-bonded and well-ordered and 31% H-bonded and disordered groups. SN 0049 FTIR spectras measured 11% of carbonyl groups are H-bonded and ordered and 40% H-bonded and disordered.

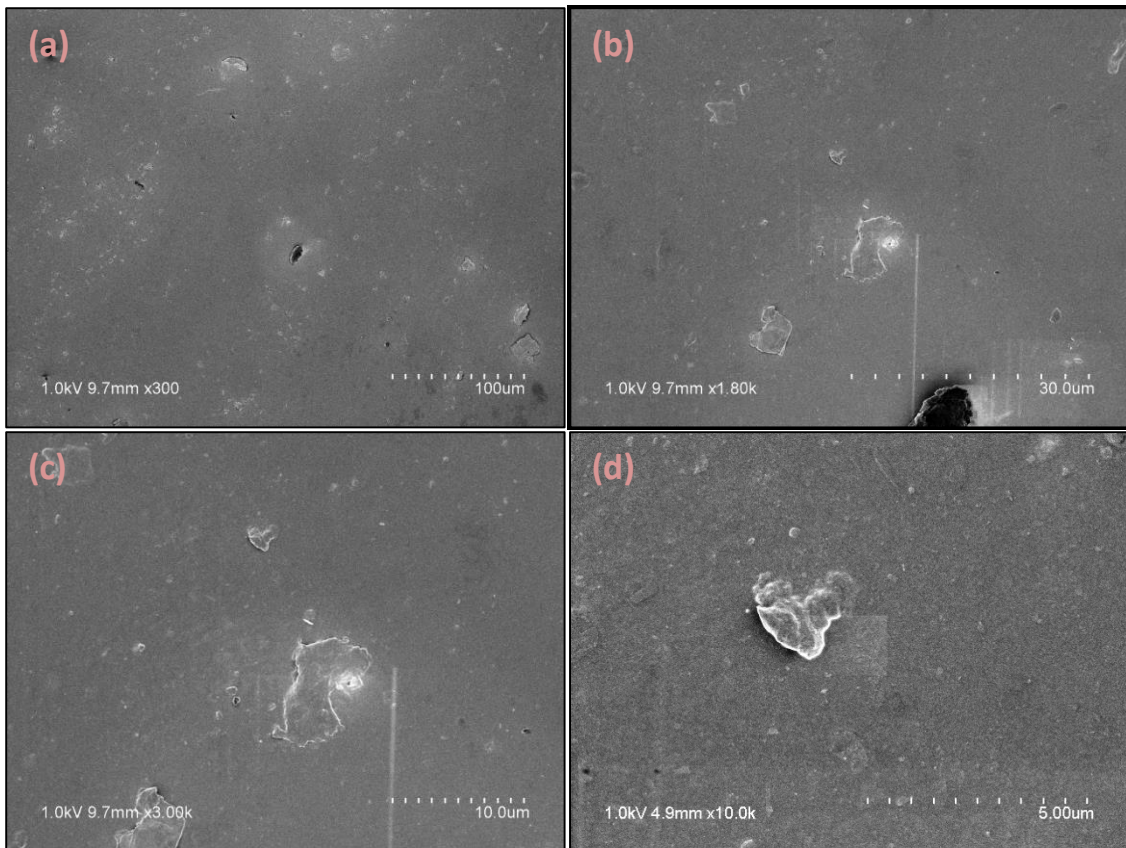


Figure 29: SEM, SE images of SN0034, 20% hard segment urethane. Four magnifications, (a) x300, (b) x1,800, (c) x3,000, (d) x10,000.

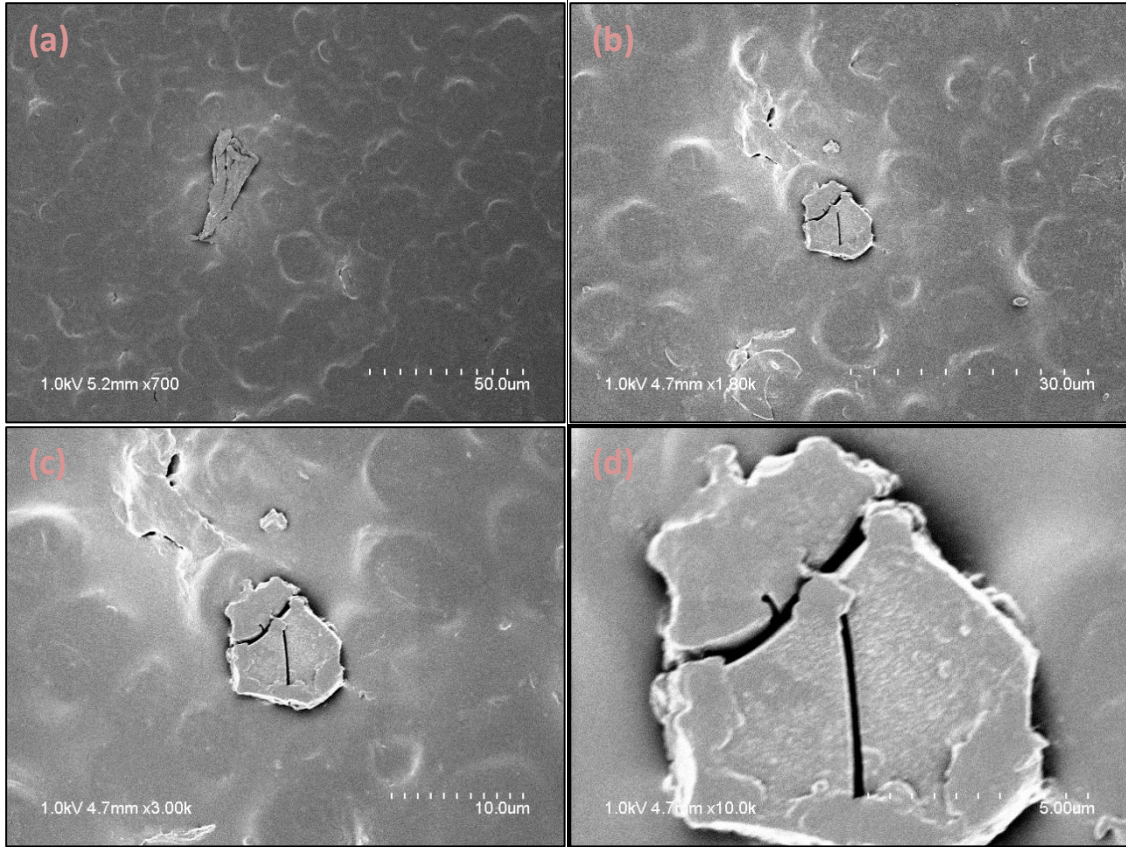


Figure 30: SEM, SE images of SN0049, 40% hard segment urethane. Four magnifications, (a) x700, (b) x1,800, (c) x3,000, (d) x10,000.

Figure 29 and 30 above are SEM images of the secondary electron signal at multiple magnifications and 1keV. As can be seen, SN0034 has relatively few features indicating a low, ordered superstructure development. Small crystalline like particles appear on the order of 5 μm , which appear to not be well incorporated into the matrix. Much smaller phases can be seen (<1 μm) scattered across the specimen. SN0049 shows similar crystalline-like structures roughly 5 μm in size. In addition, faint circular patterns about 5-10 μm are visible which are not evident in SN0034. This pattern is well dispersed across the sample. Higher magnification of these areas was unsuccessful.

CHAPTER V

Section 5: DISCUSSION AND CONCLUSION

5.1 Discussion

The primary goal, as presented in chapter 1 is: to determine the sensitivity of MDI based polyurethane (PUR) materials mechanical and thermal properties to manufacturing controls and environmental conditions. It has been presented in the literature that mechanical and thermal properties are highly dependent on the hard phase of the block copolymer, polyurethane. For this reason, microphase separation is given a great deal of attention and is of primary importance for material design. In this study, the effects of the percentage of hard segment, mixing index, processing temperature, and relative humidity of the curing environment on the microphase separation has been completed by FTIR and DSC. To ensure statistical significance and provide a regression fit model (transfer function), a DOE was followed. 23 of the 78 samples were produced according to a 4 factor-3 level CCD test matrix. SEM imaging of the developed superstructure of two samples has also been presented. Moreover, the effects of the DOE factors on the mechanical and thermal properties has also been completed by tensile and DSC testing. The first objective presented in chapter 1 is to rank the processing factors effects on mechanical properties and material thermal stability. According to the DOE regression results presented, a summary of the coded coefficients are summarized in figure 31. A greater value

indicates a larger impact on the output parameter. The sign of the coefficient indicates the correlation (i.e. positive or negative). However, it must be reemphasized that these values are contingent on a high confidence and orthogonal test samples. Although orthogonality was adequate to create the regression models, further sampling may improve correlation and statistical significance. Moreover, coded coefficients shown below are normalized and may not be used for model coefficients. Coded coefficients primary function is to illustrate the factors impact on outcome variation. Uncoded coefficients are presented in the Appendix B. Coded coefficients for FTIR carbonyl amplitude peak and DSC ΔC_p results are presented in figure 32.

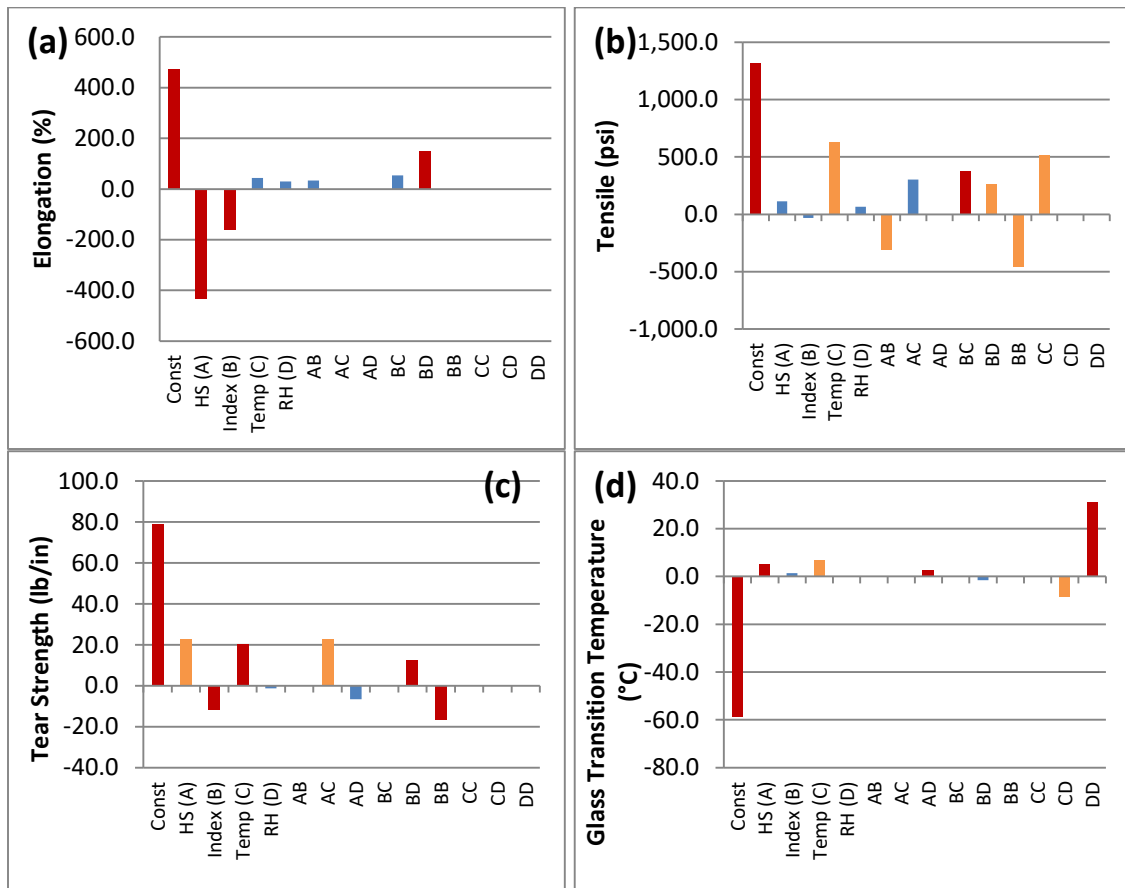


Figure 31: Coded coefficient summary of factor effects on mechanical and thermal properties. (a) elongation at break (%), (b) max tensile strength (psi), (c) tear strength (lb/in), (d) glass transition temperature (°C). P-values < 0.05 and VIF < 1.5 (red), for P-values < 0.05 and VIF > 1.5 (orange), and P-values > 0.05 and VIF > 1.5 (blue).

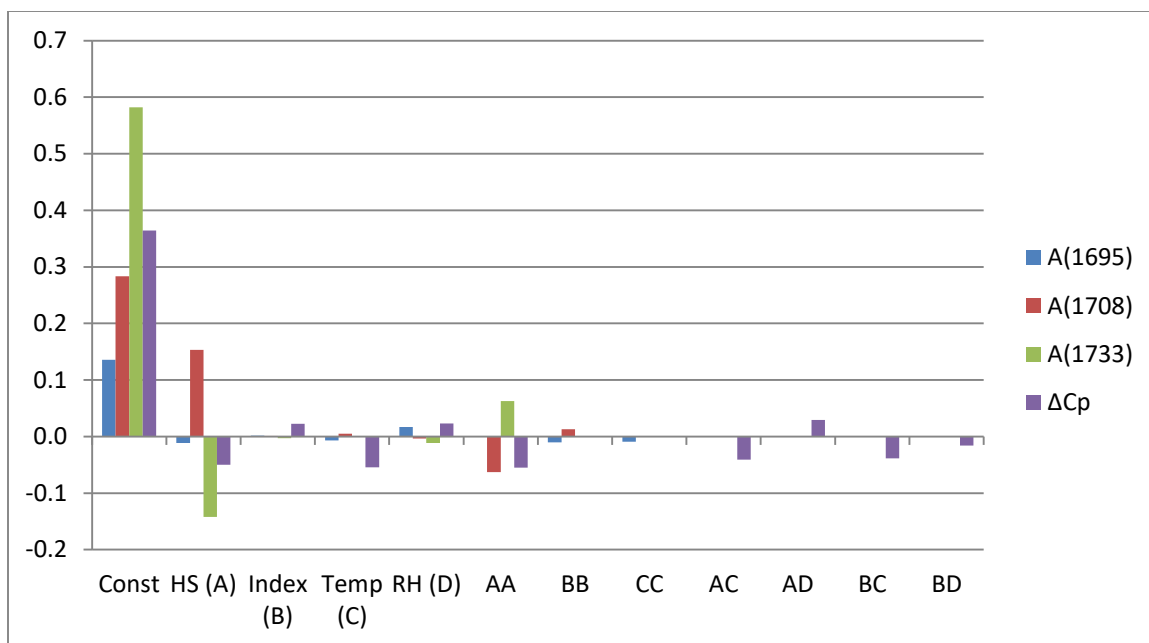


Figure 32: Coded regression coefficients for FTIR carbonyl peaks and DSC ΔC_p .

From figure 31 (a), it is clear that HS, index, and the interaction between index and RH are the largest contributors to elongation. These factors have acceptable statistical correlation. Figure 31 (b) indicates that curing temperature and the quadratic term for index and processing temperature have the largest impact on tensile strength. However, this regression model shows weak correlation to test results. This is due to low orthogonality and aliasing between factors. Figure 31(c) coefficients indicate that the amount of hard segment, processing temperature, and the interaction term between the two has the largest influence over tear strength. Statistical confidence in this model is adequate, but improved orthogonality may give higher confidence. These results indicate that higher %HS and processing temperature may improve tear properties. Figure 31(d) shows large contributions from the quadratic term of the relative humidity. This result shows significant statistical parameters, however, the signal-to-noise may be improved with additional samples and higher resolution testing. If CO_2 from the reaction of the diisocyanate and water molecules were trapped in the elastomer, this could explain this drastic increase in T_g .

Figure 32 indicates that all factors had very little contribution to increases in the FTIR peak centered at 1695 cm^{-1} . However, by increasing the percentage of hard segment, the amplitude at the 1733 cm^{-1} peak decreased as the 1708 cm^{-1} increased. Regression analysis shows significant statistical results. The main effects plot for the 1733 and 1708 cm^{-1} peaks shows that as the 1733 peak decreases, the 1708 cm^{-1} peak increases appropriately.

This phenomenon is contributed to the use of an unsymmetric diisocyanate, MDI. Yilgor, et al have shown the high phase separation of polyurethanes utilizing symmetric diisocyanate molecules. Therefore, the results show that by increasing the amount of hard segment while using an unsymmetrical diisocyanate, H-bonding is promoted. However, an ordered microphase separated structure is not.

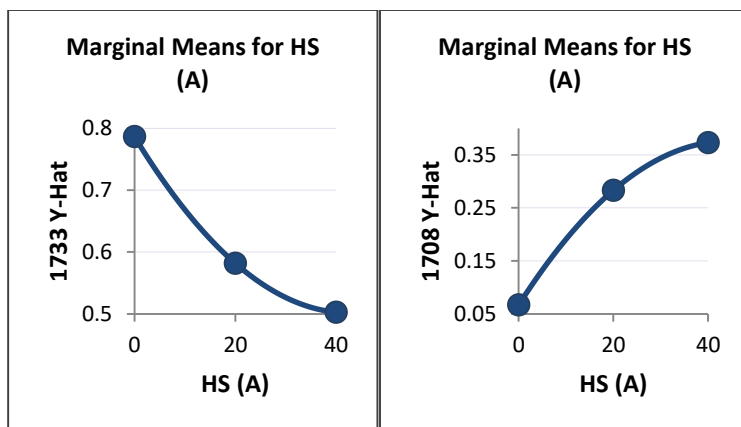


Figure 33: Main effects plot of 1733 and 1708 cm^{-1} carbonyl peaks. Index = 1.00, Temp = $93\text{ }^{\circ}\text{C}$, and RH = 73% are held constant.

The increase in the 1708 cm^{-1} appears to contribute primarily to the improvement of tear strength, but also a large reduction in elongation. However, this does not appear to contribute to a large improvement in tensile strength. Additional testing is required to confirm this. It is hypothesized that the addition of this larger hydrogen bonded structure creates blunting to crack growth. With the improvement of phase separation, the closer proximity of urethane rich regions

may contribute to higher hydrogen bonding, and therefore, it may contribute to improved mechanical strength.

From the DSC results, it can be seen that as the amount of hard segment is increased, the change in the specific heat at the glass transition is reduced. The quadratic term is also significant indicating a second order interaction. This result is consistent with DSC testing of a 72 %HS sample which shows no glass transition, therefore, a ΔC_p of zero. Moreover, the DSC results indicate that the mixing temperature also has a negative impact on the ΔC_p . The interaction term between the %HS and mix temperature is negatively correlated and shows a possible statistical significance. The change in the specific heat at the glass transition temperature may be attributed to the amorphous segments of the sample. Therefore, as the ΔC_p at this temperature decreases, it can be said that the sample is more crystalline. The large effect of the hard segment on this value is consistent with FTIR results. However, these results also indicate that the mix temperature has a significant effect. FTIR results indicate very poor correlation of the 1708 cm^{-1} peak with mix temperature. However, the 1685 cm^{-1} peak indicates a possible correlation (P-value = 0.098). It can be seen from the tear results in figure 31(c) that the mix temperature has a large positive contribution. Therefore, these results show that by increasing the mix temperature, a higher degree of crystallinity is achieved resulting in improved tear strengths.

5.2 Conclusion

In conclusion, this thesis has studied the effect of the amount of hard segment, mix index, mix temperature, and environment humidity on the microstructure and the mechanical and thermal properties. It has been shown through FTIR that the amount of hard segment has a very large effect on the degree of hydrogen bonding. Moreover, the hard segment has a large contribution to the elongation at break and tear strength. A higher mix temperature appears to promote higher crystallinity as shown through DSC resulting in improved tear strength. The mixture index at the limits chosen, shows only minor effects on elongation and tear strength.

Finally, the humidity shows a large contribution to the glass transition temperature. However, no other humidity effects could be detected with significance.

5.3 Future Work

Although some of the statistical parameters show high confidence, improved orthogonality of some factors is needed. It is recommended that VIF is reduced below at least 1.5. Many factors indicated significant terms (p -value < 0.05), however, the low orthogonality did not allow for a conclusion. Additional runs could help alleviate this issue. More repetitions would also allow for a regression model for the standard deviation and possibly improved p -values.

If tensile testing is conducted, it is recommended that improved mixing techniques be setup to reduce the entrapment of air. This could be achieved with a batch mixer. The use of a compression molding process may also reduce air entrapment. Moreover, it is recommended that all samples are manufactured quickly and within a small time frame to reduce any deterioration of diisocyanate and the need for multiple melting down of the polyols. The effects of this are unknown, however, this may have introduced additional variation. The completion of DMA testing is also needed to study the viscoelastic nature of these samples.

The effects of humidity did not show any detectable peaks at the 1635 cm^{-1} . Higher resolution of the carbonyl region of the FTIR spectrum could improve the deconvolution of the peaks and reduce regression variability. In addition, the reduction of the low amplitude noise in this region may reveal a 1635 cm^{-1} peak. This could be achieved with more background scans or a different ATR crystal such as germanium. Further investigation of the FTIR spectrum may indicate the formation of allophanate, biuret, or other crosslinking peaks that could reveal additional information of morphological developments. However, the author is not aware of any unique peaks for these formations. The synthesis of samples with symmetrical diisocyanates at varying temperatures may indicate any significant correlation to improved crystallinity of the hard segment. SEM at higher magnifications may also produce images of spherulite formations

which may give clues into the sizes of the hard segments and its growth in either a radial or tangential pattern. Finally, an analysis of the type I and type II DSC endotherm is recommended for distinguishing of the types of hard segment development.

REFERENCES

- [1] R. Palinkas, *Journal of elastomers and plastics* 23 (1991) 22-23.
- [2] M. Alger, *Polymer science dictionary*, Springer Science & Business Media, 1996.
- [3] C. Schollenberger, K. Dinbergs, F. Stewart, *Rubber Chemistry and Technology* 55 (1982) 137-150.
- [4] C. Wang, D. Klempner, K. Frisch, *Journal of applied polymer science* 30 (1985) 4337-4344.
- [5] I. Yilgör, E. Yilgör, G.L. Wilkes, *Polymer* 58 (2015) A1-A36.
- [6] E. Yilgör, I.s. Yilgör, *Polymer* 42 (2001) 7953-7959.
- [7] R. Bonart, E. Müller, *Journal of Macromolecular Science, Part B: Physics* 10 (1974) 177-189.
- [8] Y. Camberlin, J.P. Pascault, *Journal of Polymer Science: Polymer Physics Edition* 22 (1984) 1835-1844.
- [9] V. Vilensky, Y. Lipatov, *Polymer* 35 (1994) 3069-3074.
- [10] A. Askadskii, Y.I. Matveev, *Khimiya*, Moscow (1983) 101-120.
- [11] H. Staley, D.J. David, *Analytical chemistry of the polyurethanes*, New York, Robert E. Krieger, 1979.

- [12] S.G. Entelis, O. Nesterov, Russian Chemical Reviews 35 (1966) 917.
- [13] R. Herrington, R. Turner, W. Lidy, Flexible polyurethane foams. Freeport, USA: The Dow Chemical Company (1997) 3.1-3.57.
- [14] A.L. Silva, J.C. Bordado, Catalysis reviews 46 (2004) 31-51.
- [15] D.A. Welch, Polyurethane Manufacturer's Association (2012).
- [16] B.S. Kim, B.K. Kim, Journal of applied polymer science 97 (2005) 1961-1969.
- [17] R.W. Fuest, Polyurethane Elastomers, Chapter, 2001.
- [18] J. Florio, R. Ravichandran, B. Hsieh, R. Coughlin, Adhesives & Sealants Industry 18 (2011) 20-26.
- [19] Dow Polyurethanes - Functionality, OH Number, and Equivalent Weight Definitions, Dow Answer Center.
- [20] P. Krol, Progress in materials science 52 (2007) 915-1015.
- [21] K. Dusek, M. Spirkova, I. Havlicek, Macromolecules 23 (1990) 1774-1781.
- [22] M. Morton, Rubber technology, Springer Science & Business Media, 2013.
- [23] E. Yilgör, I. Yilgör, E. Yurtsever, Polymer 43 (2002) 6551-6559.
- [24] S. Parnell, K. Min, M. Cakmak, Polymer 44 (2003) 5137-5144.
- [25] J.S. Bergstrom, M.C. Boyce, Rubber chemistry and technology 72 (1999) 633-656.
- [26] Z. Hashin, Journal of Applied Mechanics 50 (1983) 481-505.
- [27] T. Lewis, L. Nielsen, Journal of Applied Polymer Science 14 (1970) 1449-1471.
- [28] R.F. Landel, L.E. Nielsen, Mechanical properties of polymers and composites, CRC Press, 1993.

- [29] S.-Y. Fu, X.-Q. Feng, B. Lauke, Y.-W. Mai, *Composites Part B: Engineering* 39 (2008) 933-961.
- [30] J.K. Fink, *Reactive polymers fundamentals and applications: a concise guide to industrial polymers*, William Andrew, 2013.
- [31] N.G. Sahoo, Y.C. Jung, H.J. Yoo, J.W. Cho, *Macromolecular chemistry and physics* 207 (2006) 1773-1780.
- [32] E.A. Meinecke, M.I. Taftaf, *Rubber chemistry and technology* 61 (1988) 534-547.
- [33] Z. Liu, G. Bai, Y. Huang, F. Li, Y. Ma, T. Guo, X. He, X. Lin, H. Gao, Y. Chen, *The Journal of Physical Chemistry C* 111 (2007) 13696-13700.
- [34] M. Vatani, E.D. Engeberg, J.-W. Choi, *Sensors and Actuators A: physical* 195 (2013) 90-97.
- [35] C.R. Lee, S. Grad, K. Gorna, S. Gogolewski, A. Goessl, M. Alini, *Tissue engineering* 11 (2005) 1562-1573.
- [36] R. Silva, D. Spinelli, W. Bose Filho, S.C. Neto, G. Chierice, J. Tarpani, *Composites Science and Technology* 66 (2006) 1328-1335.
- [37] Y.Q. Rao, J. Munro, S.R. Ge, E. Garcia-Meitin, *Polymer* 55 (2014) 6076-6084.
- [38] S.A. Madbouly, J.U. Otaigbe, *Progress in Polymer Science* 34 (2009) 1283-1332.
- [39] T.K. Chen, Y.I. Tien, K.H. Wei, *Polymer* 41 (2000) 1345-1353.
- [40] F.G. Ornaghi, V. Pistor, R.V.B. de Oliveira, *Journal of Applied Polymer Science* 132 (2015) 10.
- [41] I. Javni, K. Song, J. Lin, Z.S. Petrovic, *Journal of cellular plastics* 47 (2011) 357-372.

- [42] J.S. Bergstrom, *Mechanics of solid polymers: theory and computational modeling*, William Andrew, 2015.
- [43] M.J. Doyle, *Polyurethane Manufacturer's Association*.
- [44] R. Rivlin, A. Thomas, *Polymer Science* 10 (1953) 291.
- [45] A. Gent, *Fracture of Nonmetals and Composites* (2013) 315.
- [46] R.P. Robert D. Cody, *Polyurethane Manufacturer's Association* (1989).
- [47] E.A. Meinecke, *Dynamic Properties of Elastomers*, *Polyurethane Manufacturing Association*.
- [48] M.T. Shaw, W.J. MacKnight, *Introduction to polymer viscoelasticity*, John Wiley & Sons, 2005.
- [49] B. McGinty, *Dynamic Material Properties*, *Continuum Mechanics*, vol 2016.
- [50] L.W. McKeen, *The effect of creep and other time related factors on plastics and elastomers*, Elsevier, 2009.
- [51] Y.-c. Fung, *Biomechanics: mechanical properties of living tissues*, Springer Science & Business Media, 2013.
- [52] N. El-Tayeb, R.M. Nasir, *Wear* 262 (2007) 350-361.
- [53] A. Muhr, A. Roberts, *Wear* 158 (1992) 213-228.
- [54] A. Schallamach, *Journal of Applied Polymer Science* 12 (1968) 281-293.
- [55] W. Arayaprane, *Abrasion Resistance of Materials*, InTech, Rijeka (2012) 147-166.
- [56] P.J. Flory, *Principles of polymer chemistry*, Cornell University Press, 1953.
- [57] P. Elmer, *A beginners Guide*, *Dynamic Mechanical Analysis* 2008.
- [58] M. Marc, *Technical paper* (2005).

- [59] B.C. Smith, Fundamentals of Fourier transform infrared spectroscopy, CRC press, 2011.
- [60] D.C. Folz, Variable Frequency Microwave Curing of Polyurethane, Material Science and Engineering, vol Master of Science in Materials Science and Engineering, Virginia Polytechnic Institute and State University, Polyurethane Manufacturing Association, 2011, p. 115.
- [61] I. Yilgor, E. Yilgor, I.G. Guler, T.C. Ward, G.L. Wilkes, Polymer 47 (2006) 4105-4114.
- [62] A. Frick, A. Rochman, Polymer Testing 23 (2004) 413-417.
- [63] R.M. Briber, E.L. Thomas, Journal of Macromolecular Science, Part B: Physics 22 (1983) 509-528.
- [64] A. Aneja, G.L. Wilkes, Polymer 44 (2003) 7221-7228.
- [65] S. Samuels, G. Wilkes, The rheo-optical and mechanical behavior of a systematic series of hard-soft segmented urethanes, Journal of polymer science: Polymer symposia, vol 43, Wiley Online Library, 1973, pp. 149-178.
- [66] S.R. Schmidt, R.G. Launsby, Understanding industrial designed experiments, Air Academy Press, 1989.
- [67] M.J. Kiemele, S.R. Schmidt, R.J. Berdine, Basic statistics: tools for continuous improvement, Air academy press, 1997.
- [68] Handbatching, Chemtura, Adiprene/Vibrathane/Duraast Library, 2001.
- [69] Dow Polyurethane - MDI Prepolymers Lab Preparation, vol 2016, Dow Answer Center, 2014.

- [70] R. Koningsveld, W.H. Stockmayer, E. Nies, Polymer phase diagrams: a textbook, Oxford University Press, USA, 2001.
- [71] L.M. Robeson, Hanser, Munich (2007) 24-149.
- [72] V.V. Tereshatov, M.A. Makarova, V.Y. Senichev, E.R. Volkova, Z.A. Vnutsikh, A.I. Slobodinyuk, Colloid and Polymer Science 293 (2015) 153-164.
- [73] J. Bicerano, Computational modeling of polymers, CRC press, 1992.
- [74] A. Noshay, J.E. McGrath, Block copolymers: overview and critical survey, Elsevier, 2013.
- [75] W. Bras, G. Derbyshire, D. Bogg, J. Cooke, Science 267 (1995) 996.
- [76] D.W. Van Krevelen, K. Te Nijenhuis, Properties of polymers: their correlation with chemical structure; their numerical estimation and prediction from additive group contributions, Elsevier, 2009.
- [77] A.F. Barton, CRC handbook of solubility parameters and other cohesion parameters, CRC press, 1991.

APPENDICES

Appendix A: Additional Testing Results

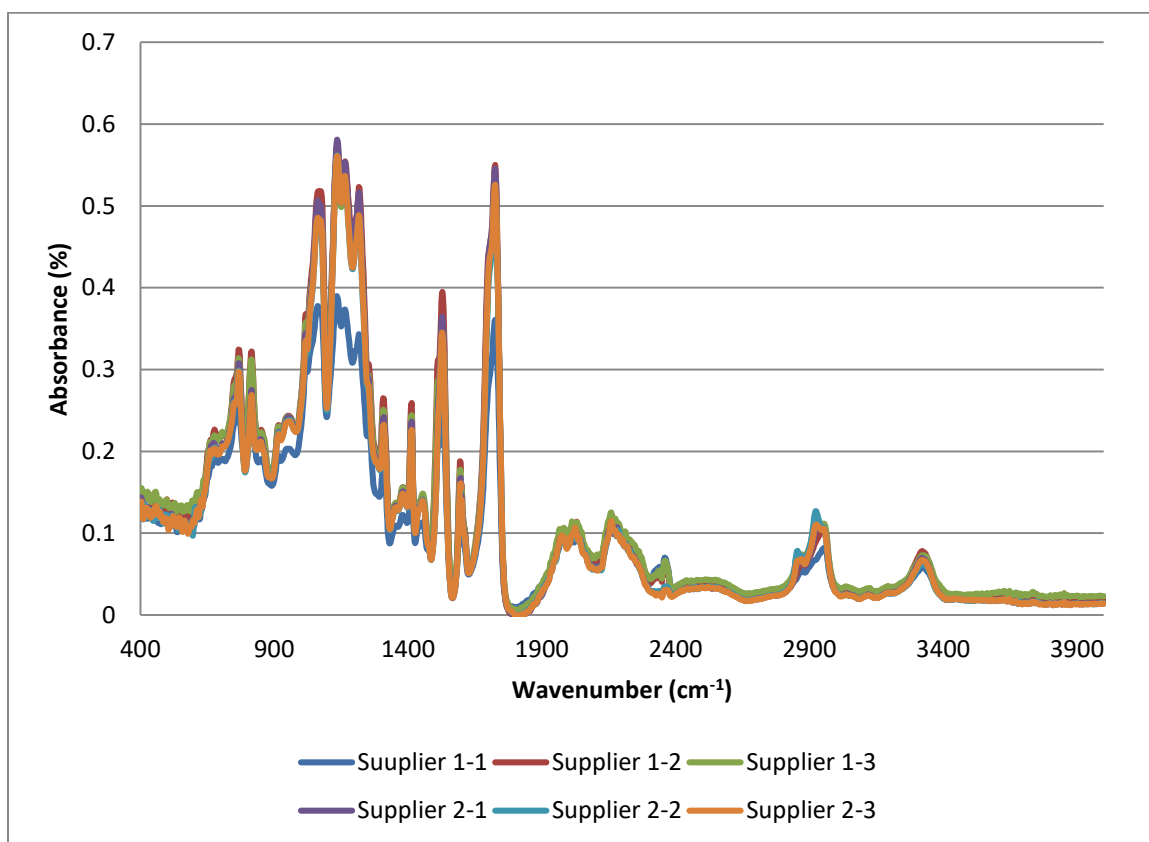


Figure 34: Full spectrum of manufacturer supplied MDI, BD, ester based polyurethane.

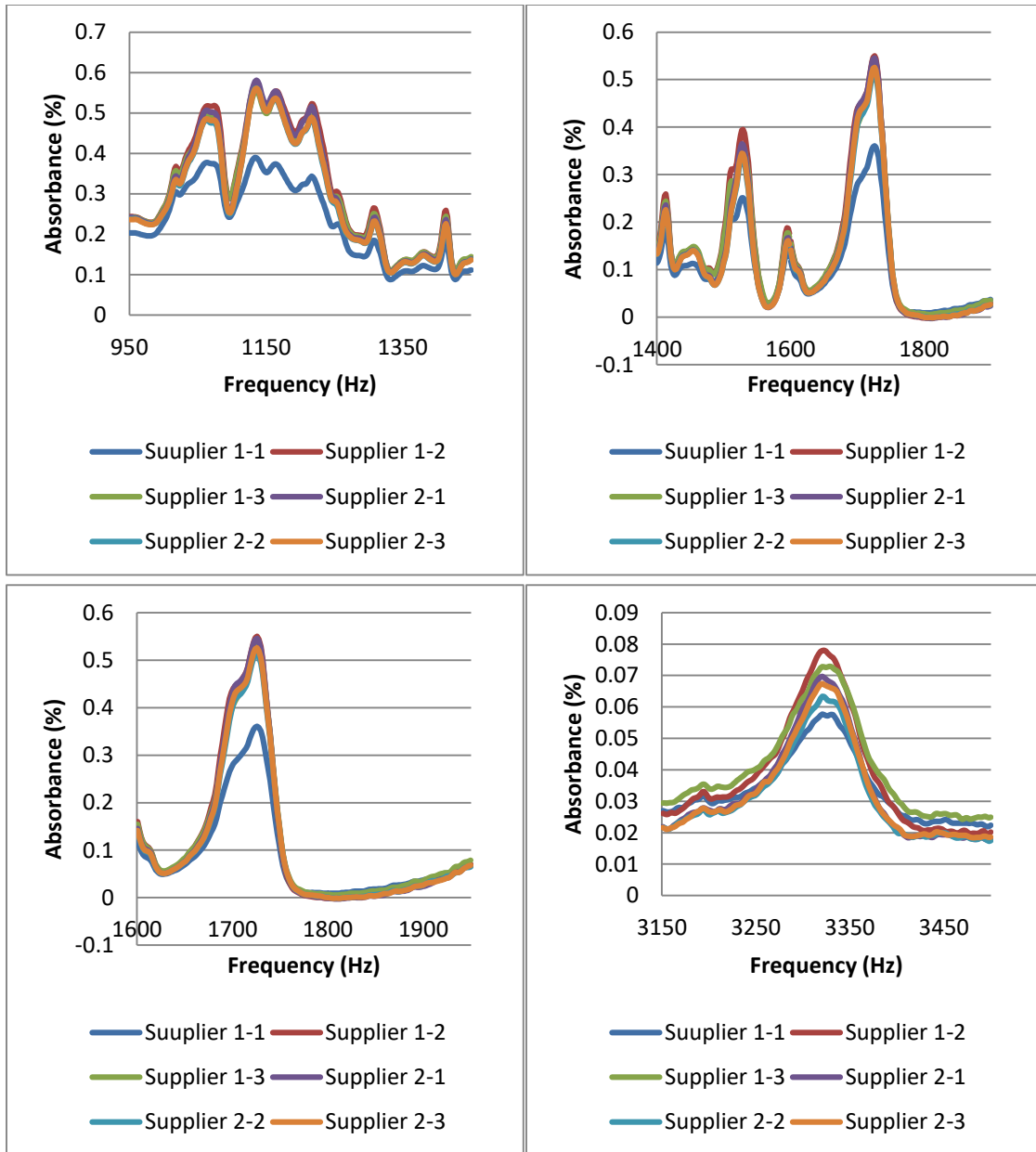


Figure 35: Selected regions of manufacturer supplied MDI, BD, ester based polyurethane.

Appendix B: Uncoded Regression Coefficients

In these regression tables, care must be taken to insure that the proper units are used and that the numerical values remain within the bounds of the values tested. Moreover, statistical parameters must be checked from the coded regression tables.

Factor	Elongation	Tensile	Tear
Const	20,876.0	-85,528.8	-5,650.06
HS (A)	-55.692	194.852	-6.6827
Index (B)	-20,384.3	297,002	12,336.5
Temp (C)	-86.937	-1,267.1	-0.1953
RH (D)	-109.093	-190.724	-9.1864
AB	34.003	-306.966	
AC		1.2669	0.0938
AD			-0.0123
BC	90.547	630.329	
BD	110.185	193.206	9.3872
BB		-182,103	-6,626.76
CC		3.5698	

Table 17: Uncoded coefficients for tensile DOE.

Factor	Tg	delta Cp
Const	-173.321	-5.7103
HS (A)	-0.113	0.0175
Index (B)	112.09	6.16
Temp (C)	2.485	0.0618
RH (D)	-2.7302	-0.0002
AC		-0.0002
AD	0.0052	0.0001
BC		-0.0626
BD	-1.1671	
CD	-0.026	
AA		-0.0001
CC		
DD	0.0426	

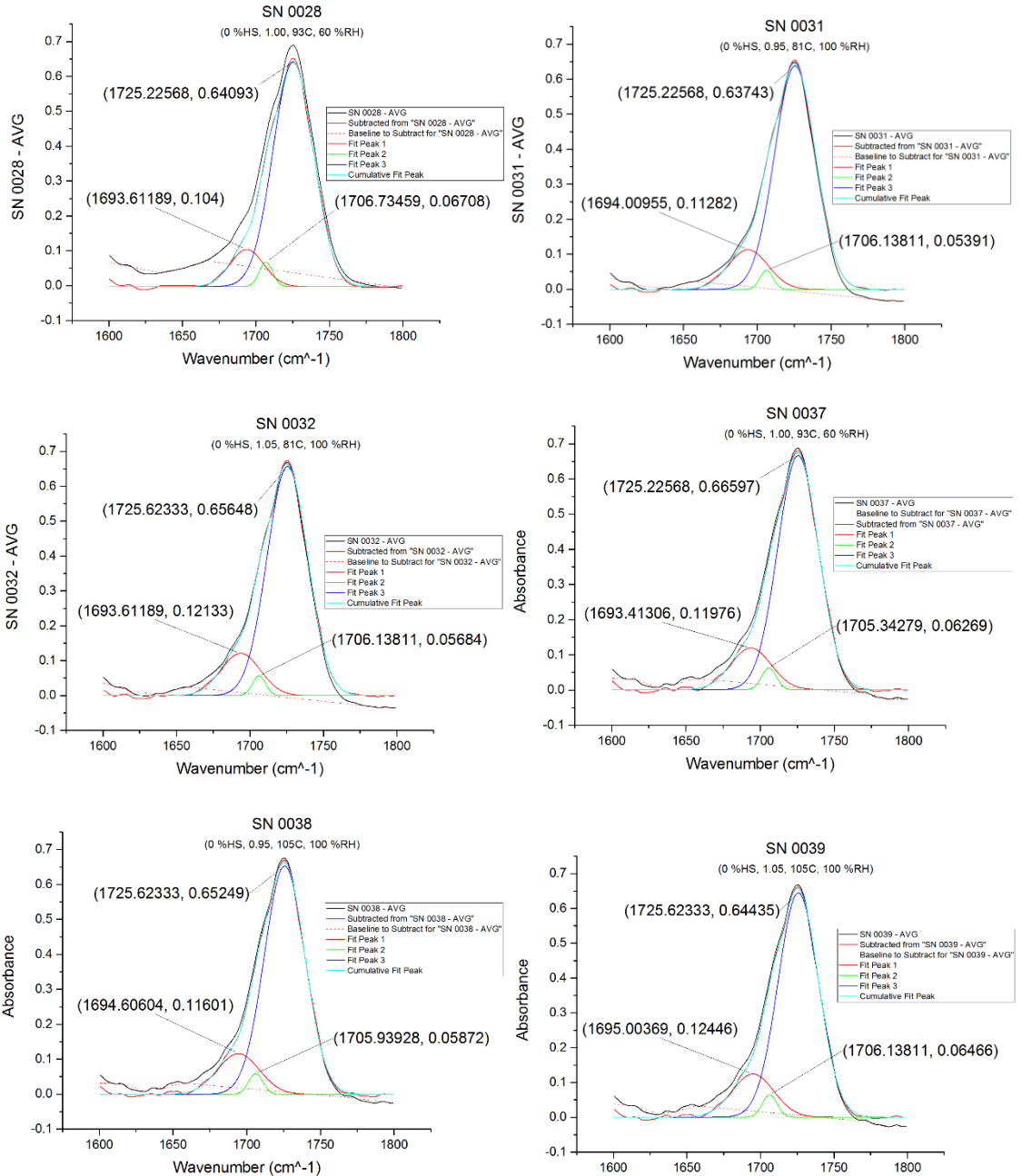
Table 18: Uncoded coefficients for DSC DOE.

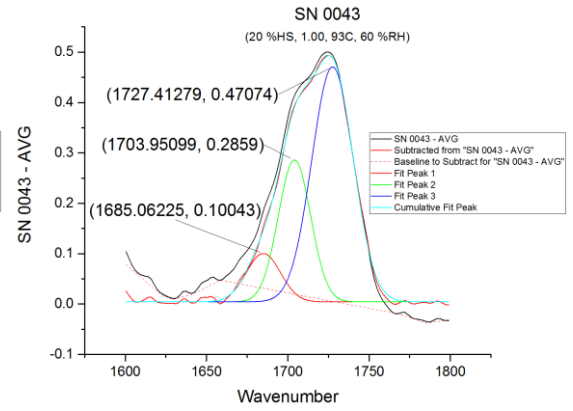
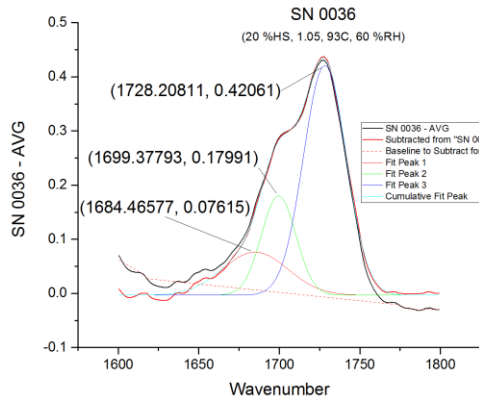
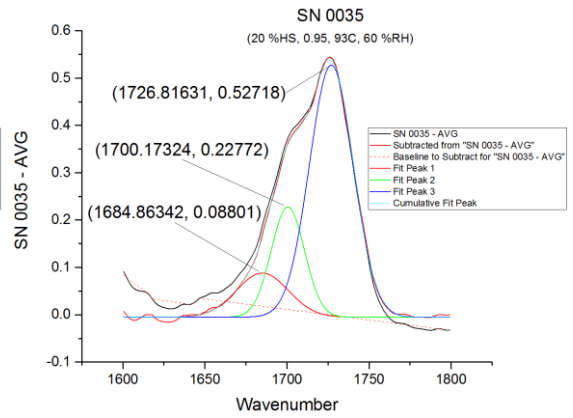
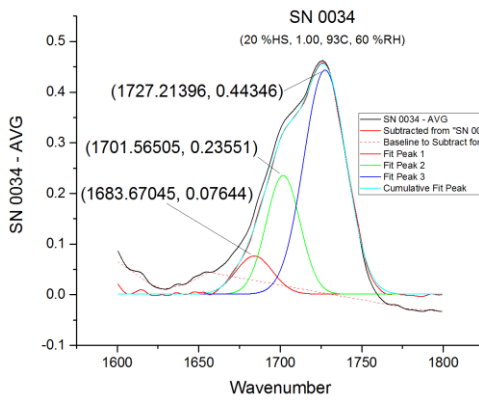
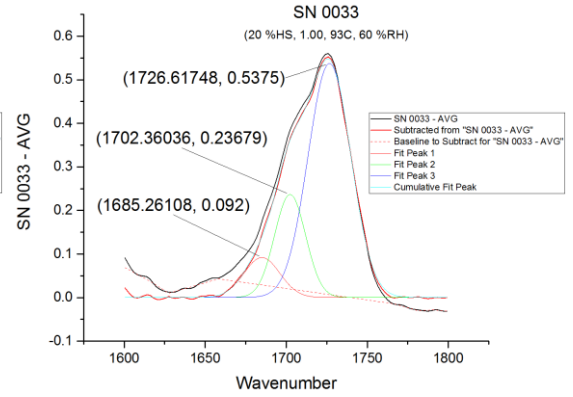
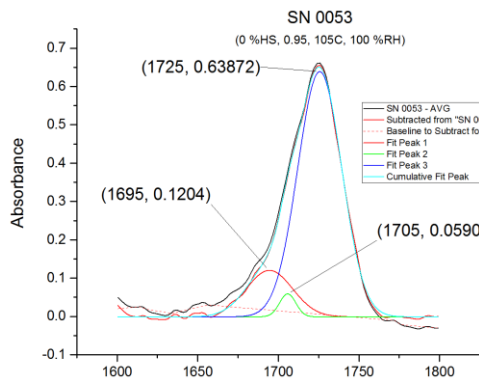
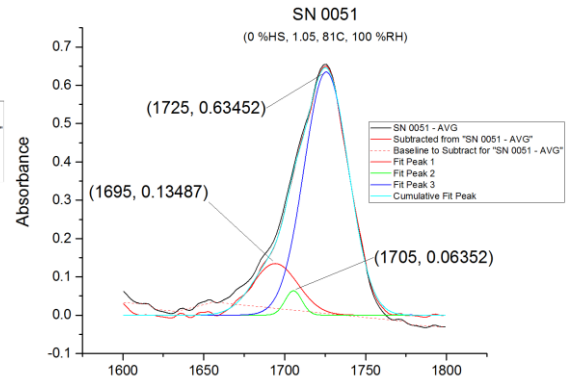
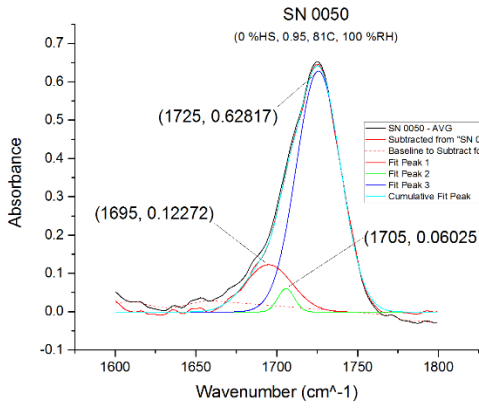
Factor	1695	1708	1733
Const	-4.6354	5.1075	0.8756
HS (A)	-0.0006	0.014	-0.0134
Index (B)	8.4856	-10.168	-0.0596
Temp (C)	0.0109	0.0004	0.0
RH (D)	0.0006	-0.0001	-0.0004
AA		-0.0002	0.0002
BB	-4.228	5.0968	
CC	-0.0001		

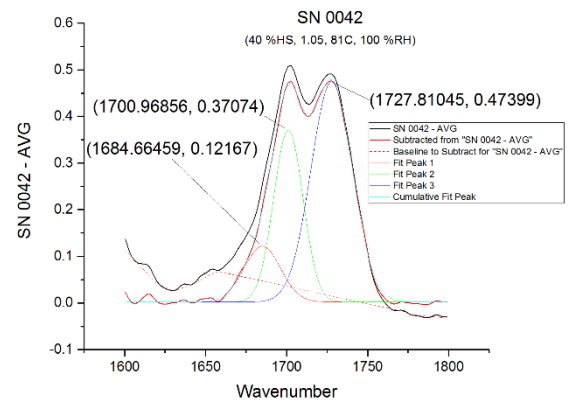
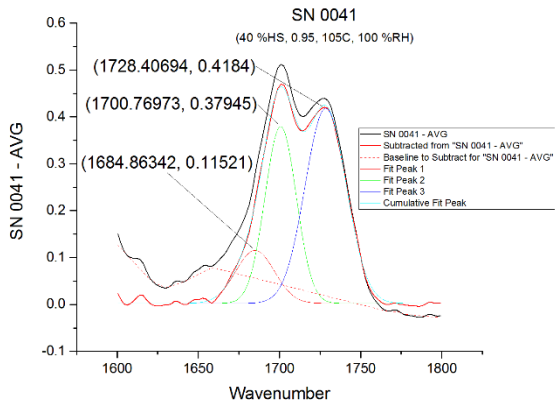
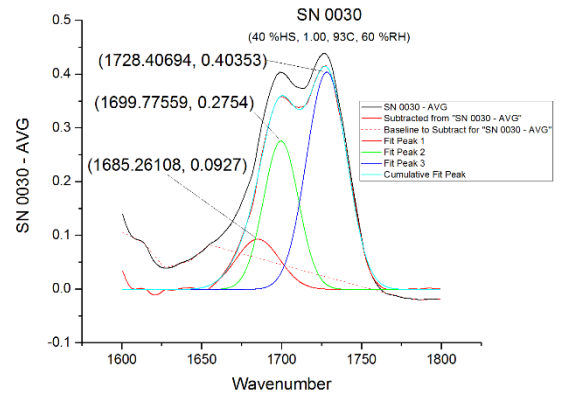
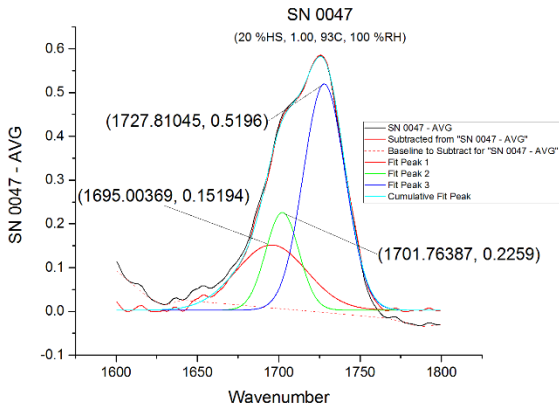
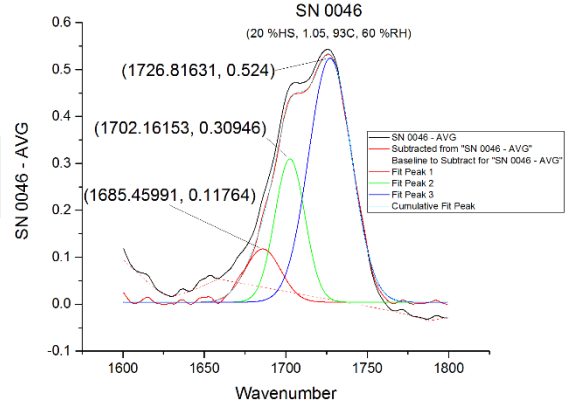
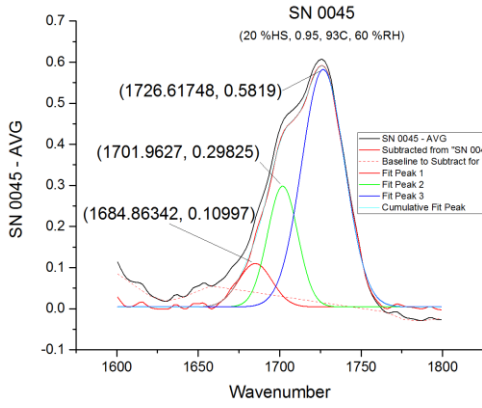
Table 19: Uncoded coefficients for FTIR DOE

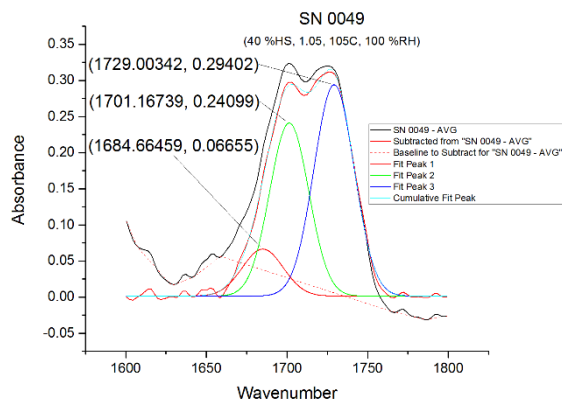
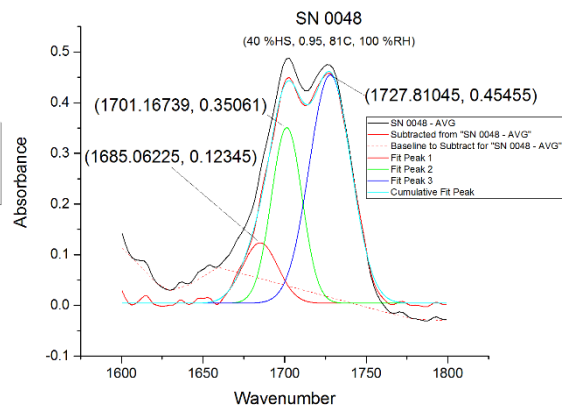
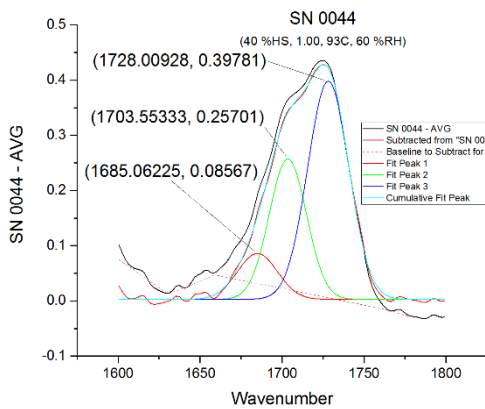
Appendix C: FTIR Peak Deconvolution

The following graphs show the peak deconvolution analysis completed on carbonyl peaks between 1600 and 1800 cm^{-1} . First, a baseline was subtracted. Second, peak deconvolution with a gauss fit was done at three peaks. The amplitude and the center of each peak are used as DOE inputs.

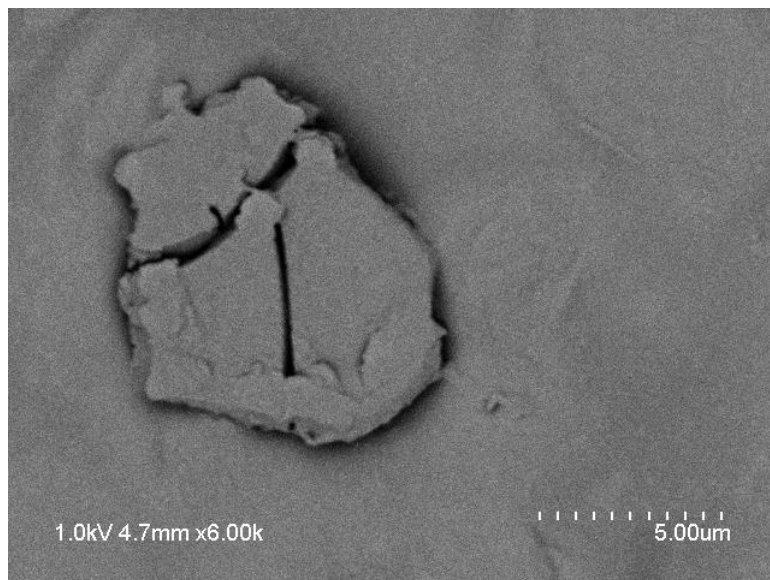
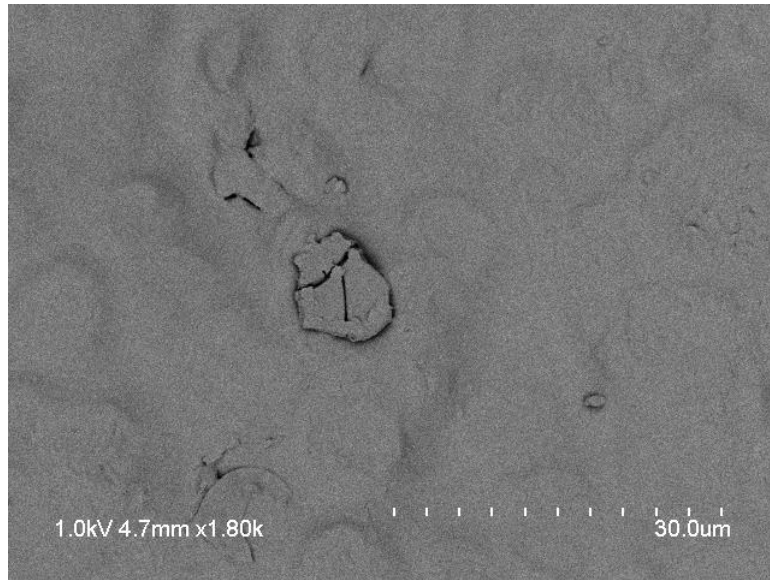








Appendix D: BSE SEM of SN0049



Appendix E: Microphase Separation

The classical Gibbs free energy of mixing (equation D1) can be calculated. If negative, then the mix will be thermodynamically miscible. If positive, microphase separation will occur.

$$\Delta G_m = \Delta H_m - T\Delta S_m, \quad (eq. D1)$$

However, the satisfaction of a negative Gibbs free energy is not sufficient to insure mixing. In addition, the following equation must also be satisfied:

$$\left(\frac{\partial^2 \Delta G_m}{\partial \phi_i^2} \right)_{T,P} > 0, \quad (eq. D2)$$

Typically, with lower molecular weight molecules, increasing temperature is sufficient enough to drive the entropy term higher. This drives the Gibbs free energy more negative. However, with higher weight molecular phases, temperature dependencies of the enthalpy term can dominate and decrease miscibility with increased temperatures. Polymer-polymer blends, such as in a urethane block copolymer, exhibit a lower critical stable temperature (LCST). An upper critical solution temperature (UCST) is more common for liquid-liquid and polymer-liquid solutions. Figure 36 below shows an illustration of the LCST and UCST with the binodal and spinodal curves. The binodal is the curve where the individual chemical potentials of a binary mixture are equal. This is also called the coexistence curve. As described by the IUPAC, the binodal is a point at a specific temperature and composition, that when crossed, a miscibility transition occurs from either single, metastable, or unstable phase separation. The spinodal curve is when equation D2 above is satisfied. These points represent limits of instability [70].

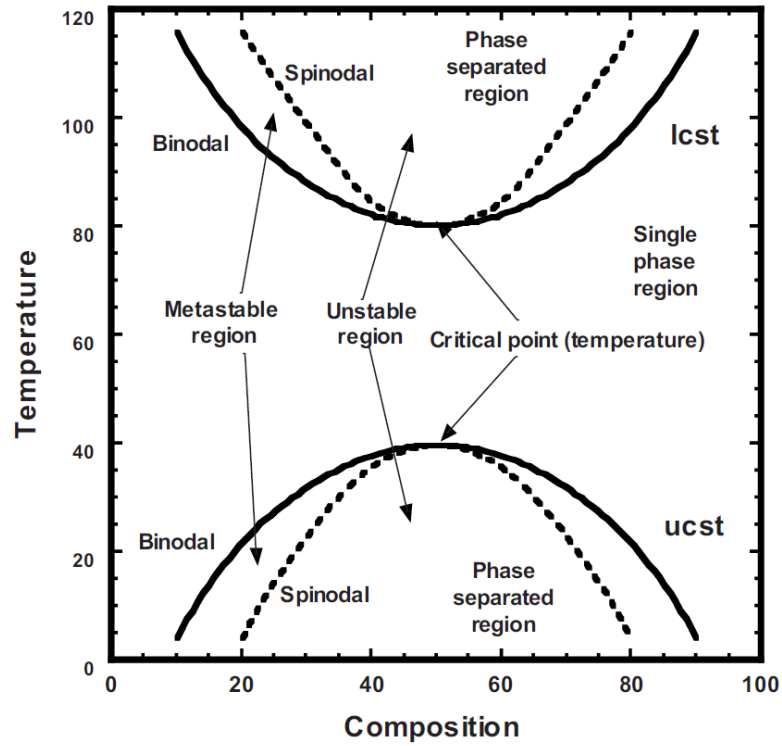


Figure 36: Phase diagram with both LCST and UCST on the binodal and spinodal thermodynamic curves [71].

Mixtures above this mix temperature will result in a phase separated product, whereas below this temperature results in a single phase [71]. However, LCST behavior is not always exhibited. At very low temperatures, glassy transition can occur before phase separation. At high temperatures, polymer degradation can occur. A useful model used to model free energy of binary polymer blends is the Flory-Huggins theory. The equation of this theory is stated below:

$$\Delta G_m = RTV \left(\frac{\phi_1}{V_1} \ln(\phi_1) + \frac{\phi_2}{V_2} \ln(\phi_2) \right) + \frac{\phi_1 \phi_2 \chi_{12} kTV}{v_r}, \quad (\text{Molecular Basis}) \quad (\text{eq. D3})$$

$$\Delta G_m = RTV \left(\frac{\phi_1}{v_1} \ln(\phi_1) + \frac{\phi_2}{v_2} \ln(\phi_2) \right) + \frac{\phi_1 \phi_2 \chi_{12} RTV}{v_r}, \quad (\text{Molar Basis}) \quad (\text{eq. D4})$$

where V is the total volume, R is the Gas constant, k is the Boltzmann constant, ϕ_i is the volume fraction of i, V_i is the molecular volume of i, v_i is the molar volume of the i polymer chain, v_r is

the molecular or molar volume of a specific segment, and χ_{12} is the Flory-Huggins interaction parameter. Typically, $v_r = (v_1 v_2)^{1/2}$.

Using equation (D4) and equation (D1), the following is derived:

$$\Delta H_m = \frac{\phi_1 \phi_2 \chi_{12} RTV}{v_r} = \phi_1 \phi_2 B_{12} V, \quad (\text{eq. D5})$$

$$-T\Delta S_m = RTV \left(\frac{\phi_1}{v_1} \ln(\phi_1) + \frac{\phi_2}{v_2} \ln(\phi_2) \right), \quad (\text{eq. D6})$$

The morphology of the polyurethane can have large influences on the material properties. These segments are different both chemically and physically. They give polyurethane many unique physical properties such as its very high elasticity while maintaining good load bearing capability [72]. The amount of separation is due to the molecular weight and the amount of interaction between chains, as discussed above [5].

However, limitations do exist for the use of the Flory-Huggins approach. No volume changes during mixing are allowed because an incompressible model is assumed. In some mixtures, a non-additive volume-composition behavior will influence both the enthalpy term (equation D5) and entropy term (equation D6) [71]. In the application to polyurethane copolymers, the above equations may be inadequate due to the following [73]:

- 1) *Intermolecular interactions* between nearby polymer chains such as entanglements, intermolecular fitting, and bonding (e.g. monodentate and bidentate hydrogen bonding between urethane and urea molecules respectively)
- 2) *Intramolecular interactions* such as steric hindrance and conjugation of pi-electrons in double bonds or aromatic rings which increase torsional and bending stiffness of chains.
- 3) Strong covalent junction bonds between chains with increased tensional stiffness.

Due to the covalently bonded blocks, an interfacial tension occurs which must be taken into account. These all add negatively to the entropic term. The Flory-Huggins approach however has been used accurately, with modifications to account for the covalently bonded chains in classic weakly bonded block copolymers such as styrene-butadiene-styrene [74]. Except for these weakly bonded block copolymers, there are relatively few junctions as compared to urethane which is the focus of this study.

It has been shown that the thermal and mechanical properties of high molecular weight multiphase thermoplastics, such as polyurethane and poly(urethane urea), are dependent on the following three microstructure characteristics [6]:

- 4) The amount of microphase separation between hard and soft segments
- 5) Degree of hydrogen bonding within the hard segments
- 6) Degree of crystallization of the hard segment

Bras et. al. have shown that, in general, high polarity hard segments promote improved phase separation and allow for hydrogen bonding with soft segment carbonyl in ester chains or oxygens in ethers [75]. The ability for a group to form a hydrogen bond can be described by its cohesive energy densities (CED) or the Hildebrand solubility parameter (δ) [73, 76, 77].

$$\delta^2 = \delta_d^2 + \delta_p^2 + \delta_h^2 = E_{CED}, \quad (eq. D7)$$

where δ_d is the dispersion due to London forces, δ_p is the dispersion due to dipole forces, and δ_h is the dispersion due to the hydrogen bonding. A large value of δ indicates a highly polar molecule, which, if paired with a low polar molecule will promote microphase separation. Solubility parameters can be related back to the enthalpy of mixing by

$$\Delta h_m = \frac{\Delta H_m}{V} = \phi_1 \phi_2 (\delta_1 - \delta_2)^2, \quad (eq. D8)$$

VITA

Tarek Kandalaft

Candidate for the Degree of

Master of Science

Thesis: DOE STUDY OF POLYURETHANE PROCESSING PARAMETERS
AFFECTS ON MICROPHASE SEPARATION AND MATERIAL
PROPERTIES

Major Field: Material Science and Engineering

Biographical:

Education:

Completed the requirements for the Master of Science in Material Science and Engineering at Oklahoma State University, Stillwater, Oklahoma in December, 2016.

Completed the requirements for the Bachelor of Science in Mechanical and Aerospace Engineering at Oklahoma State University, Stillwater, Oklahoma in December, 2013.

Experience:

- Mechanical Engineer in Technology Development at T.D. Williamson, 2014
- Technical internship at Sandia National Laboratory, 2012, 2013
- Technical internship at GE Aviation, 2011

Professional Memberships: ASME, SAE, AIAA